Evolutionary Optimization of Nanophotonic Design for Optical and Optoelectronic Applications

Evolutionary Optimization of Nanophotonic Design for Optical and Optoelectronic Applications

Ping Bai

The cover image has been designed with the motion of bird flocks in the blue sky as background. In addition, some elements related to the thesis are artistically designed, including a square array of nanoparticles on a substrate, surface lattice resonance spectra from figure 1.9 (b), spectra for strong light-matter coupling, and the chemical structure of Poly(3-hexylthiophene).

Evolutionary Optimization of Nanophotonic Design for Optical and Optoelectronic Applications

THESIS

door

Ping Bai

geboren te Jiangxi, China

Dit proefschrift is goedgekeurd door de promotoren en de samenstelling van de promotiecommissie is als volgt:

voorzitter:	prof.dr.ir. Gerrit M.W. Kroesen	
1^e promotor:	prof.dr. Jaime Gómez Rivas	
2^e promotor:	prof.dr. Andrea Fiore	
Ieden:		
	prof.dr.ir. Idelfonso Tafur Monroy	
	dr. Peter Zijlstra	
	prof.dr. Jianting Ye	(Rijskuniversiteit Groningen)
	dr. Andrea Baldi	(Vrij Universiteit)

Het onderzoek of ontwerp dat in dit wordt beschreven is uitgevoerd in overeenstemming met de TU/e Gedragscode Wetenschapsbeoefening.

"I am a slow walker, but i never walk backwards."

(us)Abraham Lincoln

Contents

CHAPTER 1

INTRODUCTION

This chapter provides a brief overview of optical resonators based on nanoparticles and periodic nanostructures by introducing the finite-differences time-domain (FDTD) method. Beginning with the description of localized resonances in single nano-disk structures, this chapter introduces also collective plasmonic resonances or surface lattice resonances (SLRs) that are supported in periodic nanoparticle arrays. An evolutionary optimization, based on the so-called particle swarm optimization (PSO), is introduced. This optimization is widely used in this thesis for the inverse design of the geometrical parameters of nanostructures with different functionalities. This chapter ends with the outline of the thesis.

1.1   Introduction

When somebody says the word "light," a listener usually interprets it as "visible light." Visible light is defined as electromagnetic (EM) waves that are visible to human eyes. Generally speaking, light is EM radiation in the visible spectrum. The spectrum of EM waves expands over a wide range, covering radio waves, microwaves, infrared radiation, ultraviolet radiation, and X-rays. Throughout our world, EM waves are the most common carrier of information. For example, light travels through the atmosphere to the surface of the earth so that we can see the world with our eyes. In modern communication, EM waves are used in cell phones, wireless internet networks, navigation devices in ships and aircrafts, and so on. They can be emitted by a variety of electrical and electronic appliances that influence an integral part of our lives. Light is also generated artificially with light emitting diodes (LEDs) or it is used for the generation of electricity in solar cells. Light, and more generally EM waves, is also omnipresent in sensors and for health applications. Another example are microwave ovens that use microwave radiation to heat food by the absorption of this radiation. The field of optics studies the propagation of light through different media. The field of photonics studies more broadly the generation, propagation, manipulation, conversion and detection of light, while nanophotonics aims at controlling these phenomena with nanometer precision.

A resonant optical cavity is an arrangement of optical components which allows a beam of light to circulate in a closed path, storing electromagnetic energy [1]. Such resonators can be made in different forms, e.g. two mirrors facing each other. Nanophotonic resonators are defined by optical cavities that are on the order of tens to hundreds of nanometers in size. They are widely used in various photonic devices and contribute to the enhancement of the light intensity. Nanophotonic resonators offer inherently large light energy confinement, strong light-material interactions and, therefore, intriguing novel phenomena, such as large non-linear responses or low lasing thresholds [2, 3].

The design of nanostructures that can resonantly interact with light is of crucial importance to enhance light-matter interactions and to control field distributions at subwavelength scales. Novel nanostructures offer technological solutions with high innovation potential. Computational inverse-design — algorithmic techniques for discovering optical structures based on desired functional characteristics — have been proposed to reshape the landscape of structures available to nanophotonics [4]. Inverse-design methods explore the parametric space of manufacturable devices. Generally, these methods are applied using various simulation software, where we can design, model and mesh the nanostructures, calculating and visualizing the required features [5–7]. In the projects described in this PhD thesis, we use Finite-Difference Time-Domain (FDTD) simulations (Lumerical Inc.) to obtain the optical response of nanophotonic structures, including the modeling and inverse design of the nanostructures for different applications in optical and optoelectronic devices [7].

1.2 Maxwell Equations and Finite-Difference Time-Domain (FDTD) Simulations

1.2.1 Maxwell Equations

In the 1860s, physicist and mathematician James Clerk Maxwell first used the equations which correctly predicted that visible light is an electromagnetic wave by demonstrating how fluctuating electric and magnetic fields propagate at a constant speed in vacuum [8]. These equations are named as "Maxwell's equations" and are four coupled partial differential equations based on the laws of Faraday, Ampére-Maxwell, and Gauss for magnetic and electric flux densities. They are considered as the foundation of optics and are used to understand the electromagnetic field distribution, the interaction between matter and EM fields, and other relevant characteristics. In SI convention, they can be written as:

$$\nabla \cdot \mathbf{D} = \rho, \tag{1.1}$$

$$\nabla \cdot \mathbf{B} = 0, \tag{1.2}$$

$$\nabla \times \mathbf{E} = -\frac{\partial \mathbf{B}}{\partial t}, \tag{1.3}$$

$$\nabla \times \mathbf{H} = \mathbf{J} + \frac{\partial \mathbf{D}}{\partial t}. \tag{1.4}$$

Here, $\mathbf{E}$ and $\mathbf{H}$ are the electric and magnetic fields, respectively. $\mathbf{D}$ and $\mathbf{B}$ are the electric displacement field and magnetic flux density, respectively. ρ is the free electric charge density and $\mathbf{J}$ is the free current density.

Situations having analytical solutions of Maxwell's equations are rare due to the complex electromagnetic field distribution in real structures. Thus, computational methods of electromagnetics are important. For these computational methods, there are two major types: time-domain and frequency-domain. The time is discretized in time-domain methods and the field distribution at a particular time step is determined by Maxwell's equations and by the spatial field distribution at the previous time step. In frequency-domain methods, the time derivative is replaced by $i\omega$, where i is the imaginary unit and ω is the angular frequency. Thus, Maxwell's equations are solved in the frequency domain at single frequencies and the simulation is repeated by changing this frequency to obtain a broadband response similar to that obtained with time-domain methods. In our work, we choose the Finite-Difference Time-Domain (FDTD) method that is implemented within the Lumerical's device multiphysics simulation suite in Ansys [7].

1.2.2 FDTD Simulations

In FDTD simulations, Maxwell equations are solved numerically on a discrete grid in both space and time, which means that the electric $\mathbf{E}$ and magnetic $\mathbf{H}$ fields are discrete in space and time:

$$\mathbf{E}(x, t) \rightarrow \mathbf{E}\left((i + \frac{1}{2})\Delta x, (n + \frac{1}{2})\Delta t\right) \rightarrow \mathbf{E}_{i+\frac{1}{2}}^{n+\frac{1}{2}}. \tag{1.5}$$

The electric and magnetic field components are distributed in space over a unit cell called the Yee cell, as shown in Fig. 1.1. This staggering of the fields in space is ideal for calculating spatial derivatives of the curl terms at the correct positions in space. The spatial grid step is generally called Δx or Δy or Δz, and the temporal grid is called Δt. For convenience of notation, we can drop the $\Delta x/\Delta y/\Delta z$ and Δt by simply referring to the spatial grid as i, j or k, and the temporal grid as n. Furthermore, we often use a subscript and superscript notation for the spatial position and time step respectively. The $\mathbf{E}$ fields are solved at time $n+\frac{1}{2}$, while the $\mathbf{H}$ fields are solved at time n. The derivatives in both space and time are calculated with finite differences:

$$\frac{\partial}{\partial t}\mathbf{E}^n = \frac{\mathbf{E}^{n+\frac{1}{2}} - \mathbf{E}^{n-\frac{1}{2}}}{\Delta t} + \mathbf{O}\left(\Delta t^2\right), \tag{1.6}$$

$$\frac{\partial}{\partial x}\mathbf{E}_i = \frac{\mathbf{E}_{i+\frac{1}{2}} - \mathbf{E}_{i-\frac{1}{2}}}{\Delta x} + \mathbf{O}\left(\Delta x^2\right). \tag{1.7}$$
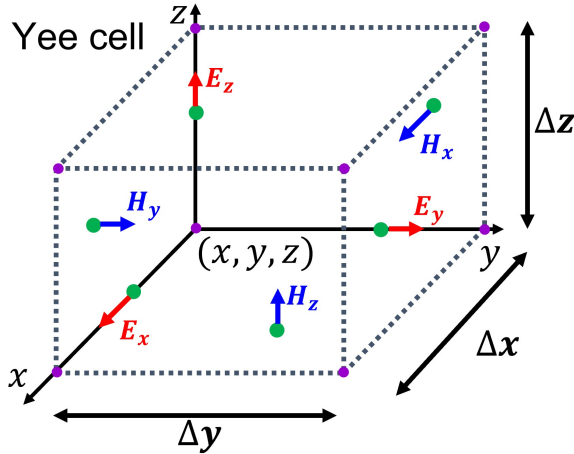
Figure 1.1: FDTD Yee Cell of dimension Δx, Δy, Δz. [9]

The $\mathbf{E}$ and $\mathbf{H}$ fields are typically zero at the beginning of the simulation,

$$\mathbf{E}^{-\frac{1}{2}} = 0, \tag{1.8}$$

$$\mathbf{H}^0 = 0. \tag{1.9}$$

Then, $\mathbf{E}$ is updated at time $n+\frac{1}{2}$, which is a function at the previous time step plus a term proportional to the curl of $\mathbf{H}$ at time step n:

$$\mathbf{E}^{n+\frac{1}{2}} = \mathbf{E}^{n-\frac{1}{2}} + \frac{\Delta t}{\epsilon}\nabla \times \mathbf{H}^n. \tag{1.10}$$

Once we have the **E** field updated to time $n + \frac{1}{2}$, we can proceed to update **H** at time $n + 1$, which is a function of **H** at the previous time step and the curl of **E** taken at time step $n + \frac{1}{2}$:

$$\mathbf{H}^{n+1} = \mathbf{H}^n - \frac{\Delta t}{\mu} \nabla \times \mathbf{E}^{n+\frac{1}{2}}. \tag{1.11}$$

In this way, we can leapfrog the update of **E** and **H** until the simulation is stopped,

$$\mathbf{H}^0 \rightarrow \mathbf{E}^{\frac{1}{2}} \rightarrow \mathbf{H}^1 \rightarrow \mathbf{E}^{\frac{3}{2}} \rightarrow \mathbf{H}^2 \rightarrow \mathbf{E}^{\frac{5}{2}} \rightarrow \mathbf{H}^3 \rightarrow ... \tag{1.12}$$

It is important to stress that we do not calculate **E** and **H** at the same instant in time. They are offset by one half time step. In fact, if we record the **E** field as a function of time with a monitor and plot it, the monitor will interpolate the original FDTD **E** fields to the same time step as **H**, so that this offset is easily overlooked. However, this leapfrog approach has the advantage of allowing us to obtain second order accuracy in time, which means that the error between the electromagnetic fields calculated by FDTD and the correct solution scales with the time step squared.

The FDTD method is a rigorous and powerful tool for modeling nanoscale optical devices and solve Maxwell's equations directly from the numerical simulation of the electromagnetic wave propagation. Its strength resides in the allocation in space of the electric and magnetic field components, and the time evolution in all three spatial dimensions of these fields. FDTD has been successfully applied to an extremely wide variety of problems, such as scattering, transmission, reflection, absorption from various objects and materials [10–13], involving typical applications of optical devices, such as LEDs, solar cells, filters, optical switches, semiconductor-based photonic devices, sensors, nano- and micro-lithography, nonlinear devices, and metamaterials [14–17].

1.2.3   Material Properties

The constitutive relation in electromagnetism relates the displacement vector **D** with the applied electric field **E** through the material permittivity ϵ. In dispersive materials, this relation is written as

$$\mathbf{D}(\omega) = \epsilon(\omega)\mathbf{E}(\omega). \tag{1.13}$$

Since FDTD is a time-domain solver, we need to convert this relationship to the time domain, where the product in the frequency domain becomes a convolution in the time domain

$$\mathbf{D}(t) = \epsilon(t) \circledast \mathbf{E}(t) = \int_0^t \mathbf{E}(t')\epsilon(t - t')dt'. \tag{1.14}$$

Performing this integration at each time step in the simulation would require more time and memory than would be practically feasible. It turns out that for a certain functions there are solutions that do not require performing the integration. However, these functions have to fulfill certain conditions, including stability and causality. These conditions

define the Kramers-Kronig relations between the real and imaginary components of the permittivity that impose that it is impossible that the displacement field at a certain time depends on electric field at a later time [18–20]. Before running broadband simulations, a broadband material fit to the complex permittivity is generated which meets these restrictions for dispersive materials.

To account for the dispersive nature of optical materials, FDTD simulators typically employ Drude, Debye, or Lorentz materials. These models describe conductive materials, polar materials and materials having a resonant response at defined frequencies. Originally derived from simplified models of the permittivity of idealized materials, these models offer good insight into the behavior of optical materials but fail to accurately capture the dispersive properties of real materials. The dispersion of real materials is impacted by impurities or defects that invalidate the assumptions of these as being ideal. To obtain a better agreement with experiments, it is a good practice to import the complex refractive index of real materials that are measured with, e.g., ellipsometry, into sampled data for FDTD simulations. A multi-coefficient model (MCM) is then generated using a broadband fit to the measured data and meeting the required restrictions imposed by causality. The MCM is able to accurately represent real materials over broad wavelength ranges.

1.3   Optical Resonators

In physics, a resonance is the tendency of a system to vibrate with increasing amplitudes at a defined frequency of excitation. The use of optical resonances has become a powerful tool for precision measurements [21], non-linear interactions [22–24], detection sensitive enhancement [25, 26], light emission [27–29], and quantum optics [30, 31]. A optical resonance occurs when the optical feedback is in phase with the intracavity optical field. Different types of resonators are schematically represented in Fig. 1.2. The optical feedback is typically provided by a pair of mirrors facing each other (Fabry-Perot resonator) so that light emitted along the line between the mirrors forms a standing wave. The cavity is able to store electromagnetic energy, increasing the wave amplitude.

Optical resonances can be also built in optical waveguides [32, 33], or at the interface between a metal and a dielectric in what is known as a surface plasmon polaritons [34]. In this thesis, nanometer size particles are thoroughly investigated. Such individual nanoparticles can support localized surface plasmon resonances (LSPRs) that correspond to the coherent oscillation of the free electrons in metallic nanoparticles and the associated oscillations of the EM field [35]. The resonance frequency of LSPRs can be easily controlled by the size, shape, composition, and local optical environment of the particle [36]. For nanoparticles of noble materials, i.e., Au, Ag and Cu, LSPRs typically occur in the visible to the near-infrared electromagnetic spectrum [37]. Aluminum is an alternative plasmonic material in the UV and visible regions of the spectrum with properties and potential applications similar to those of noble metals. [38] Also dielectric nanoparticles support resonances known as Mie resonances arising from the displacement currents induced in the nanoparticles by the applied EM fields [39]. Based on nanoparticles, different kinds of optical resonances are explained in the next sections
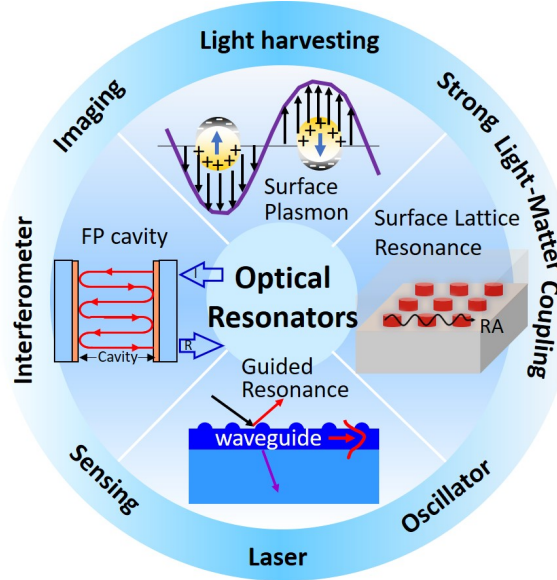
Figure 1.2: Overview of optical resonators with different configurations, including Fabry-Perot (FP) cavities, localized surface plasmons or Mie resonances, waveguided resonances and surface lattice resonances. Different applications of optical resonators for imaging, light harvesting, sensing, lasing, and strong light-matter coupling.

and gradually introduced into various applications in the chapters of this thesis. An interesting cavity type, thoroughly investigated here, is distributed feed-back cavities in arrays of nanoparticles. These cavities support the so-called surface lattice resonances (SLRs) that result from the enhanced radiative coupling of localized resonances in indivual nanoparticles by in-plane diffraction orders in the array, also known as Rayleigh anomalies (RAs) [40, 41].

1.4 Optical Resonances of Individual Nanoparticles

The simplest approach to understand the optical resonant behavior of small nanoparticles is the dipole oscillator model including the self-inductance force. In what follows, we reproduce the derivation of Ref. [42], which is able to illustrate the scattering and absorption processes of these particles under illumination. In the dipole oscillator model, the electron location is described as $x(\omega, t)$ with a angular frequency ω and real time t. Each electron has the electric charge of $q_e = 1.60 \times 10^{-19}$ C and electron mass $m_e = 9.11 \times 10^{-31}$ kg. The restoring force constant of the dipole is labeled as κ. The self-induced inductance force due to the electric charge oscillation is characterized as L with the unit of henry per meter

(H/m), which is proportional to the change rate of the electrical current as

$$F = -q_e L \frac{dI}{dt} = -q_e^2 L \frac{d^2 x(\omega, t)}{dt^2}. \tag{1.15}$$

In the dipole oscillator model, the internal damping coefficient is Γ_a. The radiation co-efficient of the oscillator is Γ_s. The oscillator is driven by a harmonic electric field with frequency ω and the equation of motion can be written as

$$m_e \frac{d^2 x(\omega, t)}{dt^2} + \Gamma_a \frac{dx(\omega, t)}{dt} + \kappa x(\omega, t) = q_e E_0 e^{i\omega t} + \Gamma_s \frac{d^3 x(\omega, t)}{dt^3} - q_e^2 L \frac{d^2 x(\omega, t)}{dt^2}, \tag{1.16}$$

By moving the inductance force term to the left side of the equation and defining the effective electron mass $m_e^* = m_e + q_e^2 L$, we have

$$m_e^* \frac{d^2 x(\omega, t)}{dt^2} + \Gamma_a \frac{dx(\omega, t)}{dt} + \kappa x(\omega, t) = q_e E_0 e^{i\omega t} + \Gamma_s \frac{d^3 x(\omega, t)}{dt^3}, \tag{1.17}$$

Assuming an harmonic electron motion $x(\omega, t) = x_0(\omega) e^{i\omega t}$, the solution of Eq. (1.17) is given by

$$x(\omega, t) = x_0(\omega) e^{i\omega t} = \frac{(q/m_e^*) E_0}{\omega_0^2 - \omega^2 + i \frac{\omega}{m_e^*} (\Gamma_a + \omega^2 \Gamma_s)} e^{i\omega t}, \tag{1.18}$$

where $x_0(\omega)$ is the complex amplitude of the dipole oscillation and $\omega_0 = \sqrt{\kappa/m_e^*}$. The time averaged power dissipated by the oscillator can be written as $P(\omega) = F^*(\omega)[i\omega x_0(\omega)]$, where $F^*(\omega)$ is the complex conjugate of the force applied to the electrons. Therefore, the total scattered and absorbed power can be written as

$$P_{sca}(\omega) = N^2 \omega^4 \Gamma_s |x(\omega)|^2, \tag{1.19}$$

$$P_{abs}(\omega) = N^2 \omega^2 \Gamma_a |x(\omega)|^2, \tag{1.20}$$

where N is the number of electrons participating in the oscillation. Consider a uniform light beam of irradiance I_0 incident on a particle of geometric cross section $A(R) = \pi R^2$. Here R is the radius of particle. The particle scatters an amount of power $P_{sca}(\omega)$ into all directions and define the scattering cross section as

$$C_{sca}(\omega) = P_{sca}(\omega)/I_0. \tag{1.21}$$

Similarly, the particle absorbs an amount of power $P_{abs}(\omega)$ leading to the absorption cross section

$$C_{abs}(\omega) = P_{abs}(\omega)/I_0, \tag{1.22}$$

where $I_0 = \frac{1}{2}\sqrt{\frac{\mu_0}{\epsilon_0}} |E_0|^2$ is the intensity of the incident optical wave. The scattering and absorption efficiencies, $Q_{sca/abs}(\omega, R)$, are defined as the ratio of the scattering and absorption cross sections to the geometric cross section,

$$Q_{sca}(\omega, R) = C_{sca}(\omega)/A(R), \tag{1.23}$$

$$Q_{abs}(\omega, R) = C_{abs}(\omega)/A(R). \tag{1.24}$$

Because of the nature of electromagnetic scattering, $Q_{sca}(\omega, R)$ can approach a value of 10 for non-absorbing resonant particles. For particles much smaller than the wavelength, the scattering is less efficient and the scattering cross section is much less than $A(R)$.

The response of a nanoparticle to an applied field can be retrieved from the induced dipole moment $\mathbf{p}$, whose magnitude is proportional to the incident field E_0. The proportionality term is the polarizability, defined through $\mathbf{p} = \alpha_0 \mathbf{E}_0$. The polarizability in the dipole approximation of a small sphere/particle compared to the wavelength of the EM radiation and with volume V is given by [35]

$$\alpha_0(\omega) = 3\epsilon_0 V \left(\frac{\epsilon_m(\omega) - \epsilon_d(\omega)}{\epsilon_m(\omega) + 2\epsilon_d(\omega)} \right). \tag{1.25}$$

Here, $\epsilon_m(\omega)$ refers to the dielectric permittivity of the sphere/particle, while $\epsilon_d(\omega)$ refers to the dielectric permittivity of the embedding medium. The polarizability can be corrected to include the effects of radiation damping by introducing an additional damping channel

$$\frac{1}{\alpha(\omega)} = \frac{1}{\alpha_0(\omega)} - \frac{ik^3}{6\pi\epsilon_0}. \tag{1.26}$$

The above scattering and absorption cross sections in the dipole approximation can be expressed in terms of the polarizability as

$$\mathbf{C}_{sca}(\omega) = \frac{k^4}{6\pi\epsilon_0} |\alpha(\omega)|^2, \tag{1.27}$$

$$\mathbf{C}_{abs}(\omega) = \frac{k}{\epsilon_0} \mathrm{Im}\alpha(\omega), \tag{1.28}$$

where $k = 2\pi\sqrt{\epsilon_d}/\lambda$ is the wavevector of light outside the scattering sphere/nanoparticle. The absorption and scattering cross sections in terms of the polarizability retain their validity for particles with diameters up to ~ 100 nm.

For larger nanoparticles, it is possible to use FDTD to retrieve the scattering and absorption cross-sections and efficiencies. As an example, we have simulated the scattering and absorption efficiencies for an aluminum nanodisk that is embedded in SiO_2. The model for these simulations is displayed in Fig. 1.3. The permittivity of the aluminum used for the simulations is taken from Ref. [43], and the refractive index of SiO_2 is set to n=1.46. The aluminum disk has a height H and diameter D. A total-field scattered-field (TFSF) source is used in these simulations. The TFSF source injects a short pulse with a temporal Gaussian envelope in the z-direction. The source region is represented by the dashed-red box in Fig. 1.3. The simulation region is presented as a dashed-black box, which has a volume of 1.2 μm by 1.2 μm in the x and y directions, and 1.8 μm in the z direction. Perfectly matched layer (PML) boundary conditions are used for the all boundaries of the simulation region. These boundary conditions suppress the back reflection of the scattered wave into the simulation volume. Based on the full vectorial
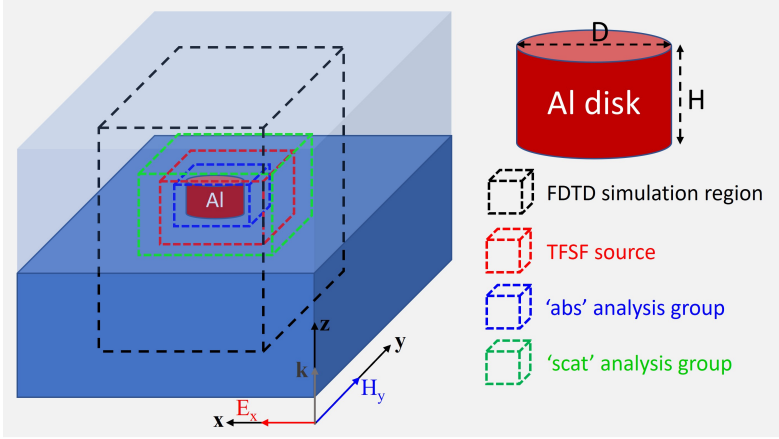
Figure 1.3: Schematic representation of a model setup for FDTD simulations: single Al disk with diameter D and height H embedded in SiO$_2$ ($n = 1.46$). Dashed black, red, blue and green boxes indicate the FDTD simulation region, TFSF source region, absorption analysis group and scattering analysis group, respectively. The polarization of the incident electric and magnetic fields are along the x- and y-axis, respectively.

solutions of the Maxwell's equations in FDTD simulations, two analysis group boxes are defined to measure the net power flowing in/out of the box. The 'abs' analysis group that measures the absorbed power of nanoparticle must be completely inside the TFSF source but enclosing the nanodisk, as shown in Fig. 1.3 with the dashed blue box. While the 'scat' analysis group, which measures the scattered intensity, must be completely outside the TFSF source (dashed green box) to collect the net optical power scattered from the aluminum nanoparticle. The scattering and absorption cross-sections are obtained by dividing the scattered and the absorbed powers by the power of the incident optical wave and the geometrical cross section of the nanodisk.

The results of the simulations are plotted in Fig. 1.4 for different diameters and heights of the nanodisks. The scattering efficiency in Fig. 1.4 (a) exhibits a strong peak that red-shifts when the diameter of the nanodisk increases. This peak corresponds to the fundamental LSPR and it becomes broader at longer wavelengths due to the increased radiation losses. Compared to the scattering, the absorption efficiency in Fig. 1.4 (b) shows a weaker resonance and a larger absorption for smaller diameters. This result is expected based on the dependence of the scattering cross-section with the square of the nanoparticle polarizability and of the absorption cross-section with the imaginary component of this polarizability (Eqs. (1.27) and (1.28)), which scales with the volume of the nanodisk (Eqs. (1.25) and (1.26)). Therefore, absorption becomes dominant for small nanoparticles, while scattering dominates the response of bigger nanoparticles.

Aside from the size dependence of the absorption resonance, we note that the absorption losses are particularly low both in the visible and the infrared range. This makes aluminum a suitable material in these wavelength ranges for potential applications [44].
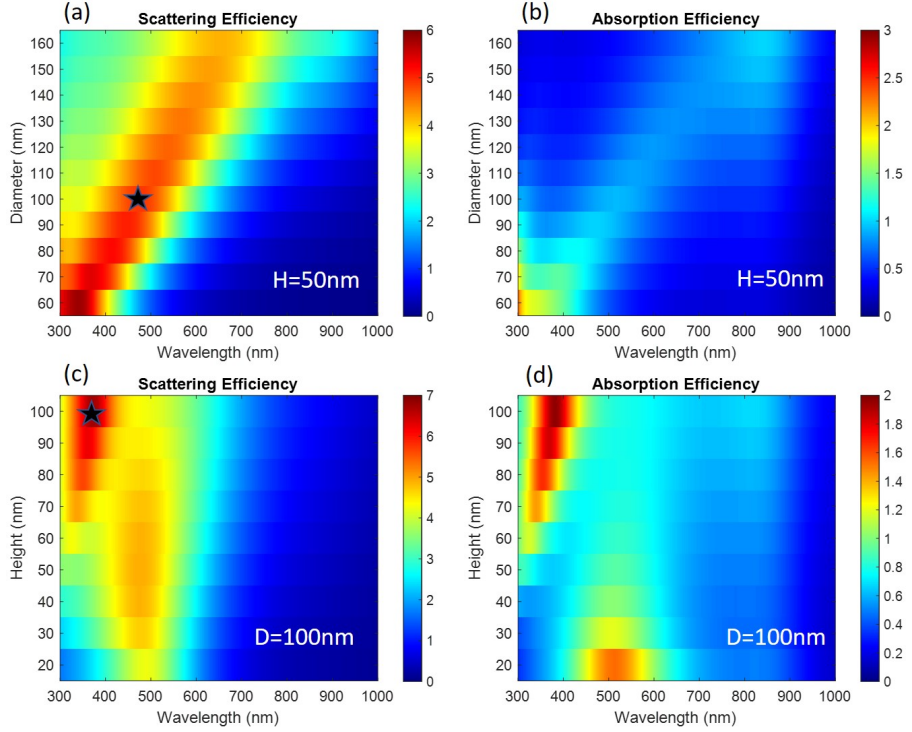
Figure 1.4: FDTD simulations of the optical response of single Al nanodisk embedded in silica. (a) Scattering and (b) absorption efficiencies for a nanodisk with height $H = 50$ nm and diameter in the range $D = 60$–160 nm. (c) Scattering and (d) absorption efficiencies for a nanodisk with $D = 100$ nm and $H = 20$–100 nm. The nanodisk is illuminated along its height from below with a broadband collimated beam ($\lambda = 300$–1000 nm).

As the height of the nanodisk is increased, a high-order resonance appears at shorter wavelengths, as shown both in the scattering (Fig. 1.4 (c)) and absorption (Fig. 1.4 (d)) efficiencies.

In order to better describe the resonances supported by single nanodisks, we focus on two nanodisks with H=50 nm and H=100 nm. These nanodisks are indicated in Figs. 1.4 (a) and (c) with the black stars. The nanodisks have the same diameter in both cases. The scattering and absorption efficiencies for these two cases are plotted in Figs. 1.5 (a) and (c). For H=50 nm, there is only one broad scattering peak with the maximum at 477 nm. Another resonance appears at 372 nm for H=100 nm. The spatial distributions of the electric field intensity enhancement relative to the incident field intensity for these two resonances are represented in Figs. 1.5 (b) and (d), respectively. The color scale in these figures represents the field intensity, while the white arrows define the vectorial electric field amplitude projected in the xz-plane. For the fundamental LSPR, the electric field in Fig. 1.5 (b) is mainly oriented parallel to the incident electric field. The near-field
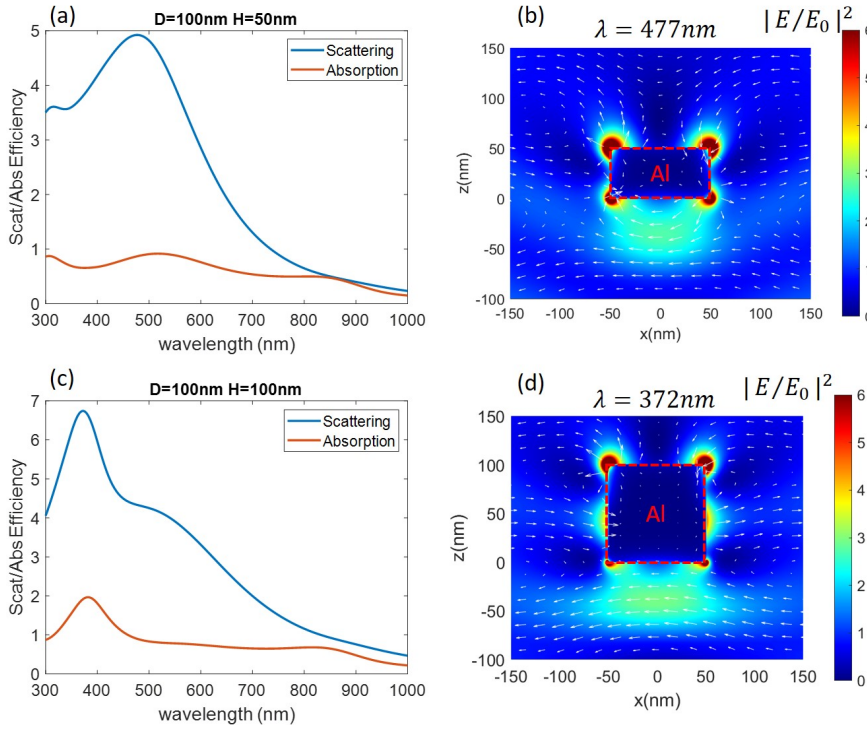
Figure 1.5: (a) Scattering (blue) and absorption (red) efficiency spectra for a single Al nanodisk with D=100 nm and H=50 nm in silica. (c) Same as (a) for an Al nanodisk with D=100 nm and H=100 nm. Panels (b) and (d) are the spatial distributions of the electric field intensity $|E|^2$, normalized to the incident field intensity $|E_0|^2$, calculated on the xz-plane crossing the center of the nanoparticle for wavelengths $\lambda = 477$ nm and $\lambda = 372$ nm, which correspond to the maximum scattering efficiencies in (a) and (c). The color scale represents the intensity and the white arrows represent the electric field amplitude projected in the xz-plane. The shape of the particle is denoted with the dashed-red rectangle.

outside the particle is distorted with respect the near-field created by an electric dipole in a nanodisk as a consequence of the finite size of the nanoparticle. Compared to the fundamental LSPR, the higher-order resonance displays an enhanced near-field confinement at half height of the nanodisk as shown in Fig. 1.5 (d), resulting for the increased size of the nanodisk and the concomitant retardation effect.

In summary, the LSPRs in single nanoparticles depend on the size and shape of the particles, including the height and diameter for nanodisks, as well as on the medium surrounding the particles [36]. Accordingly, LSPRs can be tuned to control the quality factor (Q-factor) and electromagnetic field confinement.

1.5 Diffraction and Rayleigh Anomalies (RAs) in Nanoparticle Arrays

Dating back to 1902, Prof. R. W. Wood measured the dependence of the light diffracted from various metallic gratings on the angle and wavelength of the incident wave [45]. An 'Anomaly' was observed in the specular reflection (zeroth order of diffraction) at certain angles and wavelengths when the wave vector of the incident beam was in the plane perpendicular to their grooves and its magnetic vector was parallel to the grooves, i.e. for p-polarization. This anomaly corresponds to the increase of the specular reflection intensity followed by a sudden drop of this intensity. The wavelength of this phenomenon was nearly independent of the metal, but determined by the period of the grating and its surrounding medium. Five years later, Lord Rayleigh attributed the increase of the intensity in Wood's anomalies to diffraction orders in the plane of the array, i.e., the increase of intensity occurs when a diffraction order disappears in the horizon defined by the surface of the grating [46], as illustrated in Fig. 1.6 (a).[1] Rayleigh's anomalies (RAs) thus correspond to the condition (wavelength and angle of incidence) at which a diffracted order is in the plane of the array.
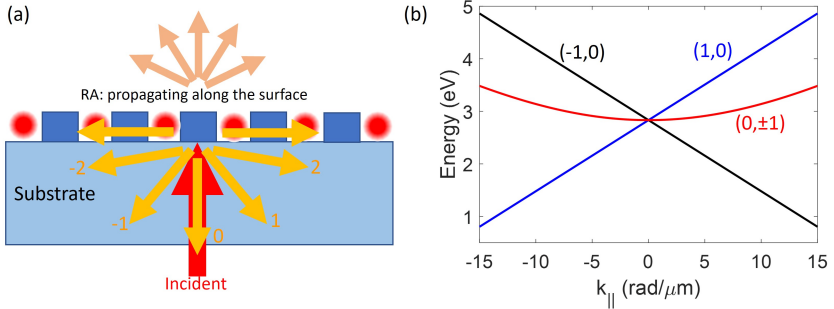
Figure 1.6: (a) Schematic illustration of the diffraction processes in a nanoparticle array. (b) Calculated RAs dispersion for the (1,0), (-1,0) and (0,±1) orders of a square array with period $a = 300$ nm and an effective refractive index of surrounding medium $n = 1.46$.

To calculate the RAs, we can use the grating equation relating the in-plane wave vector of the diffracted orders ($\mathbf{k}_{||}^{out}$) with the in-plane component of the incident wave vector ($\mathbf{k}_{||}^{in}$) and the reciprocal lattice vector ($\mathbf{G}_x, \mathbf{G}_y$) defining the lattice momentum in the x and y-directions for (p, q) diffracted orders:

$$\mathbf{k}_{||}^{out} = \mathbf{k}_{||}^{in} + p\mathbf{G_x} + q\mathbf{G_y}, \tag{1.29}$$

where $\mathbf{G}_x = (2\pi/a_x)\mathbf{u}_x$ and $\mathbf{G}_y = (2\pi/a_y)\mathbf{u}_y$ and a_x, a_y are the lattice constants. The simplest array is a square lattice, where the periods in the x and y-directions are equal, $a_x = a_y = a$. Thus the wavelengths of RAs can be calculated from Eq.(1.29) with a diffracted angle

---

[1]The drop in the intensity was due to the grating coupling to surface plasmon polaritons [47].

$\theta_d = 90°$, i.e., diffraction along the plane of the array. For normal incidence ($\mathbf{k}_{||}^{in} = 0$) this wavelength is

$$\lambda_{RA}^{(p,q)} = \frac{na}{\sqrt{p^2 + q^2}},$$
(1.30)

Here, n is the refractive index of the medium in which the grating is embedded. Under the illumination at various angles of incidence (here we assume $k_{//}^{in}$ is along the k_x), we are particularly interested in the angular dispersion as a function of the incident photon energy, given by

$$E^2(k_{||}^{in}) = \left(\frac{\hbar c}{n}\right)^2 \left[\left(k_{||}^{in}\right)^2 + \left(\frac{2\pi}{a}p\right)^2 + \left(\frac{2\pi}{a}q\right)^2 + 2k_{||}^{in}\frac{2\pi}{a}p\right].$$
(1.31)

In the next chapters, we will frequently show the RA dispersion for different orders, especially for the fundamental orders. The non-degenerate (1,0) and (-1,0) RAs show a linear dispersion, while the degenerate (0,±1) RAs exhibit a parabolic dispersion. These RAs dispersion are displayed in Fig. 1.6 (b) for a square lattice with period a = 300 nm and refractive index of surrounding medium n = 1.46.

1.6   Surface Lattice Resonances

Localized resonances supported by individual nanoparticles (LSPRs in metallic nanoparticles and Mie resonances in dielectric nanoparticles) involve the current of free charges or the displacement current of bound charges, and the associated electromagnetic field. For the most common plasmonic materials, including gold (Au), silver (Ag) and aluminum (Al), the LSPRs typically occur in the visible and near-infrared regions of the spectrum. Interband transitions in Au at wavelengths shorter than 550 nm introduce a dissipative channel that suppress the plasmonic effect. Ag has the ability to support LSPRs down to 350 nm, but suffers a rapid oxidation that degrades its plasmonic properties. Therefore, Ag nanoparticles are usually passivated with a thin layer of Al_2O_3 to prevent the oxidation. Al has been demonstrated as a high-quality plasmonic material in the UV and visible regions of the EM spectrum [38, 48]. In this thesis, we will choose the plasmonic material according to the relevant wavelength range.
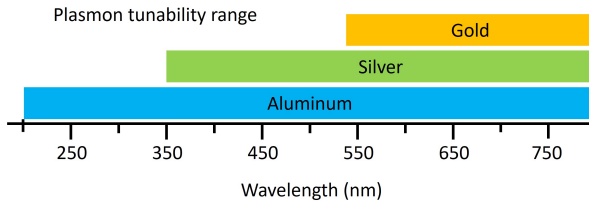
Figure 1.7: LSPRs tuning ranges of the most common plasmonic materials in the UV-visible [38].

The spectral line width of LSPRs is the result of the radiative and material damping [49]. As an example, the LSPRs of Au nanostructures exceed the full-width at half-maximum (FWHM) of ~80 nm [50], well above the values desired for many applications.

The limitations on the Q-factor of plasmonic resonances have been greatly overcome if the nanostructures are arranged in a periodic array [51–61] in where the electromagnetic fields scattered by the LSPRs of each nanoparticle influence the response of neighboring nanoparticles, leading to a reduction of the radiative damping. By appropriate tuning of the nanoparticle size, shape, and period of the array, it is possible for the scattered fields to be in phase with the LSPR induced in its neighboring particles. Thus, a significant improvement of the resonance Q-factor can be achieved by the diffractive coupling of LSPRs. For simplicity, we refer to these resonances in periodic arrays as surface lattice resonances (SLRs) [40, 62].

High-refractive-index dielectrics could replace metallic nanoparticles in particular applications to avoid the problem of strong non-radiative damping in metals. Dielectric nanoparticles support Mie resonances at optical frequencies based on magnetic or electric displacement currents that lead to high local field enhancements and low optical losses [39]. Dielectric particles, like Si, are also considered for the design of all dielectric metamaterials [39], demonstrating effects like optical magnetism [63, 64]. Arrays of such particles show total dielectric reflectance and field enhancement [65, 66]. Combining nanoparticles into arrays allow achieving much higher values of the Q-factor for SLRs [67–71].

To understand the nature of SLRs, the simplest rigorous mode is the coupled dipole model (CDM) [72, 73]. The CDM is a numerical method for solving Maxwell's equations and generating the absorption, scattering, and extinction cross-sections for arrays of nanoparticles. There are three important aspects in this method: first, every single nanoparticle is considered as an electric dipole and it does not consider multipolar resonances. Second, the local electromagnetic field for each nanoparticle is the sum of the incident field and the scattered fields from the neighboring dipoles. Finally, the response of the whole array involves the self-consistent determination of the reaction of each dipole to its local electromagnetic field.

To illustrate this method, let us consider a plasmonic nanoparticle square array of N polarizable nanoparticles (N must be large enough to show their collective behavior). As shown in Fig. 1.8, if the nanoparticles are small compared to the wavelength, the electric dipole polarization $\mathbf{P}_i$ of the ith nanoparticle at its center position $\mathbf{r}_i$ can be expressed as

$$\mathbf{P}_i = \alpha_i \cdot \mathbf{E}_{loc}(\mathbf{r}_i). \tag{1.32}$$

The ith nanoparticle has a polarizability α_i. $\mathbf{E}_{loc}(\mathbf{r}_i)$ is the total local electric field at the position of the nanoparticle, which represents the sum of the incident field $\mathbf{E}_0 e^{ik\mathbf{r}_i}$ and the retarded fields frpm the other N-1 nanoparticles in the array. This local field is given by

$$\mathbf{E}_{loc}(\mathbf{r}_i) = \mathbf{E}_0 e^{ik\mathbf{r}_i} + \sum_{j=1, j \neq i}^{N} \frac{e^{ik\mathbf{r}_{ij}}}{\mathbf{r}_{ij}^3} \left\{ k^2 \mathbf{r}_{ij} \times \left(\mathbf{r}_{ij} \times \mathbf{P}_j \right) + \frac{1 - ik\mathbf{r}_{ij}}{\mathbf{r}_{ij}^2} \times \left[\mathbf{r}_{ij}^2 \mathbf{P}_j - 3\mathbf{r}_{ij} \left(\mathbf{r}_{ij} \cdot \mathbf{P}_j \right) \right] \right\}, \tag{1.33}$$

where $\mathbf{r}_{ij}$ is the vector between the ith and jth nanoparticles with their distance $r_{ij} = |\mathbf{r}_{ij}|$, $k = 2\pi/\lambda$ is the wavenumber of the incident plane wave. The retardation effects can be simplified in a matrix $\mathbf{A}_{ij}$ for the coefficients in Eq. (1.33). Substituting Eq. (1.33) into Eq. (1.32), leads

$$\left(\alpha_i^{-1}\right)\mathbf{P}_i + \sum_{j\neq i} \mathbf{A}_{ij} \cdot \mathbf{P}_j = \mathbf{E}_{inc,i}. \tag{1.34}$$

Each element of $\mathbf{A}_{ij}$ is a 3×3 matrix. Defining $\mathbf{A}_{ii} = \alpha_i^{-1}$ reduces the scattering problem to finding the polarizability $\mathbf{P}_i$. After solving the set of $3N$ complex linear equations allows to obtaind the polarizability vector. Consequently, the extinction and absorption cross sections can be determined using [73]

$$C_{ext} = \frac{4\pi k}{|\mathbf{E}_{inc}|^2} \sum_{i=1}^{N} \text{Im}\left\{\mathbf{E}_{inc,i}^* \cdot \mathbf{P}_i\right\}, \tag{1.35}$$

$$C_{abs} = \frac{4\pi k}{|\mathbf{E}_{inc}|^2} \sum_{i=1}^{N} \left\{\text{Im}\left[\mathbf{P}_i \cdot \left(\alpha_i^{-1}\right)^* \mathbf{P}_i^*\right] - \frac{2}{3} k^3 |\mathbf{P}_i|^2\right\}. \tag{1.36}$$

The scattering cross section is given by

$$C_{sca} = C_{ext} - C_{abs}. \tag{1.37}$$

The CDM is also suitable for modeling the coupling effects of electric and magnetic fields separately in dielectric materials. [65, 74]
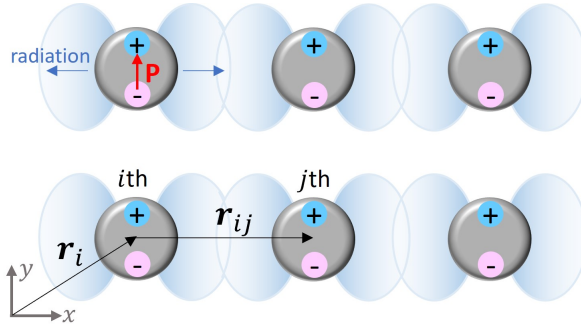
Figure 1.8: The radiative coupling of different nanoparticles depends on polarization. The dominant coupling direction is orthogonal to the polarization $\mathbf{P}$ [75].

Multipolar contributions to the polarizability can not be neglected in large nanoparticles. In this case, the T-matrix theory is frequently used because it includes a converged multipole expansion on each particle [72, 76]. As in the case of single particles, FDTD simulations can used to retrieve the scattering and absorption properties of arrays of nanoparticles with arbitrary size and shape. This is illustrated in Fig. 1.9, where (a) is a schematic representation of an square array of Al nanoparticles embedded in fused silica (n=1.46).
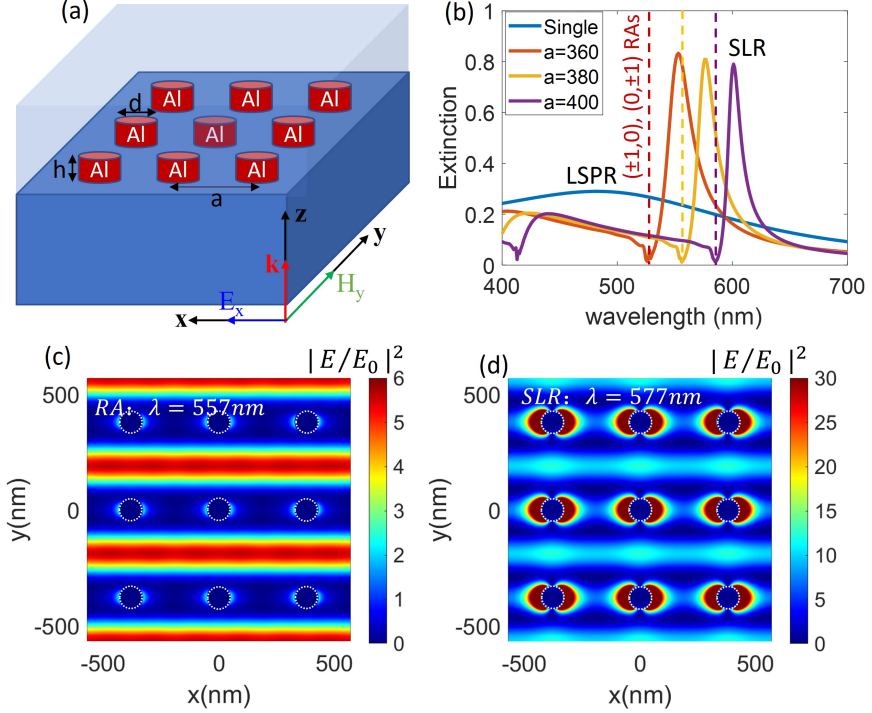
Figure 1.9: (a) Schematic representation of a square array of Al nanoparticles with lattice constant a, height h and diameter d, embedded in fused silica (n=1.46). The array is illuminated with a broadband (λ = 400–700 nm) plane wave incident normal to the plane of the array from below. The polarization of the incident electric field is along the x-axis. The FDTD simulations of the extinction spectra are shown in (b) for a single nanoparticle, and arrays with different lattice constants, a = 360, 380, and 400 nm. The non-degenerate and degenerate fundamental ($\pm$1,0), (0,$\pm$1) RAs at normal incidence are indicated by the dashed vertical lines. (c) and (d) are FDTD simulations of the spatial distribution of the electric field intensity $|E|^2$ normalized to the incident field intensity $|E_0|^2$, in the xy-plane of nine unit cells of the array with a periodicity of 380 nm for the RA wavelength (λ = 557 nm) and SLR wavelength (λ = 577 nm), respectively.

The FDTD simulated extinction spectra under the same illumination conditions are displayed in Fig. 1.9 (b) for single Al nanoparticle and arrays with different periodicity a. A broad and low extinction LSPR can be observed for the individual nanoparticle. SLRs can be regarded as the result of the hybridization of localized resonances with diffracted orders in the plane of the array (RAs) that simultaneously manifest very large spatial extension and strong EM field enhancement. This hybridization depends on the detuning of two bare modes and their damping. In the extinction spectra of the nanoparticle arrays shown in Fig. 1.9 (b), the extinction dips correspond to the RA wavelengths. The RAs are close to the broad LSPR mode, leading to a narrow and strong peak in the extinction (the SLR peak) at slightly longer wavelengths. By increasing the detuning between the localized

17

resonance and the RA, the photonic characteristics of the SLRs become more dominant leading to the narrower SLRs. Accompanied by the narrowing of the line width of the resonance, there is an increase of the decay length of the EM field in the direction perpendicular to the array. SLRs can lead to exceptionally large field enhancements close to the array that extend over large regions [41, 75, 77, 78].

For the example shown in Fig. 1.9, the polarization of the incident electric field is along the x-axis. The dominant radiation direction from the nanoparticles is orthogonal to the polarization, leading to radiative coupling along the y-direction, as shown in Figs. 1.9 (c) and (d) for the RA and SLR, respectively. In experiments, the near-field enhancement caused by SLRs is limited by the number of elements of the array that interact coherently [78].
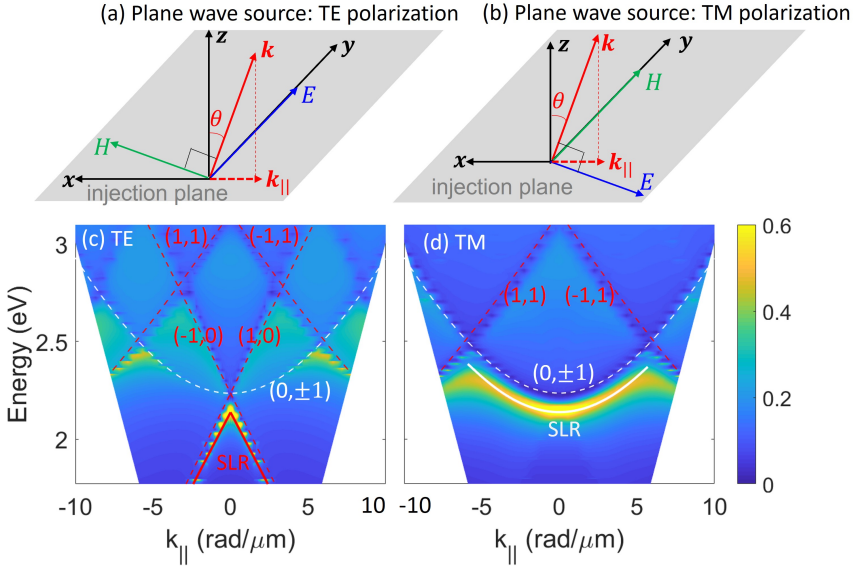
Figure 1.10: TE (a) and TM (b) polarization orientation of a plane wave source. The red arrow indicates the wave vector in the propagation direction, the blue arrow the electric (E) field, and the green arrow the magnetic (H) field. θ is the angle of incidence, and $k_{||} = k \sin \theta$ is the in-plane wave vector. (c) and (d) are the simulated energy dispersion of SLRs along (1,0) and (-1,0) RAs, and along the (0, ±1) RAs for TE and TM plane wave illumination, respectively. The energy of the LSPRs in the individual Al nanoparticles with diameter d = 100 nm and height h = 50 nm is 2.55 eV. The pitch size of the square array is 380 nm.

The hybridization of localized resonances with a diffraction order can be phenomenologically described using a damped coupled harmonic oscillator model. Within this model, the localized resonances in the individual nanoparticles are described as one oscillator, while the other resonator describes the RA from the lattice. The eigenstates of

this coupled system are given by [79]:

$$\begin{bmatrix} E_{LR} - i\gamma_{LR} & g \\ g & E_{RA} - i\gamma_{RA} \end{bmatrix} \begin{pmatrix} \alpha \\ \beta \end{pmatrix} = E \begin{pmatrix} \alpha \\ \beta \end{pmatrix}, \tag{1.38}$$

where E_{LR} and E_{RA} define the energies of the localized resonance and the RA with their associated losses of γ_{LR} and γ_{RA}, respectively, and g denotes the coupling strength. Diagonalizing the Hamiltonian given in Eq. (1.38) leads to the eigenfrequencies of SLRs, which can be expressed as

$$E_{\pm} = \frac{1}{2}(E_{LR} + E_{RA} + i(\gamma_{LR} + \gamma_{RA})) \pm \frac{1}{2}\sqrt{(4g)^2 + [E_{LR} - E_{RA} - i(\gamma_{LR} + \gamma_{RA})]^2}, \tag{1.39}$$

where E_- corresponds to the red-shifted peak in the extinction relative to the localized resonance that is indicated in Fig. 1.9 (b). This hybridization of localized resonances with diffraction orders to form SLRs have provided an interesting platform for many experimental and theoretical investigations associated with the interaction of light with nanomaterials.

SLRs have a similar linear or parabolic dispersion as the corresponding RAs. For a TE-polarized incident plane wave (Fig. 1.10 (a)), SLRs formed by the (1,0) and (-1,0) RAs have the linear dispersions shown in Fig. 1.10 (c). While for a TM-polarized source (Fig. 1.10 (b)), the degenerate SLRs formed by the $(0,\pm1)$ RAs exhibit a parabolic dispersion, as shown in Fig. 1.10 (d).

In the following chapters, SLRs will be demonstrated in different periodic arrays of both plasmonic and dielectric nanoparticles and various applications are discussed in detail.

1.7 Particle Swarm Optimization Method

A major goal of this thesis is the design and optimization nanophotonic structures for various applications. Particle swarm optimization (PSO) combined with FDTD simulations is used for this purpose. In the early of 1990s, scientists made a great effort in understanding animal's social behavior and showed that some animals belonging to certain groups were able to share information among them, giving these animals a great survival advantage. Inspired by this kind of social behavior of birds or fishes, Kennedy and Eberhart developed in 1995 a population based stochastic optimization technique named particle swarm optimization [80]. Imagine a swarm of birds looking for food in a vast valley were there is food only in one place. Without any knowledge of the food location, the birds begin in random locations with random flight velocities searching for the food. While flying through the valley, the birds keep their speed (inertia) constant but change their direction. Each bird tries to find food based on its intuition (cognitive behaviour) and position. But it also tends to imitate other birds (social behaviour) according to their reported positions. Each bird is thus influenced by its experience and knowledge of the whole swarm. The swarm of birds takes advantage of their large number to explore the valley as well as possible. This swarm of birds, after coordination, would exploit the best places by refocusing their search in these places.

Therefore, PSO is a robust stochastic computation technique based on the evolution of swarms. In attempting to model this behavior, some key terms are first given: *Particle* is each individual in the swarm who accelerate toward the best personal and best overall location, while constantly checking the value of its current location. *Position* represents a candidate solution to the problem, which can be optimized in the multi-dimensional solution space during the search process. This multi-dimensional solution space includes any variables that needed to be optimized. Reducing the optimization problem to a set of values that could represent a position in the simulation space is an essential step for using the PSO. *FoM* is the figure of merit, which is usually a single number calculated from a fitness function that represents the goodness of a given solution. The fitness function provides the interface between the physical problem and the optimization algorithm. In the analogy with the swarm of birds, the fitness function would be the distance of the bird from the food and a minimum value of this fitness is the goal. In physics, the Q-factor of a resonance, a certain performance of a device, the sensitivity to uncertainties, etc., can be the FoM for different applications. *pbest* is the position in the solution space of the best FoM returned for one individual particle. *gbest* is the location in parameter space of the best FoM returned for the entire swarm. Both pbest and gbest are constantly updated during the optimization process.
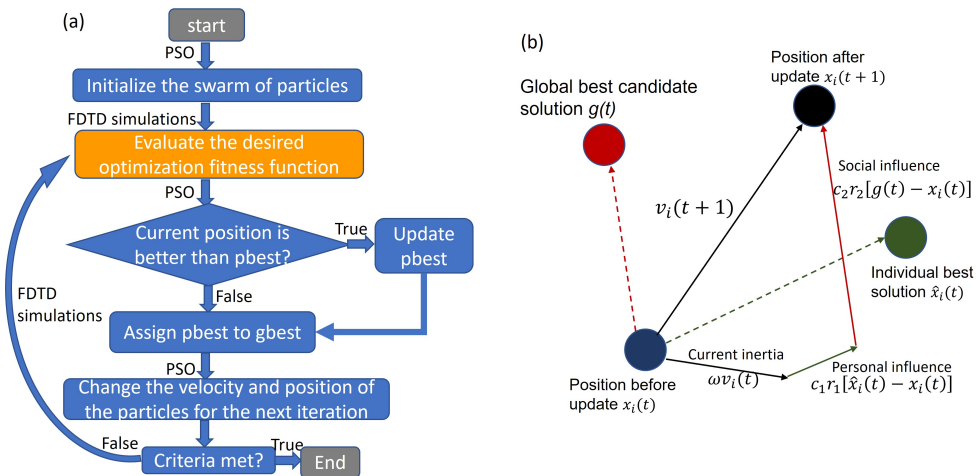
Figure 1.11: (a) Flowchart of the PSO algorithm. (b) Each individual particle i is accelerated in each time step toward the location of the best global solution gbest, and the location of its own personal best pbest.

Based on the above definitions, the first step toward implementation of the PSO is to select the parameters that need to be optimized and give them a reasonable range in which to search for the optimal solution. This requires the specification of a minimum and maximum values for each parameter in a N-dimensional optimization (N is the number of parameters). Then, the critical step is the definition of a fitness Function or FoM that

provides the link between the optimization parameters and the physical world. In general, a single number can be obtained that accurately represents the goodness of the solution. After definition the search space and fitness function, the PSO algorithm can be initiated as pictorially described in the flow chart of Fig. 1.11. To begin searching for the optimal position in the solution space, each particle begins at its own random location with a velocity that is random both in direction and magnitude. Then, FDTD is used to evaluate the goodness of each particle's position. Since the initial position is the only location encountered by each particle at start of the PSO, this position becomes the respective pbest for each particle. The first gbest is then selected from among these initial positions. Each particle must then move through the solution space as if it was a bird in a swarm. The algorithm acts on each particle one by one, moving it by a small amount and cycling through the entire swarm. The manipulation of the velocity of a particle is the main element of the entire optimization, which is accelerated towards its previous best position (pbest) and towards the best solution of the group (gbest) according to the following equation:

$$v_i(t+1) = \omega v_i(t) + c_1 r_1 [\vec{x}_i(t) - x_i(t)] + c_2 r_2 [g(t) - x_i(t)] , \quad (1.40)$$

where $v_i(t+1)$ is the velocity of i particle at $t+1$, which is determined by its inertia speed at t, $v_i(t)$, with an inertial weight ω, the distance of the individual best solution $\vec{x}_i(t)$ to its location with a cognitive factor c_1, and the distance of global best solution at time t ($g(t)$) to the current location with a social factor c_2. Both cognitive acceleration and social acceleration are stochastically adjusted by the random weights r_1 and r_2. Thus, the position of particle i is updated based on the above velocity as shown in Fig. 1.11 (b) and given by

$$x_i(t+1) = x_i(t) + v_i(t+1) . \quad (1.41)$$

After the positions of all the particles in the swarm are updated, FDTD simulations perform evaluations and corrections are made to the positions of pbest and gbest before the next updating. If the FoM value is greater than the value at the respective pbest for one particle, or the global gbest, then these locations are replaced with the current locations. This process is repeated by the PSO until a termination criterion is met. There are different ways of defining this termination criterion according to the analysis of a specific physical problem. A widely applicable method is the convergence to the global best position for the whole swarm. Usually, we set a maximum number of iterations, for example 50 or 100. The optimization stops when this number of iterations is reached.

PSO has been successfully applied in many research and application areas. Since Jacob Robinson and Yahya Rahmat-Samii introduced the PSO to the electromagnetic community in 2004 [81], several studies on optical instruments have relied on this powerful computational evolutionary optimization approach. In 2005, Massimo Donelli and Andrea Massa proposed PSO for the solution of the inverse-scattering problem that arise in microwave-imaging applications [82]. In recent years, the PSO has been used to find the values of parameters that optimally match the impedance of micro-bolometers for nanoantenna-based infrared detectors [83], simplify the development of a high-performance digital optical phase conjugation systems [84], and retrieve a high

performance reflection in the visible [85]. For this thesis, we have used the PSO algorithm in the nanophotonic design for optical and optoelectronic applications.

1.8   Outline of this Thesis

Besides this introduction, the thesis is organized as follows: in chapter two, we present a detailed theoretical investigation of collective resonances in lattices of dielectric nanoparticles, which give us an overall understanding of the characteristics of these resonances for various applications throughout the thesis. Two kinds of collective resonances in square arrays of silicon nanoparticles are described. The first are electric and magnetic SLRs, which originate from the radiative coupling of localized resonances in the individual nanoparticles when the silicon nanoparticle array is homogeneously embedded in a dielectric material. When the dielectric nanoparticle array in embedded in an optical waveguide, electric and magnetic quasi-guided modes can be also observed. Both, SLRs and quasi-guided modes exhibit narrow line widths and high electromagnetic field enhancements that are demonstrated by the spatial field distributions. The author contributed to developing and performing simulations and the associated data analysis.

By applying the PSO algorithm and FDTD simulations, in chapter three we optimize the sensitivity of optical hydrogen sensors based on SLRs in palladium nanoparticle arrays. This work was done in collaboration with Dr. Ferry Nugroho and Dr. Andrea Baldi for the Vrij Universiteit Amsterdam. The optimization is experimentally demonstrated with a sensor capable of detecting hydrogen gas down to the ppb level. We employ the PSO algorithm for nanophotonic design to find optical structures with the highest possible FoM that represents the sensitivity of the optical hydrogen sensor. The author edited the PSO algorithm code in the Lumerical FDTD platform and performed all the simulations and optimizations, and a series of numerical characterizations of optimal sensors.

In chapter four, the PSO algorithm is used to optimize the coupling strength between excitons in poly(3-hexylthiophene-2,5-diyl) (P3HT) and SLRs in open cavities defined by arrays of aluminum nanoparticles. P3HT is an electron-donor polymer, widely employed in organic photovoltaics. We have determined the optimal size and lattice constant of square arrays of Al nanoparticles, retrieving a maximum Rabi splitting of 0.8 eV in these open optical cavities. Samples have been fabricated with the optimized dimensions, and the optical extinction dispersion has been measured, showing the formation of exciton polaritons in the strong coupling limit. This work illustrates an efficient approach to optimize resonant structures for light–matter interaction in open systems that can be used in polaritonic devices. The author was the major contributor to this work by performing all simulations and optimizations, data analysis and writing the related manuscript.

In chapter five, the short-circuit current density (J_{sc}) enhancement of organic solar cells is optimized with PSO design of periodic nanoparticle arrays and holes arrays acting as electrodes. Compared to the large optical losses of plasmonic hole array electrodes that reduce the J_{sc} of the device, A 20% enhancement of J_{sc} has been achieved for the solar cell with an optimized nanoparticle array electrode. Moreover, we spectrally and spatially investigate the electric field enhancement in the whole device and illustrate that surface

plasmon polaritons excited by the diffraction of the nanoparticle array play an ambivalent role for absorption enhancement and red-shift of the optical gap. The author was the major contributor to this work by performing all simulations and optimizations, data analysis and writing the related manuscript.

The last chapter of this thesis is dedicated to the study of the localized and hybrid plasmonic resonances supported by randomized and periodic silver nanodisks arrays on a thin HfO_2 dielectric layer and silver film. Surface plasmon polaritons (SPPs) can be excited by the diffraction of the incident polarized light from the periodic nanodisk arrays. Furthermore, a hybrid plasmonic mode was observed, which originates from the coupling of the SPP resonance and dark gap mode. A feature similar to bound states in the continuum (BIC) emerges in this hybrid mode due to the dark gap mode at normal incidence. The author performed all simulations and contributed to the interpretation of the measurements. She also had a major role in writing the related manuscript.

LATTICE RESONANCES IN DIELECTRIC METASURFACES

We present a numerical investigation of collective resonances in lattices of dielectric nanoparticles. These resonances emerge from the enhanced radiative coupling of localized Mie resonances in the individual nanoparticles. We distinguish two similar systems: a lattice of silicon nanoparticles homogeneously embedded in a dielectric and a lattice of silicon nanoparticles in an optical waveguide. The radiative coupling is provided by diffraction orders in the plane of the array for the former system or by guided modes in the optical waveguide for the latter one. The different coupling leads to distinct lattice resonances in the metasurface defined by the array of silicon nanoparticles. These resonances have been extensively investigated in metallic nanoparticle arrays, but remain highly unexplored in fully dielectric systems. We describe the pronounced differences in the intensity enhancement and field distributions for the two systems, providing valuable information for the design and optimization of optical components based on dielectric lattice resonances.

2.1   Introduction

Our capacity of structuring matter at the nanoscale has opened a myriad of possibilities for applications at optical frequencies. The resonant response of nanostructures at these frequencies leads to local field enhancements, increased light-matter interaction, enhanced non-linearities and high sensitivity to small perturbations. These phenomena can be exploited for optical detection, light emission, light harvesting and sensing. [86] A significant scientific effort has been made over the past decades in controlling and enhancing the optical response of metallic nanoparticles. [87] The nanoparticles support coherent oscillations of free electrons, known as localized surface plasmon polaritons, which can locally enhance electromagnetic fields in tiny volumes. [88] Intrinsic to metals are Ohmic losses due to the complex conductivity of real metals. In order to suppress these losses, more recent research has focused on low loss and high refractive index dielectric nanostructures supporting Mie resonances at optical frequencies. [68, 89–91] These resonances, arising from displacement currents in the dielectric nanostructures, also lead to high local field enhancements and low optical losses. [92] Moreover, compared with plasmonics, dielectric nanostructures can exhibit both electric and magnetic resonances. [93–96]

Real applications typically require field enhancements over larger volumes than those of single resonant nanoparticles. Metasurfaces and periodic lattices have emerged as systems formed by resonant nanoparticles with unusual characteristics emerging from their collective response. [97] Arrays of metallic nanoparticles supporting collective resonances have received significant attention due to their remarkably narrow line widths (high Q-factors),[40, 41, 98, 99] low radiation losses, and high field enhancements over large volumes. [100] These collective resonances originate from the radiative coupling of localized resonances in the individual nanoparticles. This radiative coupling can be enhanced by diffraction orders in the plane of the arrays, known as Rayleigh anomalies (RAs), or by optical guided modes in thin dielectric layers. Collective resonances emerging from RAs are known as Surface Lattice Resonances (SLRs), [57–60] while those emerging from guided modes are knows as waveguide polaritons or quasiguided modes (GQMs), [101–103] although they are usually not distinguished from SLRs in the literature. The high Q-factor of collective resonances has been the reason from proposing them in applications, such as sensing, [104–106] spectroscopy, [107] surface-enhanced Raman spectroscopy, [52, 108] solid-state lighting, [48, 109] etendue reduction, [110] and lasing. [111–113] Similar to single nanoparticles, collective resonances in arrays of dielectric and semiconductor resonant nanoparticles have been recently proposed as alternative to resonances in metallic arrays. [68, 70, 71, 114]

In this chapter, we present a detailed theoretical investigation of collective resonances in arrays of resonant silicon (Si) nanoparticles using finite-difference time-domain (FDTD) simulations. Their narrow line width allows to clearly resolve the collective resonance emerging from the diffraction enhanced radiative coupling of electric and magnetic resonances, which overlap in single nanoparticles. We illustrate the notorious differences between SLRs and quasi-guided modes in Si nanoparticle arrays. Near-field simulations illustrate the strong electromagnetic field confinements that result in the collective resonances. We specially consider the field enhancement as a function of the distance to the

nanoparticles. For an illumination along the normal direction to the surface, this field enhancement represents the eventual enhanced absorption that a material will experience at a particular height. It also provides the fractional local density of states or the efficiency at which the material will emit in the normal direction.

2.2 Single Silicon Nanoparticle

We first describe the optical resonances supported by individual Si nanoparticles. The optical constants of Si are taken from Palik. [115] The nanoparticles have a cylindrical shape and are embedded in fused silica with constant refractive index $n = 1.46$. We select the height of the particle so that both electric and magnetic multipoles are supported, specifically the lowest order modes, i.e. the electric dipole (ED) and magnetic dipole (MD). The ED arises from the displacement current along the polarization of the incident electric field. The MD requires field retardation in the particle along the propagation direction of the incident wave, such that a displacement current loop is formed, leading to a magnetic field. [91, 116]If the nanoparticle is too shallow the field retardation is not sufficient to build a current loop. From calculations not shown here, we have determined that a height of 100 nm satisfies this requirement and, therefore, we fix the nanoparticle height to this value.

We have calculated the scattering and absorption efficiencies, i.e. the ratio of the scattering (absorption) cross-section to the geometrical cross-section of the particle, for cylinder diameters in the range 70-160 nm (Fig. 2.1 (a) and Fig. 2.1 (b), respectively). A total-field scattered-field (TFSF) plane wave illumination (see Sec. 2.6) is used with a broadband spectrum, which is incident from below along the height of the particle. The scattering efficiency in Fig. 2.1 (a) exhibits a strong peak that red-shifts when the diameter is increased. This peak corresponds to the MD resonance. The peak is not symmetric and presents a shoulder at shorter wavelengths, which is attributed to the ED resonance. The spectral overlap between the MD and ED resonances is a consequence of the refractive index of the surrounding medium that increases the radiative losses and broadens the resonances. [91] For diameters larger than 120 nm, other peaks appear at shorter wavelengths, which are attributed to higher order modes.

Compared to the scattering, the absorption efficiency (Fig. 2.1 (b)) in the silicon nanoparticles decreases as the diameter is increased. The high absorption at shorter wavelengths and small diameters is not caused by interband transitions on Si and is attributed to the interaction of the particle with the electromagnetic fields, as described by Mie theory. [117] The real and imaginary components of the electric and magnetic multipole moments have different dependence on the particle size. The absorption at short wavelengths for small diameters is attributed to the magnetic and electric dipole resonances, while for larger diameters is due to higher order modes. Aside from these absorption peaks, we note that in the range of 600-700 nm the absorption losses are particularly low. This makes silicon nanoparticles suitable structures for the design of lattice resonances in this spectral range.

The ED and MD resonances can be identified calculating the spatial distribution of the
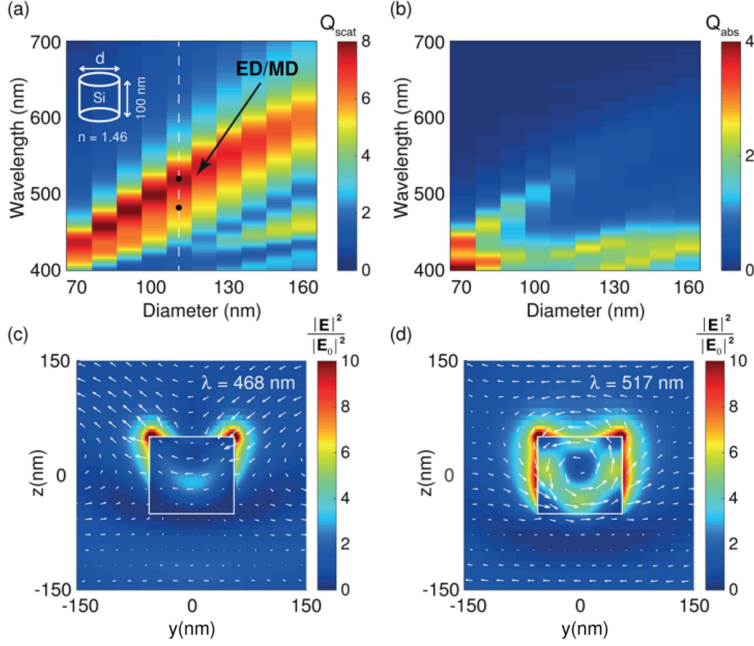
Figure 2.1: FDTD simulations of the optical response of a silicon cylinder embedded on fused silica (n = 1.46). Scattering (a) and (b) absorption efficiencies, Q_{scat} and Q_{abs}, respectively, for a silicon cylinder with h = 100 nm and diameter d = 70-160 nm. The cylinder is illuminated along its height from below with a broad-band (λ = 400 - 700 nm) beam. The main band of enhanced scattering observed in (a) corresponds to the magnetic and electric dipole resonances, indicated as ED/MD by the black arrow. For the particle with diameter d = 110 nm (white dashed line in (a)), the spatial distribution of the normalized electric field intensity $|\mathbf{E}|^2$, normalized to the incident field intensity $|\mathbf{E}_0|^2$, is calculated on the yz−plane for the wavelengths λ = 468 nm (c) and λ = 517 nm (d), which correspond with the two black dots in (a). The color scale represents the intensity and the white arrows represent the real part of the vectorial electric field projected in the yz−plane. The shape of the particle is denoted with the white rectangle. The center of the nanoparticles is considered as the zero in the yz−plane.

electric field intensity enhancement relative to the incident field intensity. We take the diameter value of d = 110 nm, indicated in Fig. 2.1 (a) by the white dashed line, and calculate the field distribution in the yz−plane for the two wavelengths corresponding to the MD and ED resonances, incidated by the black dots in Fig. 2.1 (a). The color scale for both Fig. 2.1 (c) and Fig. 2.1 (d) represents the field intensity and the white arrows represent the real part of the vectorial electric field projected in the yz−plane. For the ED resonance, the electric field in Fig. 2.1 (c) shows no circulation and is to a large extent oriented parallel to the incident electric field. The near-field outside the particle is distorted with respect the typical near-field created by a pure electric dipole in a disk and is a consequence of the retardation effect inside the particle. In Fig. 2.1 (d) we can see that the

electric field circulates inside the silicon particle, and thus corresponds with the magnetic dipole resonance.

2.3 Surface Lattice Resonances (SLRs)

SLRs arise from the enhanced radiative coupling of particle resonances by the in-plane diffraction orders of the lattice. For simplicity, we call these diffraction orders Rayleigh anomalies (RAs) in reference to the condition at which a diffraction order becomes evanescent at the interface separating two media. To investigate these resonances, we arrange the particles in an infinite periodic array with hexagonal geometry. We simulate this array embedded in a symmetric environment, i.e., with a substrate and superstrate with the same refractive index ($n = 1.46$). This condition maximizes the radiative in-plane coupling between particles due to phase matching of the in-plane diffraction orders in the lower and upper media. A schematic representation of the array is shown in Fig. 2.2 (a).

To tune the frequency of the SLRs to a particular spectral range, we have to consider the coupling strength between the optical resonances of the individual silicon cylinders to the RA. This coupling determines the redshift of the SLR with respect to the RA and its line width. The position of the RA can be calculated using the grating equation:

$$\pm \vec{k}_{\|d} = \vec{k}_{\|i} + \vec{G}, \tag{2.1}$$

where $\vec{k}_{\|d}$ is the wave vector for the in-plane diffracted orders, $\vec{k}_{\|i}$ is the in-plane projection of the incident wave vector $\vec{k}_i$, and $\vec{G}$ is the reciprocal lattice vector of the hexagonal array. If we choose a periodicity $a = 485$ nm, we find that the first order RA happens at 613 nm for normal incidence ($k_{\|i} = 0$). The optical resonances of single Si cylinders with diameters between 80 nm and 110 nm are sufficiently detuned from the RA (see Fig. 2.1 (a)). For these diameters, we use FDTD simulations (see Sec. 2.6) to calculate the optical extinction of the array, defined as 1 - T, where T is the zero order transmittance for a plane-wave incident normal to the array plane from below. The results are displayed in Fig. 2.2 (b) for the wavelength range 400-700 nm. A series of peaks around 600-650 nm can be seen, in addition to the optical resonances of the individual particles at shorter wavelengths. These spectral features, not present in the spectrum of individual silicon particles, correspond to the SLRs and are shown in more detail in Fig. 2.2 (c). We can see several peaks that redshift and broaden as the diameter of the nanoparticles increases. This behavior corresponds to a stronger coupling between the single particle resonances and the RA as their detuning is decreased - note that changing the particle diameter shifts the localized resonances of the individual nanoparticles, but does not change the RA, which depends on the lattice constant. The most relevant feature in the extinction spectra is the emergence of a second SLR for $d > 90$ nm, which increases in intensity and redshifts with the diameter in a similar fashion as the first SLR at longer wavelengths. The formation of two collective resonances in the array has its origin in the electric and magnetic dipole resonances of the single nanoparticles. This result was already demonstrated by Evlyukhin *et al.* using a coupled-dipole model for both the electric and magnetic dipoles. [68] The total induced electric (magnetic) dipole moment of an individual nanoparticle in the array is the sum of the

induced electric (magnetic) dipole moment by the incident field in this particle and by the rest of the particles in the array. At a particular wavelength, this leads to the coherent and collective magnetic response of the array. Along with the formation of two SLRs, we note their highly symmetric line profile. Typically, SLRs exhibit an asymmetric line shape - Fano resonance [118]- which results from the interference between the broad resonance in the individual nanoparticles and the narrow resonance given by the RA. In our system this interference is small due to the large detuning between these two resonances.
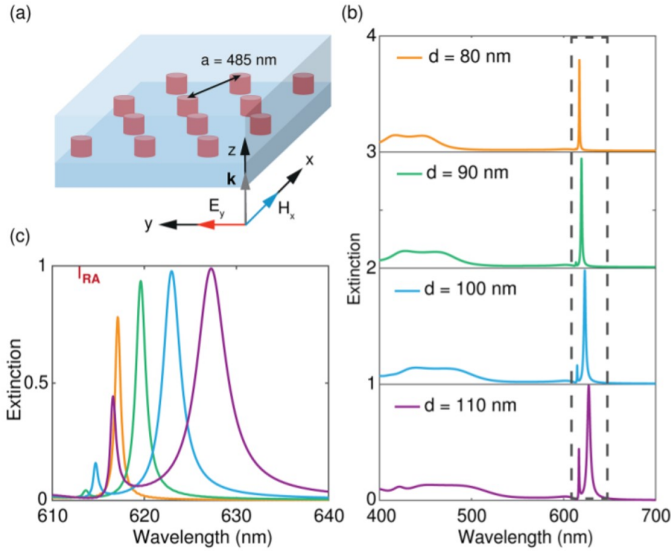
Figure 2.2: Surface lattice resonances in an infinite periodic array of dielectric nanoparticles. (a) Schematic representation of the geometry: a hexagonal array with periodicity $a = 485$ nm formed by Si nanoparticles with a height $h = 100$ nm, embedded in fused silica ($n = 1.46$). The array is illuminated with a broadband ($\lambda = 400$ - 700 nm) beam incident normal to the array plane from below. The polarization of the incident electric and magnetic fields is along the $y-$ and $x-$axis, respectively. The extinction spectra are shown in (b) for arrays with different nanoparticle diameters, $d = 80$, 90, 100 and 110 nm. The spectra are offset by unity for clarity. The dashed grey rectangles show the SLRs in these arrays, which are plotted in (c), with the RA indicated for the period of $a = 485$ nm.

To identify the nature of the SLRs in Fig. 2.2 (c), we investigate the spatial distribution of the electric and magnetic field intensity enhancement relative to the incident field intensity. We focus on the array of particles with diameter $d = 110$ nm, as this array exhibits both SLRs. The electric and magnetic field profiles on the $yz-$plane are shown in Figs. 2.3 (a) and (c) for the SLR at 617 nm, and in Figs. 2.3 (b) and (d) for the SLR at 627 nm. The color scale represents the magnetic and electric field intensity enhancement, in logarithmic scale, while the black arrows are the real components of the vectorial electric and magnetic fields projected in the $yz-$plane. At $\lambda = 617$ nm, the circulation of the electric fields results in strong magnetic fields inside the silicon particle (Fig. 2.3 (c)). These fields indicate that the SLR at 617 nm arises from the collective coupling of magnetic dipoles in the nanopar-

ticles, and we label this resonance as MD-SLR. In Fig. 2.3 (b) the electric field is aligned with the incident field and the intensity shows a dipolar field pattern. Therefore, the SLR formed at 627 nm corresponds to the collective coupling of electric dipoles in the nanoparticles, and we label it as ED-SLR. Note that induced electric and magnetic dipole moments inside the Si particle for the ED-SLR and MD-SLR, respectively, are oriented orthogonal to each other along the direction of the incident fields. This result is also observed in the couple-dipole model for infinite arrays and implies an orthogonality relation between the ED-SLR and MD-SLR at normal incidence.[68] Compared to the local fields of the ED and MD resonances in the single particle illustrated in Fig. 2.1 (c) and (d), the electric and magnetic fields for both ED-SLR and MD-SLR show a strong intensity enhancement, which is confined near the array plane. This in-plane confinement is attributed to the diffracted orders grazing to the sample which are responsible for the enhanced radiative coupling of the nanoparticles.
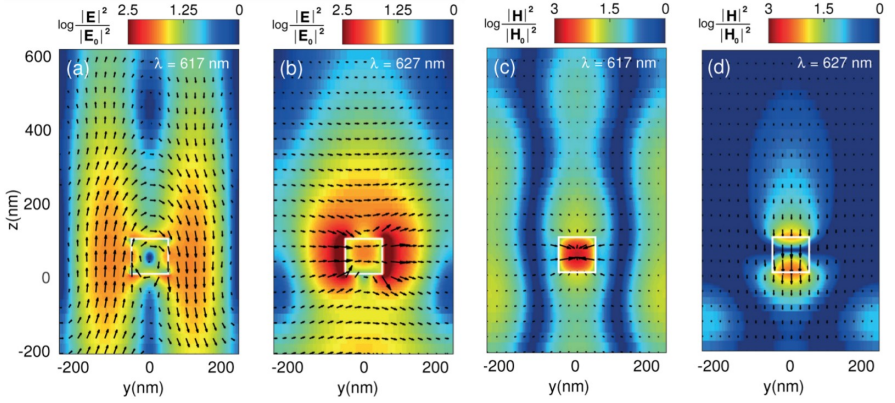
Figure 2.3: FDTD simulations of the spatial distribution of the electric field $|\mathbf{E}|^2$ and magnetic field intensities $|\mathbf{H}|^2$, normalized to the incident field intensity ($|\mathbf{E_0}|^2$ and $|\mathbf{H_0}|^2$, respectively), in the yz−plane of a unit cell of the array with particle diameter d = 110 nm. The color scale represents the magnetic and electric field intensity enhancement, in logarithmic scale, while the black arrows are the real components of the vectorial electric and magnetic fields projected in the yz−plane. The shape of the Si nanoparticles is indicated with the white rectangles. The refractive index is the same everywhere outside the particle (n = 1.46). Figures (a) and (c) correspond to the SLR at λ = 617 nm, while figures (b) and (d) correspond to the SLR at λ = 627 nm. The simulations of the fields are performed with the same illumination conditions than in Fig. 2.2, i.e. with a plane wave normally incident to the array plane from below. The bottom of the nanoparticles is considered as the zero in the z−axis.

The simulated arrays present a MD-SLR blue-shifted with respect to the ED-SLR. This blue-shift indicates that the coupling strength between the RA and the magnetic dipole resonance is smaller than in the case of the electric dipole resonance. We can also observe this different coupling in the spatial distribution of the magnetic field intensity in Fig. 2.3 (c): Although the intensity is much higher than in 2.3 (d), it is mainly located inside the silicon nanoparticle. However, the magnetic and electric fields of the ED-SLR are extended

outside the nanoparticles with larger intensities. It is important to stress that the coupling strength can be tuned with both the periodicity (i.e. the RA) and the geometry of the nanoparticles (i.e. the Mie resonances). In rectangular arrays, the periodicities in the x- and y-directions allow to tune separately the coupling for ED-SLR and MD-SLR, as their orthogonality relation means that they couple along perpendicular directions. Therefore, it is possible to achieve a cross-over between the ED-SLR and MD-SLR and invert the spectral position of the ED-SLR respect to the MD-SLR. [71, 96, 119]

To demonstrate the potential of SLRs in dielectric arrays to interact with thin layers of optically active materials, we have calculated the total intensity enhancement (IE), also known as excitation enhancement. [120] The IE is defined as the integral of the field intensity enhancement over the volume or area occupied by the material, normalized to a reference without the nanoparticle array. Specifically, we aim to illustrate the dependence of the IE with the distance to the particle array plane, which corresponds to situation in which the SLRs interact with planar and thin-layer materials. [121] Therefore, we discretize the IE as a surface integral in the $xy-$plane that is evaluated as a function of the position z and wavelength:

$$IE(z,\lambda) = \frac{\int_A |E(x,y,z,\lambda)|^2 dx dy}{\int_A |E_{ref}(x,y,z,\lambda)|^2 dx dy}, \qquad (2.2)$$

where $E(x,y,z,\lambda)$ is the electric field at wavelength λ and position z when the nanoparticle array is present, and $E_{ref}(x,y,z,\lambda)$ corresponds to the electric field in the absence of the array. The integrals are evaluated in a unit cell of the array with area A. The same method can be used to calculate the IE of the magnetic field. However, from the simulations shown in Fig. 2.3, we concluded that most of the MD-SLR enhancement is inside the Si nanoparticles, which makes it inaccessible to magnetic field active materials. Consequently, we focus on the electric field. For optically active materials, such as molecular dyes and quantum dots, with transition dipole moments randomly oriented, the modulus of $|E(x,y,z,\lambda)|$ includes the three field components, E_x, E_y and E_z. We have also considered the coupling of the SLRs to two dimensional materials (e.g., 2D transition metal dichalcogenides or quantum wells), for which the optical transitions have dipole moments confined in the plane. In this case, only the projected components of $E(x,y,z,\lambda)$ in the $xy-$plane are evaluated in the integral. Further, the integral excludes the area of the unit cell occupied by the silicon particles.

Simulations of the IE for the array with a = 485 nm, h = 100 nm, and d = 110 nm are shown for the MD-SLR and ED-SLR in Fig. 2.4. The red curves are calculations including the three components of the electric field in the IE, while the blue curves include only the in-plane components. The grey area indicates the points where the integral excludes the electric fields inside the nanoparticles. The nanoparticle upper boundary leads to the small peaks observed in Figs. 2.4 (a) and (b) at z = 100 nm. We can see for the MD-SLR in Fig. 2.4 (a) that the IE is mainly for the $z-$component of the electric field. This response is attributed to the diffraction enhanced coupling between magnetic dipole moments oriented along the $x-$axis. Since the electric field is given by the curl of the magnetic field, this creates a field strongly oriented in the direction perpendicular to the $xy-$plane. In
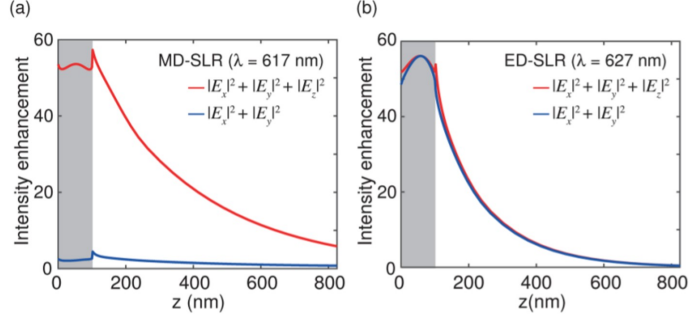
Figure 2.4: Intensity enhancement for the MD-SLR (a) and the ED-SLR (b) in a hexagonal array of Si nanoparticles. The array has a period a = 485 nm and the nanoparticles have height h = 100 nm and diameter d = 110 nm. The red curves are calculations including the three components of the electric field, and the blue curves include only the in-plane components. The pale grey area represents the positions in which the integration excludes the electric fields inside the nanoparticles. The FDTD simulation uses the same illumination conditions as in previous figures. For the reference, the same structure and illumination is considered but without the array.

contrast, the ED-SLR in Fig. 2.4 (b) has the IE mainly in the $xy-$plane, which corresponds with the diffraction enhanced coupling between electric dipole moments in the $xy-$plane.

By virtue of this particular field orientation of the MD-SLR and the ED-SLR, we note that materials with different orientations in transition dipole moments will couple preferentially to one of the two SLRs. In addition, we can see from these calculations, that such IE would enhance the absorption of the material if it overlaps spectrally and spatially with the SLR. Further, the IE also provides information about the directivity of the emission of emitters coupled to SLRs: Using Lorentz reciprocity theorem, the emission probability of a dipole in certain direction, i.e. the fractional radiative local density of states (FLDOS), is proportional to the local field enhancement produced by an illuminating beam incident in that direction. [70, 121, 122] Therefore, layers of emitting materials positioned at the height of maximum field enhancement will radiate in the direction normal to the surface.

2.4   Quasiguided Modes (QGMs)

Unlike SLRs, which are favored when the array of nanoparticles is embedded in an homogeneous dielectric, quasiguided modes (QGMs) need a waveguide structure with a higher refractive index than the surrounding medium. Without the periodic array of scatterers, guided modes lie outside the lightcone, decoupled from the radiation modes as consequence of the momentum mismatch. An array of particles acts as a grating coupler, providing to radiative modes the required momentum to couple to guided modes. [101, 103] This makes possible the excitation of guided modes, but by the same argument, such modes are now leaky and couple out to free space propagating modes. Hence, the term "quasiguided".
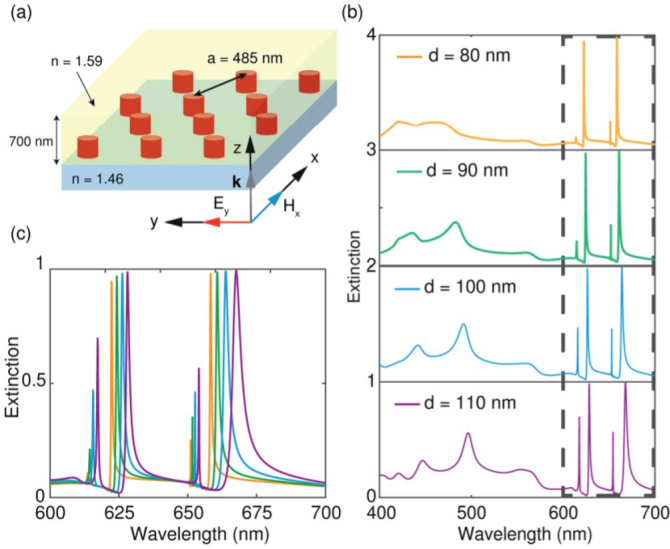
Figure 2.5: Quasiguided modes and surface lattice resonances in an infinite periodic array of Si nanoparticles coupled to a waveguide. (a) Schematic representation of the geometry: a hexagonal array with periodicity a = 485nm, formed by Si nanoparticles with height h = 100 nm on top of a fused silica substrate (n = 1.46), and embedded in a waveguide (n = 1.59). On top the waveguide there is an infinite layer of air (n = 1). The array is illuminated with a broadband (λ = 400 - 700 nm) beam incident normal to the array plane from below. The polarizations of the incident electric and magnetic fields are along the $y-$ and $x-$axis, respectively. The extinction spectra are shown in (b) for different diameters of the nanoparticles, d = 80, 90, 100 and 110 nm. The curves are offset by unity for clarity. The dashed grey rectangle indicates the region of interest with several QGMs that is plotted in (c).

Although quasiguided modes have been observed in plasmonic particle arrays, their excitation is possible using dielectric scatterers as the silicon cylinders studied here. [103, 114] The proposed structure is shown schematically in Fig. 2.5 (a) and consists of a hexagonal array with a = 485 nm, where the Si nanoparticles, with h= 100 nm, are placed on top of a fused silica substrate (n = 1.46). On top of the substrate and embedding the particles, there is a slab waveguide with n = 1.59 and a thickness of 700 nm, and on top of this waveguide, there is an infinite layer of air (n = 1). The value of the waveguide thickness is considered so that there are quasiguided modes supported in the wavelength range of 600-700 nm. As with the RAs, the coupling strength between guided modes and the single particle resonances is determined by the detuning between them. Consequently, and following the same argument than in the section 2.3, we vary the diameter of the Si particles in the range 80-110 nm. The extinction results from the FDTD simulations are illustrated in Figs. 2.5 (b) and (c) for a plane wave like illumination incident from the substrate along the normal direction (see Sec. 2.6). The different spectra exhibit a rich diversity of resonances. If we focus on Fig. 2.5 (b) in the range of 400-600 nm, where the
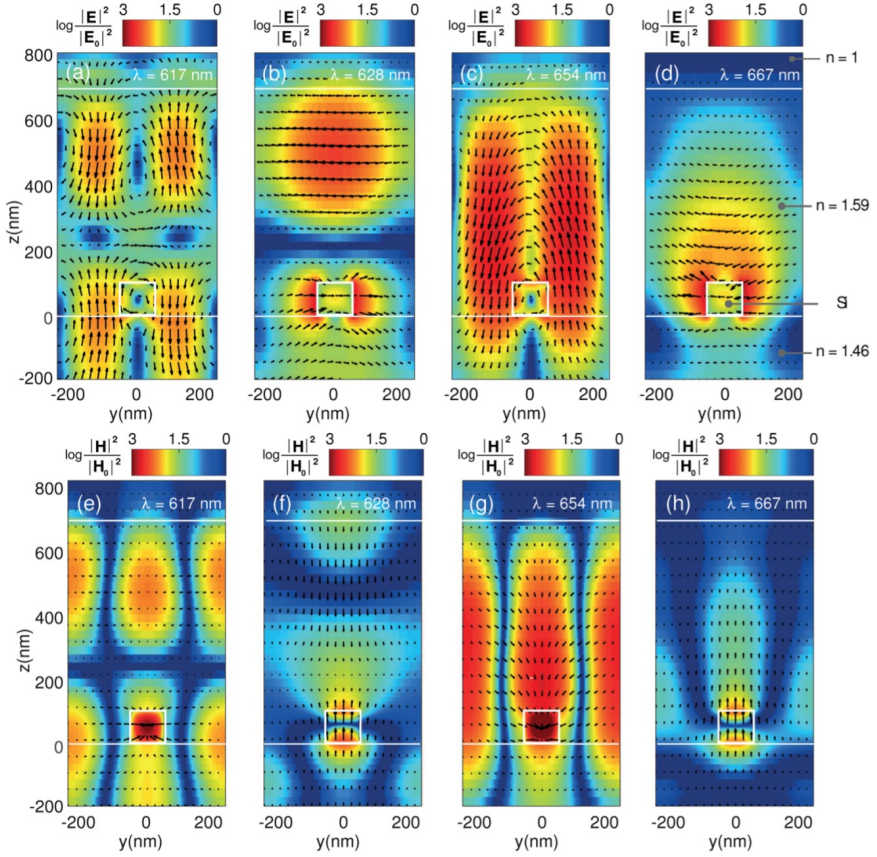
Figure 2.6: FDTD simulations of the spatial distribution of the electric field $|\mathbf{E}|^2$ and magnetic field intensities $|\mathbf{H}|^2$, normalized to the incident field intensity ($|\mathbf{E_0}|^2$ and $|\mathbf{H_0}|^2$, respectively), in the $yz-$plane of a unit cell of the array-waveguide system with particle diameter $d = 110$ nm. The color scale represents the magnetic and electric field intensity enhancement, in logarithmic scale, while the black arrows are the real components of the vectorial electric and magnetic fields projected in the $yz-$plane. The shape of the Si nanoparticles is indicated with the white rectangles. The white lines indicate the boundaries of the waveguide. The top figures (a-d) show the electric field and the bottom figures (e-h) show the magnetic fields. The figures are shown in order of increasing wavelength: (a,e) for $\lambda = 617$ nm (first resonance); (b,f) for $\lambda = 628$ nm (second resonance); (c,g) for $\lambda = 654$ nm (third resonance); and (d,h) for $\lambda = 667$ nm (fourth resonance). The simulations of the fields are performed with the same illumination conditions as in Fig. 2.5, i.e. with a plane wave normally incident to the array plane from below. The bottom of the nanoparticles and the waveguide is considered as the zero in the $z-$axis.

Mie resonances of individual silicon particles are excited, we now see several peaks that shift and increase as the diameter increases. These resonances are attributed to high order quasiguided modes that couple to the Mie resonances. Considering that radiative and

35

absorption losses increase for the silicon particles at shorter wavelengths (Fig. 2.1 (a) and (b)), we focus on the range of 600-700 nm, where we find several collective resonances. We can see in Fig. 2.5 (c) two main resonances with large extinction next to weaker resonances with very narrow line widths. These four peaks redshift and broaden as the diameter of the particles is increased, with a pronounced increase in extinction for the weaker resonances. Further, the two largest peaks have an asymmetric profile not observed when the environment has an homogeneous refractive index (see Fig. 2.2 (c)). The reason of this asymmetry lies in the interference between the collective mode and light that is reflected back and forth inside the waveguide.

The resonances in a grating-waveguide system can be predicted analytically by combining Eq. (2.1) with the phase condition for constructive interference in the waveguide. However, this model assumes the grating elements to be small and with low scattering efficiency, which is not the case for our system. The presence of the nanoparticles changes drastically how light propagates inside the waveguide. In addition, the different refractive index of the particle also changes the optical path of a light ray compared to the waveguide without the array. Therefore, to understand the nature of the four resonances observed in the spectral range of 600-700 nm in Fig. 2.5 we simulate the spatial distribution of the electric and magnetic fields. We focus again on the array of Si nanoparticles with $d = 110$ nm. In Fig. 2.6, we show the electric and magnetic field intensity enhancement (relative to the incident field) for the four resonances in the $yz-$plane of the simulation unit cell, and for the same illumination conditions as in Fig. 2.5. The color scale represents the intensity enhancement of the electric and magnetic fields in a logarithmic scale. The black arrows represent the real part of the vectorial fields projected in the $yz-$plane. The shape of the Si cylinder is indicated with the white rectangle and the white horizontal lines indicate the boundaries of the waveguide. We can see that both the electric (Figs. 2.6 (a)-(d)) and magnetic (Figs. 2.6 (e)-(h)) fields are strongly confined inside the waveguide. The narrow resonances at $\lambda = 617$ nm (Figs. 2.6 (a) and (e)) and $\lambda = 654$ nm (Figs. 2.6 (c) and (g)) show circulation of the electric field, a signature of a magnetic mode, which is confirmed by the strong magnetic fields observed in Figs. 2.6 (e) and (g)). Compared with the resonance at $\lambda = 654$ nm, we can observe for $\lambda = 617$ nm in Fig. 2.6 (a) that there are two regions around which the electric field has circulation, one in the bottom of the waveguide, along the array plane; and the other in the upper part of the waveguide. Moreover, the circulation in the upper part is opposite to the circulation in the bottom. As result, the magnetic field created is antisymmetric in the waveguide along the $z-$axis. Given that the magnetic field is strongly oriented in the $x-$axis, we can identify this resonance at $\lambda = 617$ nm with a first order quasi-guided TM mode, while the resonance at $\lambda = 654$ nm corresponds to the fundamental quasiguided TM mode. [123] We label them as TM_0 and TM_1.

We turn now our focus to the resonances at $\lambda = 628$ nm (Figs. 2.6 (b) and (f)) and $\lambda = 667$ nm (Figs. 2.6 (d) and (h)). The electric field shows an strong enhancement for $\lambda = 628$ nm (Fig. 2.6 (b)) in the waveguide and around the nanoparticle. From the $yz-$plane projection of the electric field, represented by the black arrows, we can observe that the electric field is mainly oriented along the $y-$axis inside the waveguide and that has an antisymmetric behaviour along the $z-$axis. This resonance resembles to a first order TE quasiguided mode that we label as TE_1. The resonance at $\lambda = 667$ nm should correspond then with
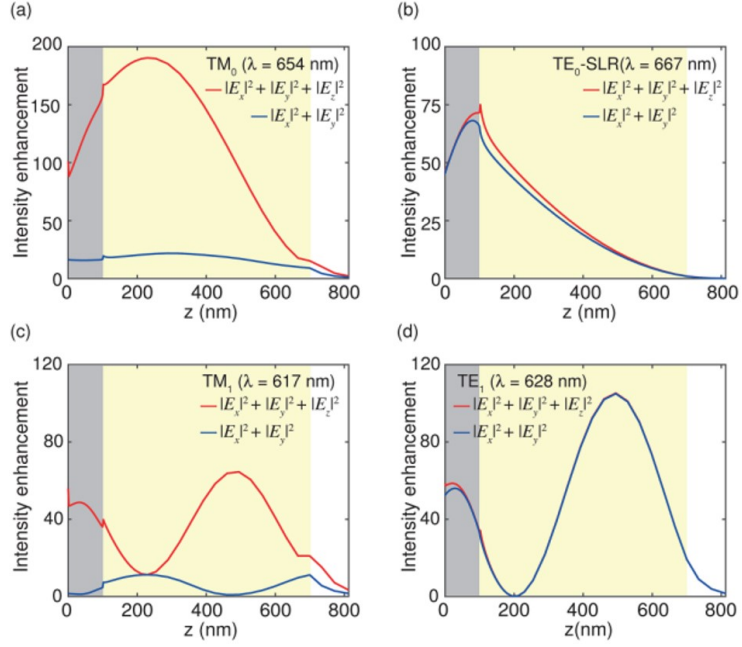
Figure 2.7: Intensity enhancement for the TM_0 (a), TE_0-SLR (b), TM_1 (c), and the TE_1 (d) QGMs in a hexagonal array of Si nanoparticles embedded in a waveguide of thickness $t = 700$ nm. The array has a period $a = 485$ nm and the nanoparticles have a height $h = 100$ nm and diameter $d = 110$ nm. The red curves are calculations including the three components of the electric field in the IE, and the blue curves include only the in-plane components. The waveguide is divided in the grey and yellow regions. The particles are included in the grey rectangle, and in this region the integration of the fields excludes the electric fields inside the particle. The yellow area represents the part of the waveguide without nanoparticle. The FDTD simulation uses the same illumination conditions as in previous figures. The reference consists an homogeneous fused silica environment without the array and the waveguide.

the fundamental quasiguided TE_0 mode. However, the electric field is mainly confined around the nanoparticles, resembling instead an ED-SLR. This result is consequence of the perturbation introduced in the spatial distribution of the fields by the scattering of the nanoparticles. Silicon particles scatter light in the waveguide in many directions, affecting to the phase relationship of the fields and their interference, which has to include now the scattered fields as well. For particles with a large scattering cross section, as the Si particles with diameter $d = 110$ nm, the perturbation is high, and the condition for in-phase accumulation of fields in the waveguide is not satisfied anymore. Radiative coupling between the particles, which depends on the phase relationship between in-plane scattered fields, is not affected and the result is that an ED-SLR-like mode is excited, that we label as TE_0-SLR. The transition between TE_0 and TE_0-SLR depends on the scattering cross section of

the particle. Decreasing the scattering cross section will reduce the perturbation and bring back the constructive interference in the waveguide. Such transition is possible since both TE_0 and ED-SLR have the same symmetry and are transverse-electric modes. The effect of the particle scattering on the spatial distribution of fields in QGMs has not been addressed in detail in the literature. [103, 121]

Next, we investigate the field enhancement (IE) associated to the quasiguided modes shown in Fig. 2.6 for the particle with diameter $d = 110$ nm. We have calculated the IE as a function of the vertical distance to the array at the resonance wavelengths using Eq. (6.5) and excluding the field inside the nanoparticles. Both the array and waveguide are considered as the resonant structure, so the reference consists of an homogeneous medium with identical refractive index than the substrate. To compare the results with the IE calculated for the homogeneous array, we focus on the electric field. We note, however, that the magnetic field enhancement is not negligible inside the waveguide for the TM_0 and TM_1 modes (see Fig. 2.6 (e) and (g)). The results of the IE are shown in Fig. 2.7. The red and blue curves represent the IE considering all the electric field components and only the in-plane components, respectively. The grey (yellow) area indicates the $z-$positions where Si particles (waveguide) is present. The TM_0 and TM_1 mode in Fig. 2.7 (a) and (c) have a significant enhancement of the E_z component, as expected for TM modes where the magnetic component is oriented along the $x-$axis. The IE for the TM_0 is remarkably high and can be attributed to the high Q-factor of this resonance. In contrast, in the TE_0-SLR and TE_1 modes of Fig. 2.7 (b) and (d) the IE shows a larger contribution of in-plane electric fields, as expected from the electric dipole excited in the nanoparticles. Compared with the IE of the MD-SLR in Fig. 2.4 (a), we note that the IE in Fig. 2.7 (a) reaches a maximum inside the waveguide, in agreement with our description of the resonance as a TM_0 mode. First order modes present two maxima, which can be seen for the TM_1 and TE_1 in Figs. 2.7 (c) and (d). Only the TE_0-SLR mode in in Fig. 2.7 (b) shows a different IE profile as a function of z. Due to the perturbation introduced by the particles, the fields are only enhanced in the array plane, which leads to an ED-SLR-like IE (see Fig. 2.4 (b)).

The application of QGMs for light-matter interaction calls for more precaution compared with the SLRs. In addition to the different orientation of the field components, we have to consider the spatial dependence of the IE. The fields for the TE and TM have maxima and minima inside the waveguide. Only materials that are spatially overlapping the regions with high IE will experience an increase in excitation rate and, by Lorentz reciprocity, strong emission in the normal direction. Materials positioned at $z = 200$ nm will be effectively quenched in the TE1 mode. This effect was measured for metallic array-waveguides, where it was shown that the photoluminescence enhancement (PLE) changed for emitters situated in different positions within the waveguide. [121]

2.5   Conclusion

We have investigated numerically the diffraction enhanced radiative coupling of Mie resonances in arrays of dielectric nanoparticles. In particular, we have investigated hexagonal arrays of Si nanopilars with large scattering cross sections. We differentiate two systems

depending on the media surrounding the nanoparticles: On one hand, the array supports surface lattice resonances arising from the enhanced radiative coupling of Si nanoparticles if the array is homogeneously surrounded by a dielectric. On the other hand, when the array is embedded in a waveguide it supports quasi-guided modes. Common to these resonances is the significant line narrowing due to the reduction of radiation losses. We also determine the spatial dependence of the electric field enhancement in these systems, finding remarkable differences between SLRs and QGMs. A correct and detailed description of these field enhancements is of utmost importance for the design and optimization of applications relying on high local fields over large areas, such as light emission, lasing, sensing or for photovoltaics.

2.6 Methods

The optical properties of the individual nanoparticles and the periodic structures are simulated using a commercial FDTD software (Lumerical). The simulations of the scattering and absorption efficiencies were done using a total-field scattered-field (TFSF) source with a broadband (400-700 nm) beam incident along the longitudinal axis of the silicon cylinder, which is defined as the $z-$axis. The TFSF source divides the simulation region in two concentric volumes, one central around the particle with the total fields, and another external were only the scattered fields propagate. Power transmission monitors are positioned around and inside the TFSF source to calculate the absorption and scattering cross-sections, respectively. The efficiency is then calculated dividing the former quantities by the geometrical cross-section, i.e. the area of the cylinder perpendicular to the propagation vector k of the incident field. Perfectly matched layer (PML) boundaries are implemented for every direction. Non-uniform meshes are used for the simulations, and a 1 nm refinement mesh around the particle when monitoring the near-field intensities.

The simulations of the arrays were performed using periodic boundary conditions in the $x-$ and $y-$directions, and PML boundaries in the $z-$axis. FDTD only deals with Cartesian grids and for a hexagonal array the unit cell is non-primitive. The illumination consists of a broadband (400-700 nm) beam, approximated by a plane wave, which is incident normal to the array plane (the $xy-$plane) from the substrate. Non-uniform meshes are used, and a 3 nm refinement mesh is used in the array plane, extending over a length equal to the height of the nanoparticle. Due to the very low absorption of silicon between 600-700 nm the lattice resonances are long-lived. Therefore we used long simulation times (5000 fs), specially for the QGMs (7000 fs) with auto shutoff levels of 10^{-6} and even 10^{-7}. This ensures the convergence of the simulations. To extract the transmission and the fields, several monitors are placed in the $xy-$plane at different z positions.

To model the optical constants of Si, Lumerical uses a multi-coefficient model with a polynomial fit of the real and imaginary components of the complex dielectric function in a specific wavelength range that is consistent with the Kramers-Kronig relations.

INVERSE DESIGNED PLASMONIC METASURFACE WITH *ppb* OPTICAL HYDROGEN DETECTION

Plasmonic sensors rely on optical resonances in metal nanoparticles and are typically limited by their broad spectral features. This constraint is particularly taxing for optical H_2 sensors, in which hydrogen is absorbed inside optically-lossy Pd nanoparticles and for which state-of-the-art detection limits are only at the low parts-per-million (ppm) range. Here, we overcome this limitation by inversely designing a plasmonic metasurface based on a periodic array of Pd nanoparticles. Guided by a particle swarm optimization algorithm, we numerically identify and experimentally demonstrate a sensor with an optimal balance between a narrow spectral linewidth and a large field enhancement inside the nanoparticles, enabling a measured hydrogen detection limit of 250 parts-per-billion (ppb). Our work significantly improves current plasmonic hydrogen sensor capabilities and, in a broader context, highlights the power of inverse design of plasmonic metasurfaces for ultrasensitive (gas) detection.

3.1 Introduction

Resonant optical sensors typically rely on wavelength shifts ($\Delta\lambda$) of their spectral features, such as peaks in transmission [124, 125] and reflection [126, 127], induced by analytes. To allow an accurate determination of the peak position and its quantitative dependence on the analyte concentration, one requires sensors with high quality factors (Q-factors), [128, 129] defined as the ratios of their resonance frequency by the corresponding linewidth. Since Q-factors are inversely related to the linewidth, which represents the losses of the resonant system, numerous strategies have been proposed to reduce these losses, and therefore sharpen the resonances and decrease the readout noise of optical sensors. [128, 130] These approaches include the use of low-loss materials [131, 132] and the tailoring of the resonator geometry as in nanoparticles-on-mirror, [133] whispering-gallery-mode microcavities, [134] and periodic metal nanoparticle arrays. [41, 135] In particular, periodic nanoparticle arrays achieve high Q-factors by two processes: First, they reduce the radiative losses of individual nanoparticles by destructive interference of the coherently scattered radiation by the nanoparticles in the array. Second, they redistribute the electromagnetic field into the surroundings, thus outside the individual metallic nanoparticles where losses originate. [41, 132, 136–138] This last condition benefits sensors probing phenomena occurring outside the metal nanoparticles, such as changes in the refractive index of the surrounding medium. [139] On the other hand, the removal of the field from the metallic nanoparticles is unfavorable for other classes of plasmonic sensors that probe changes inside the metal; the so-called direct plasmonic sensors.

   Emerging examples of direct plasmonic sensors are plasmonic hydrogen sensors based on palladium (Pd) nanoparticles and their alloys. [125, 140, 141] These devices feature spark-free and room-temperature operation, efficient remote readout with small footprints, subsecond response time with excellent resistance to cross-contaminating and deactivating gases, and long-term stability. [125, 142–144] Mechanistically, these sensors rely on the barrierless dissociation of H_2 molecules at the surface of Pd nanoparticles and the subsequent intercalation of H atoms into the metal lattice. The corresponding change in dielectric function between pure Pd and Pd hydride leads to shifts in the localized surface plasmon resonance (LSPR) spectra of Pd nanoparticles, which are linearly proportional to the hydrogen concentration inside the particles. [141, 145] Unfortunately, due to the lossy nature of palladium, the LSPR of Pd nanoparticles is broad, [146, 147] with full-widths at half maximum (FWHMs) typically >300 nm for nanostructures with plasmonic spectra at visible or near infrared frequencies. Consequently, these broad peaks introduce inaccuracies in the determination of the sensing readout peak position, λ_{peak}, [140] leading to higher signal noise, σ, and thus higher limits of detection (LoD), defined as the lowest analyte concentration measurable with a signal larger than 3σ. [130, 148] In fact, the detection limit still remains a significant challenge for plasmonic (and optical) sensors, with the state-of-the-art only at single-digit *ppm*; a comparably inferior performance than electrical sensors where *ppb* detection limit has been reported in Refs. [149–153]. While *ppm* hydrogen sensitivity is appropriate for some applications, an ultralow detection limit, coupled with the abovementioned advantages of plasmonic sensing, is crucial for various application requiring local and early detection, such as hydrogen embrittlement in

engineering structural materials, [154] and intragastric hydrogen production in bacterial infections. [155, 156]

Here, we overcome the sensitivity bottleneck of optical sensors by designing and experimentally demonstrating a sensor capable of detecting hydrogen gas down to the *ppb* level. Our sensing platform is based upon 2D periodic arrays of palladium nanoparticles that support collective surface lattice resonances (SLRs). These resonances emerge *via* the hybridization of the LSPRs of the individual nanoparticles and the constructive in-plane diffraction orders of the incoming light, known as Rayleigh anomalies (RAs). [41, 157, 158] Since RAs emerge from interference effects outside the metal nanoparticles, they are characterized by narrow spectral features [159] that are therefore inherited by the SLRs. We employ inverse nanophotonic design–an algorithmic technique to find optical structures with set functional targets, [4] to find sensor array configurations with the highest figure-of-merit (FoM), defined as the ratio between the SLR wavelength shift, $\Delta\lambda_{peak}$, and its FWHM. Critically, we find that the maximum FoM emerging from our evolutionary algorithm is not achieved by the array with the narrowest resonance, but rather by the array with an optimal balance between a narrow SLR and sufficiently large field enhancements inside the nanoparticles. This generic approach, which can benefit any direct plasmonic sensing platform, guides us to identify and experimentally demonstrate a sensor nanoarchitecture with a discernible signal down to 250 *ppb*; the lowest detection limit reported for an optical hydrogen sensor.

3.2 SLR in Pd Nanoparticle Arrays

Despite their sensing potential, plasmonic SLRs have so far only been extensively studied on prototypical plasmonic metals, such as Au and Ag, with sensing applications limited to refractive index changes outside or at the surface of the metal. [41, 79, 130, 160, 161] The use of SLRs for direct plasmonic sensing of phenomena occurring inside the metals requires the utilization of active plasmonic metals such as Y [162], Mg [163] and Pd [147]. Hence, as a crucial step towards our optimized plasmonic sensor, we first demonstrate the existence of SLRs in periodically-arranged Pd nanoparticles and characterize their optical spectra and field distributions. To this end, we fabricated an extensive set of square arrays of 45 nm high Pd nanodisks with varying diameters (d = 70–180 nm, steps of 20/30 nm) and pitch distances (a = 300–600 nm, steps of 50 nm) on fused silica (n_{sub} = 1.46). To allow efficient radiative coupling between the nanodisks by the in-plane diffraction orders, an index-matching medium is essential. [158] We thus coated the arrays with a 200 nm thick poly(methylmethacrylate) (PMMA) film (n_{PMMA} = 1.48). Besides having a suitable refractive index, PMMA is also serendipitously beneficial for Pd hydrogen sensors because it accelerates sorption kinetics by lowering the H_2 absorption energy into the Pd lattice and rebuffs other interfering and deactivating gases, such as O_2, CO, NO_2 and volatile hydrocarbons. [125, 164]

Figure 3.1 shows the experimental extinction spectra of 42 Pd nanodisk square arrays alongside finite-difference time-domain (FDTD) calculations that accurately reproduce all spectral features in the measured data. In particular, we observe extinction spectra with

one, two, or three peaks, depending on the nanodisk diameter and array pitch. The Figure also includes the calculated extinction spectra of the corresponding single-particles, highlighting how arranging the nanodisks in a periodic array results in distinct optical properties compared to their isolated counterparts. Particularly, as the pitch of the array, a, increases, the "main" peaks (as referenced to the array with a = 300 nm) universally redshift and narrow as shown in Figs. 3.2 and 3.3. For example, for the d = 180 nm sample, its FWHM reduces by one order of magnitude from 650 to 65 nm. Furthermore, we observe the appearance of additional redshifting peak(s) at lower wavelength(s) when a reaches 350 and 500 nm. Last, scrutinizing closely these different peaks as a function of diameter reveals contrasting behaviors. While "main" peaks redshift as d increases, the peaks at lower wavelengths are relatively immobile in Fig. 3.2. This observation hints that the "main" peaks are SLRs that are dominated by contributions from the LSPR, and that the peaks at lower wavelengths are dominated by RAs, since their position depends solely on the particle-to-particle distance and not on the nanodisk diameter.
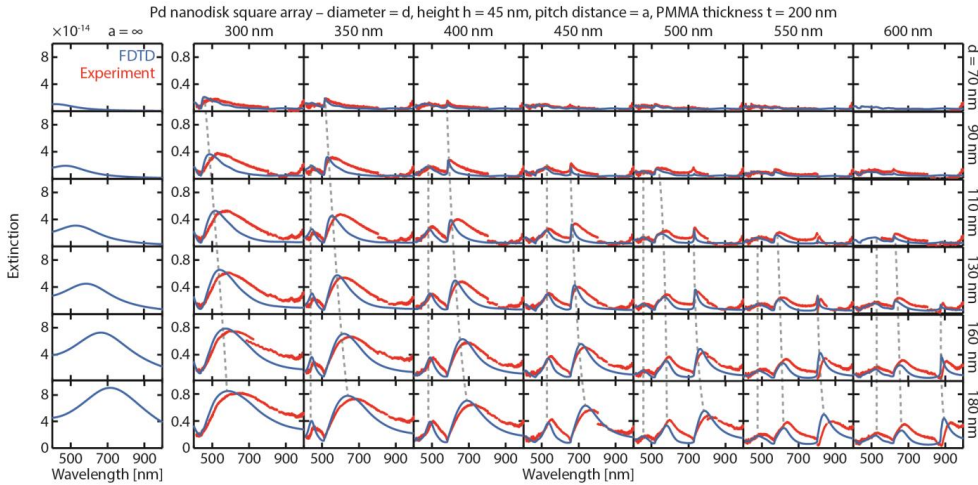
Figure 3.1: Optical extinction spectra of Pd nanoparticles in a periodic array. A collage of experimental (red) and simulated (blue) extinction spectra at normal-incidence from Pd nanodisk square arrays of fixed height, h, of 45 nm and PMMA layer thickness, t_{PMMA}, of 200 nm. The pitch of the array, a, increases from left to right from 300 nm to 600 nm. The nanodisk diameter increases from top to bottom from 70 nm to 180 nm. For comparison, the leftmost panels plot the extinction cross-sections (in m^2) of the corresponding isolated single particles ($a = \infty$). Arranging the nanodisks in arrays results in distinct optical spectra compared to their isolated single particle counterparts. The spectra comprise peaks originating from hybrid RA-LSPR modes – the SLR, see main text for details. Dashed lines are a guide to the eye to the position of corresponding extinction peaks as function of particle diameter.

To further characterize the nature of the extinction peaks, we mapped the field distribution and optical dispersion relation of the array with a = 550 nm and d = 180 nm, which pronouncedly features three extinction peaks in Fig. 3.4 a). Fig. 3.4 b) depicts the
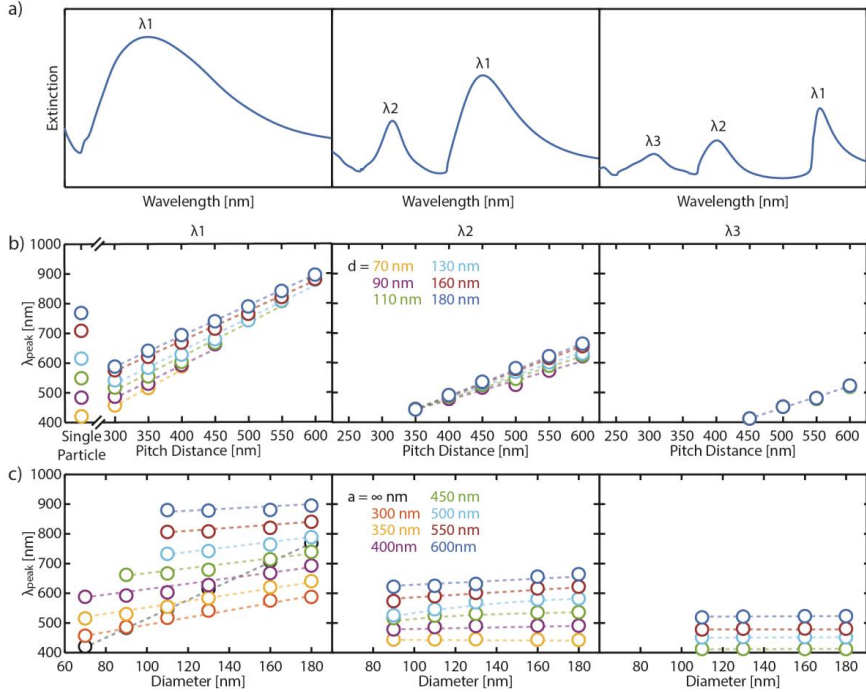
Figure 3.2: (a) Excerpt of simulated extinction spectra of Pd square arrays taken from Fig. 3.1 with different numbers of "peaks" (left: a = 300 nm, middle: a = 450 nm, right: a = 450 nm, all with similar d = 180 nm, h = 45 nm and t_{PMMA} = 200 nm). In each case, λ_1 is consistently assigned to the peak at the longest wavelength, followed by λ_2 and λ_3 (the shortest wavelength). (b) Peak position of λ_1 (left), λ_2 (middle) and λ_3 (right) as a function of array pitch distance (h = 45 nm, t_{PMMA} = 200 nm). Clear dependence of the peak position on the pitch distance in all peaks is observed. (c) Peak position of λ_1 (left), λ_2 (middle) and λ_3 (right) as a function of nanodisk diameter. In contrast to (b), here only λ_1 has dependency on the diameter, whereas λ_2 and λ_3 are rather constant. This behavior corroborates the dominating contribution of the LSPR in λ_1, and of the RA in λ_2 and λ_3, respectively.

FDTD-calculated field distribution map of the array at three different y-polarized excitation wavelengths corresponding to each of the peak wavelengths ($\lambda_1 - \lambda_3$). At the two shorter wavelengths (λ_1 and λ_2), complex field distributions are found, with maxima lying in-between the nanodisks. These features suggest a strong contribution from the RA to the resonance, consistent with the discussion above. The excitation at the longest wavelength (λ_3) gives rise to field maxima in the vicinity of the nanodisks, suggesting a strong contribution of the LSPR to the resonance. [165] Given such field distribution, these relatively localized but narrow peaks will emerge as the sensing peaks for direct plasmonic sensing of hydrogen in our Pd nanodisk arrays.

After confirming the physical origin of the multiple peaks of our array, we carried out an angle dispersion extinction measurement and plot it alongside data from FDTD sim-
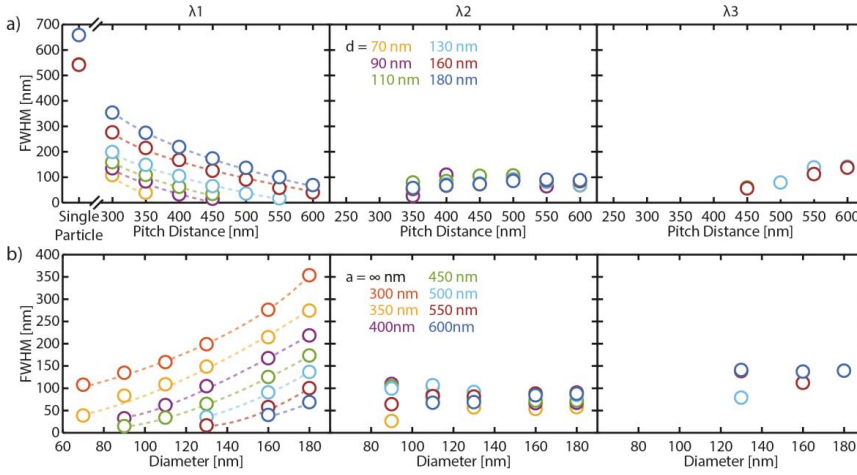
Figure 3.3: (a) FWHM of λ_1 (left), λ_2 (middle) and λ_3 (right) as a function of array pitch distance ($h = 45$ nm, $t_{PMMA} = 200$ nm). Clear dependence of the FWHM on pitch distance in λ_1 is observed, while λ_1 and λ_3 exhibit weak dependency. (b) FWHM of λ_1 (left), λ_2 (middle) and λ_3 (right) as a function of nanodisk diameter. Similar to the case in (a), only λ_1 has dependency on the diameter, whereas λ_2 and λ_3 are rather constant. This behavior, along with the dependency of the peak position shown in Fig. 3.2, corroborates the dominating contribution of the LSPR in λ_1, and of the RA in λ_2 and λ_3, respectively.

ulations (see Fig. 3.4 c)). From the data we can determine the different RA orders that give rise to the optical properties of the array. At shorter wavelengths, the higher ($\pm 1, \pm 1$) modes influence the behavior of the spectra, while at longer wavelengths the ($\pm 1, 0$) and ($0, \pm 1$) modes do. It is these lower order modes that at certain illumination angles overlap with the LSPR deduced from the single-particle extinction peak. The coupling of the LSPR to the diffraction orders results in the narrowing of the resonance, while, as we show later below, maintaining its direct plasmonic sensing properties when exposed to H_2 gas.

3.3 PSO of the Sensitivity of Hydrogen Sensor

Having established the ability to efficiently engineer the FWHM via SLRs in Pd arrays, we move on to design our hydrogen sensor with the aid of FDTD calculation coupled to an inverse design optimization algorithm. As an optimization parameter for the performance of our sensor we use a FoM defined as (Fig. 3.5 a))

$$FoM = \frac{\lambda_{peak,PdH_x} - \lambda_{peak,Pd}}{FWHM_{Pd}}.$$ (3.1)

Our optimization aims at developing sensors capable of detecting H_2 at sub-*ppm* concentrations. At these concentrations and at room temperature, the Pd-H system will be in the so-called α-phase, characterized by hydrogen concentrations in the metal typically lower

Figure 3.4: Field distribution and optical dispersion relation of Pd nanoparticles arranged in a periodic array. (a) Extinction spectra of a array sample with $d = 180$ nm, $h = 45$ nm, $a = 550$ nm and $t_{PMMA} = 200$ nm. (b) 2D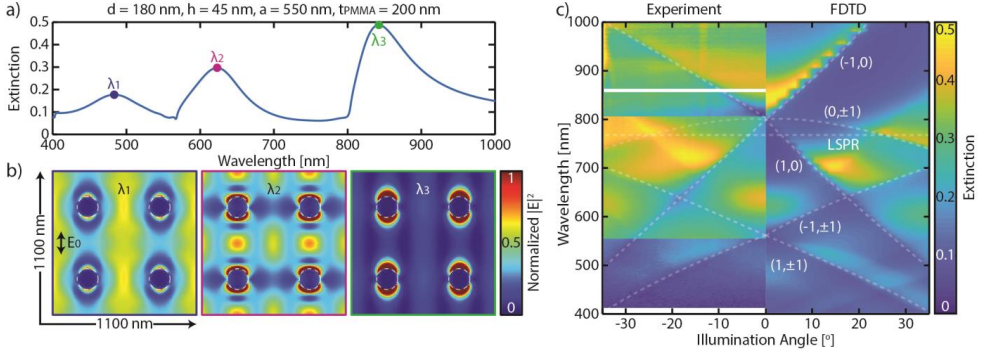 maps of the normalized total field amplitude $|E|^2$ of the array at different excitation wavelengths, as marked in panel (a) at the mid-height of the nanoparticles. Excitation at wavelengths λ_1 and λ_2 generate field maxima far away from the nanodisks – a prominent characteristic in a RA mode. In contrast, excitation at λ_3 features field maxima surrounding the nanodisks. Dashed lines outline the nanodisks themselves. (c) Experimental and simulated wavelength-resolved optical dispersion represented as the extinction spectra of the array for different angles of incidence. The dashed lines indicate the different RA orders of the array. The LSPR wavelength of the corresponding single-particle counterpart is also plotted which crosses two lower RA orders.

than ~ 1 at.%. To best model the optical properties of the palladium hydride phase, we therefore use the composition PdH$_{0.12}$, corresponding to the lowest PdH$_x$ composition for which an accurate dielectric function is available in the literature. [145] From Eq. (3.1), it is apparent that the highest FoM is obtained by finding an array configuration where the contributions from the LSPR (maximizing $\Delta\lambda_{peak}$ upon hydrogenation) and RA (narrowing FWHM) in their hybridized modes are optimized.

Typical plasmonic (hydrogen) sensing setups measure transmission or reflection spectra of the nanofabricated samples within the visible and near-infrared range (400–1000 nm). To have sensors with resonances within this range, we thus limit our array parameter searching space to $d = 100$–300 nm, $h = 20$–100 nm and $a = 300$–500 nm (Fig. 3.5 b)). For the PMMA layer thickness, t_{PMMA}, we limit the range to 100–300 nm. The lower limit of 100 nm is chosen to ensure robust PMMA deposition when translating the parameters into a real sensor and also to provide sufficient refractive index medium, while the upper limit of 300 nm is to avoid significantly slowing the H$_2$ diffusion kinetics introduced by a thicker layer. [166]

To efficiently pinpoint the structural parameter combination with the highest FoM within such four-dimensional searching space, we adopt a particle swarm optimization (PSO) algorithm [167] combined with our FDTD calculations (Fig. 3.5 b)). This computational technique comprises populations that together asses the parameter space, and subsequently influence each other to move within this space to maximize the set goal (fitness parameter) that, in our case, is to maximize the FoM. We utilize 10 populations
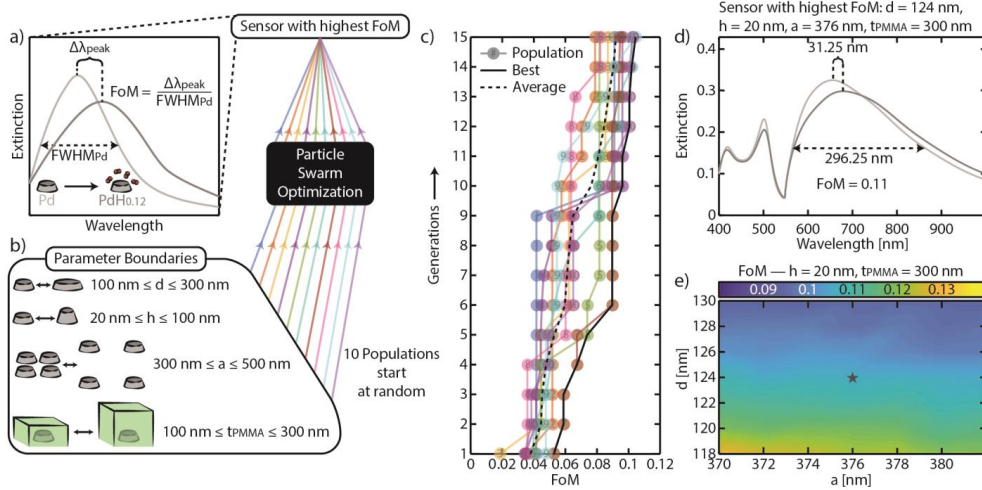
Figure 3.5: Finding the sensor parameters with the highest FoM through particle swarm optimization. (a) Schematic of the working principle and the associated figure of merit of our plasmonic sensor. (b) Sketches of the four parameters defining the architecture of the Pd nanodisk array and their range used for the particle swarm optimization (PSO) algorithm. In this four-dimensional searching space, 10 populations are generated at random and let evolve iteratively through the PSO algorithm to find sensor with the highest FoM, as defined in (a). (c) Evolution of the FoM for each of the 10 populations through 15 iterative generations. Clearly, in each generation, each population finds structures with higher FoM. At the end, one of the populations reaches the highest FoM of 0.11. (d) Extinction spectra of the best sensor (d = 124 nm, h = 20 nm, a = 376 nm, t_{PMMA} = 300 nm) calculated for Pd (light gray) and PdH$_{0.12}$ (dark grey) nanodisk arrays. (e) Calculated FoM of nanodisk arrays with particle diameters d and array pitches a in close proximity to the ones determined for the best sensor (star symbol). The FoM exhibits 10% variance from the best sensor, which indicates that a rather constant FoM can be achieved during the fabrication of the sensor.

that start with a random set of parameter values and assess its corresponding FoM. In the following generations, each population moves to other parameter values that result in a higher FoM (Fig. 3.5 c)). Running this process for 15 generations, we move from an average FoM of 0.03 to 0.09, with single-best populations reaching 0.11. The corresponding best sensor architecture is d = 124 nm, h = 20 nm, a = 376 nm and t_{PMMA} = 300 nm (Fig. 3.5 d)), with $\Delta\lambda_{peak}$ and FWHM of 32 and 296 nm, respectively. Looking at the best sensor extinction spectrum (Fig. 3.5 d)), it is interesting to note that only the LSPR-dominated peak responds to hydrogen, whereas the other peaks have lower LSPR contributions and are therefore less sensitive to changes in the refractive index of the nanodisks, as Fig. 3.6 where the angle dispersion extinction and field distribution of the optimized sensor array are shown. This finding further corroborates our interpretation of the origin of the SLR peaks above. Finally, to appreciate the role of SLR excitation in obtaining sensors with high FoM, we also calculate the optical spectra of the best sensors single-particle counterpart (i.e., similar nanodisk parameters but not in array). As shown in Fig. 3.7, the
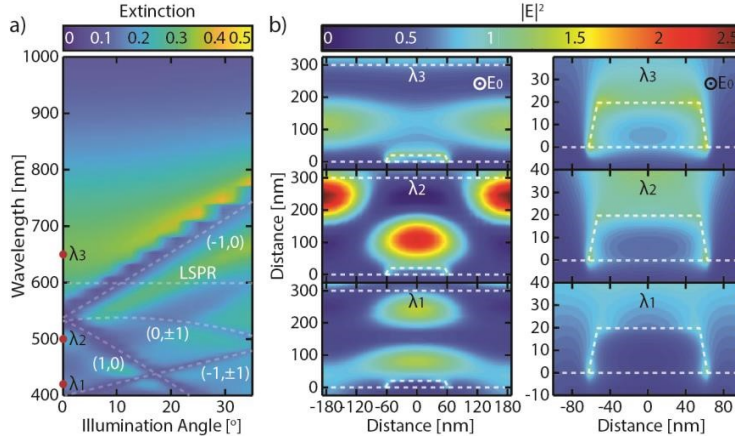
Figure 3.6: (a) Simulated wavelength-resolved angle dispersion extinction spectra of the optimized sensor array, showing the different RA orders (dashed lines) and the LSPR position of the corresponding single-particle counterpart. (b) Field distribution surrounding the nanoparticle (left) and at the close vicinity and inside of the nanoparticle (right) at three different excitation wavelengths corresponding to the extinction peaks (λ_1-λ_3). From the maps it is clear that relative field amplitude inside the nanoparticle excited at λ_1 and λ_2 are lower than the one at λ_3. This again corroborates the nature of the peak, in which λ_3 is dominated by the LSPR and thus is sensitive to the change from Pd to Pd hydride. Dashed lines outline the interfaces between glass/nanodisks/PMMA/air.

isolated nanodisk features comparable $\Delta\lambda_{peak}$, but suffers from an expansive FWHM of 498 nm, which drops its FoM to 0.07.

We also numerically assess the FoM for array parameters in close proximity to the ones of the best sensor architecture. In particular, we vary the pitch of the array, a, and the diameter of the nanodisks, d, within ±6 nm, as these are the parameters that are prone to largest uncertainties in real sample fabrication via electron-beam nanolithography (see Sec. 2.6). As shown in Fig. 3.5 e), the FoM variation within the studied range is relatively small (0.09–0.13, 10% from 0.11), which guarantees us to obtain the expected sensitivity when translating the best sensor parameters into a real sample. Furthermore, it is clear that there are actually a and d combinations that result in slightly higher FoM, which could be identified if the PSO generation iteration would be expanded beyond 15 generations. However, there exists a complex relationship between small structural changes in our arrays and peak positions and linewidths in the corresponding extinction spectra. Given the relatively simple definition of our optimization parameter, FoM, extending our algorithm routine to more than ~15 generations typically led to coalescence of peaks and thus spuriously high FoMs originated from inaccurate assignment of peak positions. While beyond the scope of the present work, these issues can be mitigated by a more rigorous definition of the FoM, peak, and the linewidth in the resulting optical spectra, by more stringent boundaries on the structural parameters of the nanodisks, and by using a dielectric function of much smaller hydride concentration relevant to the targeted H_2
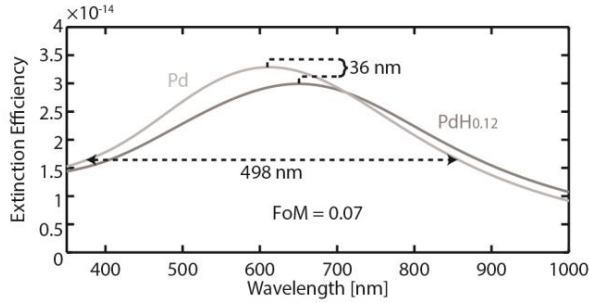
Figure 3.7: Calculated Pd and PdH0.12 extinction spectra of a single Pd nanodisk with same geometrical parameters to the optimized array sensor obtained by PSO (d = 124 nm, h = 20 nm, a = 376 nm, t_{PMMA} = 300 nm). Comparable peak shift as for the array sensor is found upon hydrogenation but with very broad FWHM. This combination results in a FoM of 0.07.

concentration range of the sensor application.

3.4 *ppb* Detection of Optimal Gas Sensor

As the final step of our work and guided by the PSO results, we experimentally realized the optimized sensor design using electron beam lithography (Fig. 3.8 a)-b)) and assessed its detection limit to hydrogen. To this end, we exposed the sensor to pulses of gradually decreasing H_2 concentration in Ar carrier gas (1000 *ppm* to 250 *ppb*, the lowest attainable concentration in our setup) at room temperature and plot its associated $\Delta\lambda_{peak}$, which is obtained through the Lorentzian fit [125]. As depicted in Fig. 3.8 a), the sensor responds positively to different H_2 concentrations, with a signal noise, σ sensor, of 0.01 nm in Fig. 3.9. Due to this small noise, the sensor is able to measure even the lowest 250 *ppb* pulse, making it the first optical hydrogen sensor to achieve sub-*ppm* detection. Recalling LoD as the lowest hydrogen pressure measurable with a signal larger than 3σ, we extrapolate it to be 200 *ppb* (Fig. 3.8 b)). We expect such sensitivity to also hold in air thanks to excellent O_2 sieving by PMMA. [125, 168]

As an important control, we fabricated an array with similar geometry parameters (d = 124 nm, h = 20 nm, and t_{PMMA} = 300 nm), but with the nanodisks dispersed randomly over the substrate rather than in a periodic lattice (Fig. 3.8 c)-d)) and Fig. 3.10). We compared the optical response of this control sensor exposed to H_2 pulses under similar experimental conditions as the periodic array. Consistent with the FDTD simulations (Fig. 3.7), the control sensor exhibits comparable $\Delta\lambda_{peak}$ with respect to the H_2 concentration (Fig. 3.8 c)). However, due to its larger FWHM, its λ_{peak} determination results in a significantly higher noise, σcontrol, of 0.08 nm (Fig. 3.10), which ultimately leads to a LoD of 1.5 *ppm*, nearly an order of magnitude higher than the detection limit of its array sensor counterpart (Fig. 3.8 d)). This comparison accentuates the critical impact of the narrow FWHM, here engineered through the use of optimized SLRs, for resolving $\Delta\lambda_{peak}$ signals at low

concentrations.
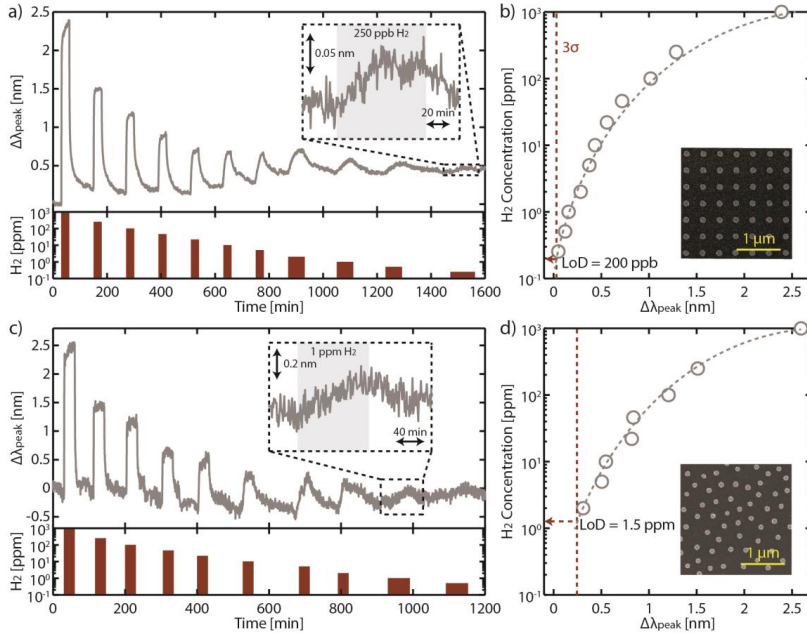
Figure 3.8: Ultralow detection limit with Pd periodic array sensor. (a) $\Delta\lambda_{peak}$ response to stepwise decreasing H$_2$ concentration (1000 to 0.25 *ppm*) in Ar carrier gas at room temperature. Inset: zoomed-in version of the sensor response to 250 *ppb* H$_2$. (b) Measured $\Delta\lambda_{peak}$ as a function of H$_2$ concentration derived from (a). Gray dashed line is a guide to the eye and extrapolates the sensor response to the 3σ value (0.03 nm, red dashed line), indicating a LoD ~200 *ppb* (red dashed arrow). Inset: SEM image of the fabricated sensor. (c) and (d) are the data from a control quasi-random array sensor analogous to (a) and (b). The control sensor responds comparably to the periodic array sensor but suffers from its higher noise. Hence, its LoD is ~8 times higher at 1.5 *ppm*.

3.5 Conclusions

In summary, we have used an inverse nanophotonic design approach to identify and experimentally demonstrate an ultrasensitive plasmonic hydrogen detector based on collective resonances in periodic arrays of palladium nanoparticles. The optimized sensor displays a non-trivial balance between a large optical response upon hydrogenation and narrow spectral features. The measured *ppb* limit of detection is an order of magnitude lower than any previous optical hydrogen sensor and becomes competitive with the more mature electrical sensors. The genericity of our strategy allows it to be combined with other optimization approaches, including the use of more sensitive transduction materials such as PdAu, [125, 141, 169, 170] (eight fold more sensitive than Pd at low H$_2$ concentrations) or PdTa [171] alloys, and advanced data fittings capable of producing lower signal

noise. [172] Furthermore, we have so far only explored a simple and generic figure-of-merit parameter during our optimization, namely the peaks shift divided by the linewidth. Our inverse design approach, however, also permits the optimization of nanoparticle arrays for sensing platforms using different readouts such as single-wavelength mode devices, [173, 174] opening the door to low-cost, ultrasensitive platforms. Beyond hydrogen sensing, our approach can be extended to arrays of surface-functionalized nanoparticles with resonances that are sensitive to the adsorption of specific gasses via refractive index effects or chemical interface damping, [175] with the potential to address a wider range of societal needs, from home safety to urban air pollution monitoring. [176]

3.6 Methods

3.6.1 Sensor Fabrication and Characterization

The samples of Pd periodic array were fabricated from a 4-inch fused silica wafer with electron-beam lithography, thermal evaporation, electron-beam evaporation, wet-chemical etching, reactive-ion etching, lift-off, and dicing. The steps involved included: (i) Using a 4-inch fused silica substrate (Siegert Wafer), a lift-off layer of 80 nm MCC NANO Copolymer EL4 (Microlithography Chemicals Corp.) was first spin coated and baked on a contact hotplate for 5 min at 180°C. Following that, an imaging layer of 70 nm MCC NANO 950k PMMA A2 (Microlithography Chemicals Corp.) was spin coated and baked on a contact hotplate for 5 min at 180°C. (ii) A 20 nm thick Cr layer was deposited with thermal evaporation (Lesker Nano 36) to enable electrical discharge during electron-beam exposure. (iii) The nanodisks were defined in the double resist layer on areas of 10×10 mm^2 with electron-beam lithography (Raith EBPG 5200) by exposing circles of 35 nm radius. Each circle was filled with 19 shots at a beam current of 50 nA and at a base frequency of 5.19 MHz. (iv) The 20 nm Cr discharge layer was removed by immersing the substrate for 60 s in Nickel/Chromium etchant (SunChem), followed by water rinsing and blow drying. (v) The exposed resist was developed for 60 s in MIBK 1:3 IPA solution, dried in N2-stream, and descummed in oxygen plasma for 5 s at 50 W RF-power, 250 mTorr chamber pressure, and 40 sccm gas flow in a BatchTop Reactive Ion Etcher (PlasmTherm). (vi) To form the nanostructures, Pd were deposited through the resist mask with electron-beam evaporation at a deposition rate of 1 Å/s in a PVD 225 system (Lesker), lifted off in acetone for 24 h, rinsed in IPA and blow dried in N2-stream. (vii) Finally, the wafer was diced (DAD3350, Disco) into individual chips of 10×10 mm^2. For the control quasi-random array sample, the fabrication procedures (steps, materials, and tools used) followed exactly the protocol reported in ref.[125] The only difference was the polystyrene beads used, that is, 120 nm sulfate latex, Interfacial Dynamics Corporation, 0.2 wt.% in Milli-Q water (Millipore). The SEM images were collected from glass samples coated with 5 nm Cr layer (Zeiss Supra 60 VP with secondary electron detector, working distance 4 mm, and an electron beam acceleration voltage of 7–15 kV).

3.6.2 Finite-Difference Time-Domain Simulations

We used commercial Lumerical FDTD software to calculate the optical properties of both single and array of Pd nanodisks. We modeled the nanodisks as cylinders with a taper angle (the angle between the base and the side wall) of 65° to be close with the fabricated samples. [177] The permittivity values of Pd and Pd hydride ($PdH_{0.12}$) were taken from the literature. [145] The nanodiks were placed directly on top of a fused silica substrate (n = 1.46). On top of the substrate and embedding the particles, a PMMA layer was added, whose permittivity was obtained from an ellipsometry measurement. [178] Finally, on top of this layer, there was air (n = 1). The simulations of the scattering efficiencies were done using a total-field scattered-field (TFSF) source with a broadband (400–1100 nm) beam incident from air and along the normal direction. The TFSF source divides the simulation region into two concentric volumes: one centered around the particle with the total fields, and another external where only the scattered fields propagate. Power transmission monitors were positioned around the TFSF source to calculate the scattering cross sections. The efficiency was calculated by dividing the former quantities by the geometrical cross section, i.e., the area of the cylinder perpendicular to the propagation vector k of the incident field. Perfectly matched layer (PML) boundaries were implemented in every direction. The simulations of the periodic arrays were performed using periodic boundary conditions in the x- and y-directions, and PML boundaries in the z-direction. The illumination consisted of a broadband (400–1100 nm) beam, approximated by a plane wave, which was incident normal to the array plane (the xy-plane) from air. To extract the transmission, an xy monitor was placed at the substrate side. Another xy monitor was placed at the center of the particles to extract the fields. The polarization of the incident electric field was set along the y-axis. To extract the extinction (i.e. 1 - transmission) dispersion data, several simulations with different incident angles were performed.

3.6.3 Optical Dispersion Measurements

An unpolarized broadband light source was used to illuminate the samples and investigate their optical dispersion. The light was focused onto the sample and collected with a Nikon L Plan 20x/0.45NA and a Nikon S Plan Fluor 40x/0.6NA objectives, respectively. Using a dedicated lens system, the back focal plane of the objective was imaged with an imaging spectrometer connected to a multiplying CCD camera (ProEM: 512B). The back focal plane contained the Fourier transform of the optical field transmitted by the sample upon illumination, i.e. the angular dispersion of the transmitted light. The image on the CCD contained 2D angular information for all the wavelengths illuminating the sample. Closing the slit that controlled the light entering the imaging spectrometer allowed selection of one angular component and its spectral decomposition into the CCD. To get accurate wavelength resolution, a grating of 150 g/mm was used. This allowed ±150 nm range to be imaged for a selected wavelength center. To image the full spectrum of the sample (400–1000 nm) we measured spectra at several wavelength centers (i.e. 470, 620, 770, and 900 nm, respectively). Using a polarizer before the illumination objective allowed us to select between TM and TE polarizations.

3.6.4 Particle Swarm Optimization Calculation

To design the most sensitive hydrogen sensors, the FDTD method associated with the particle swarm optimization (PSO) algorithm was adopted. PSO is a robust population-based stochastic evolutionary computation technique, which is inspired by the natural social behavior and dynamic movements with communications of animal species (called particles) and looking for their requirements in a search space. [167]
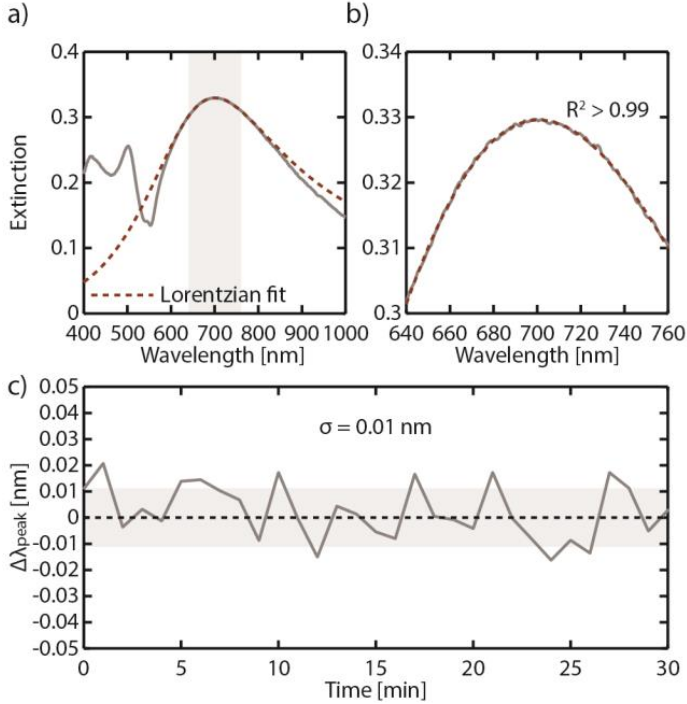
Figure 3.9: (a) Lorentzian function fitting (red dashed line) to the experimental optical spectra to extract λ_{peak}. In our analysis, the fit is only applied within ±60 nm from the peak maximum (grey shaded area, following the method established in Ref. [142]), where the peak is symmetric. (b) Zoomed-in version of (a) within the fit range. Clearly, the Lorentzian represents well the data and thus enables a good fit with $R^2 > 0.99$. (c) Lorentzian-fitted $\Delta\lambda_{peak}$ response of the best sensor (cf. Fig. 3.8 a)) in the first 30 min of operation used to derive the peak-to-peak readout noise, σ, of 0.01 nm. The dashed lines and gray-shaded areas denote the mean of the signal and $\pm\sigma$ from the mean, respectively.

Here PSO was employed to optimize the structural parameters of the plasmonic hydrogen sensor to yield the highest FoM defined by Eq. (3.1). To this end, we chose to use $PdH_{0.12}$ for the calculation of the hydride phase for the following reasons: (i) This is the lowest Pd hydride concentration whose dielectric function is available in the literature. [145] (ii) At this concentration, the Pd hydride is still at the diluted α-phase, with negligible lattice expansion. This condition prevents inaccurate calculation during FDTD

simulation where the expansion of the nanodisk has to be included. [179] (iii) The chosen hydride concentration is also in line with the targeted range of the hydrogen concentration. (iv) Lastly, the accompanied spectral change of the sensor at this hydride concentration was expected to be small enough so that it would be the same SLR peak that was considered, thus avoiding false $\Delta\lambda_{peak}$ determination when calculating the FoM, as we detailed later below.

To begin the optimization, the algorithm was initialized with 10 Pd/PdH$_{0.12}$ nanodisk arrays of random locations of parameters in their own spaces, which then were sent to the Lumerical FDTD platform, where the transmission was numerically evaluated. After that, FDTD sent the computed optical values back to the algorithm where the FoM was calculated, and produced the parameters for the next generation. The full technical description of the PSO used here is provided in Sec.1.7 of chapter 1.

Ideally, PSO should keep iterating until all particles converge to the global optimal solution instead of stopping at the 15th generation as in our present case here. However, we found that a number of populations updated their FoM through very large peak shifts and very broad FWHM that included two SLR different peaks. In this case there are two close SLR peaks in both Pd and PdH$_{0.12}$ arrays at around 530 nm and 650 nm, respectively. In this case, the algorithm wrongly considered the lower wavelength peak for the case of Pd, and the longer wavelength peak for the case of PdH$_{0.12}$, causing a wrong evaluation of $\Delta\lambda_{peak}$. Furthermore, the FWHM was also calculated for two close SLRs. Consequently, in such case, we cannot correctly calculate the FoM since the parameters originated from two different peaks. Because this similar array began to appear in the 16th generation, we stopped the PSO after the 15th generations and confirmed that all the FOM calculated were from single SLR peak.

Targeted H$_2$ Concentration [ppm]	1000 ppm H$_2$ Flow [mL/min]	Ar Flow [mL/min]
1000	1	0
250	5	15
100	2	18
46	1	21
22	1	44
10	1	99
5	0.5	199
2	0.25	125
1	0.1	100
0.75	0.1	133
0.5	0.1	200
0.25	0.05	200

Table 3.1: Set Flow of Hydrogen and Argon Gas to Achieve the Targeted Hydrogen Concentrations.

3.6.5 Hydrogen Sensing Measurements

The sensors' LoD determination was performed in a custom-made reactor chamber (effective volume *ca.* 1.5 mL) equipped with two fused silica viewports (1.33" CF Flange, Accu-Glass) that enabled transmission-mode optical monitoring. The detail of the chamber is reported in ref. [180]. The transmission measurements were carried out through fiber-coupled, unpolarized halogen light source (AvaLight-HAL-S-Mini) and a high-resolution visible range spectrophotometer (Avantes Sensline Avaspec-HS-TEC).
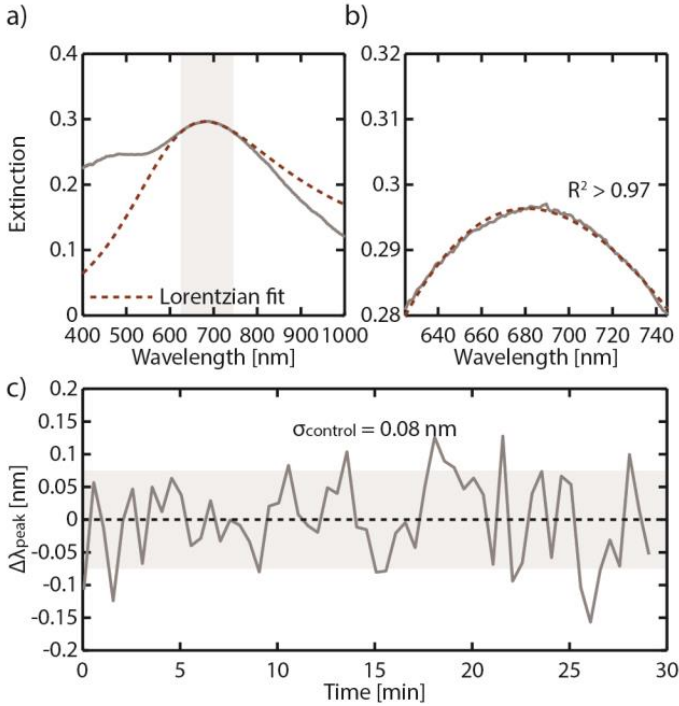
Figure 3.10: (a) Lorentzian function fitting (red dashed line) within ±60 nm from the peak maximum (grey shaded area) to extract λ_{peak}. (b) Zoomed-in version of (a) within the fit range. The Lorentzian represents the data well in the peak-maximum region and thus enables a good fit with $R^2 > 0.97$. (c) Lorentzian-fitted $\Delta\lambda_{peak}$ response of the quasi-random array control sensor (cf. Fig. 3.8 c)). The derived peak-to-peak noise, σ control, is 0.08 nm, much higher than that of the optimized regular array sensor. The dashed lines and gray-shaded areas denote the mean of the signal and $\pm\sigma$ from the mean, respectively.

The H_2 gas concentration was controlled by adjusting the flow rate (v [mL/min]) ratio of 1000 ppm H_2 (diluted in Ar) and 100% Ar using mass flow controllers (MFCs, Bronkhorst El-Flow Select series). Table. 3.1 shows the targeted hydrogen concentrations by setting flow of hydrogen and argon gas.

All experiments were carried out at constant 30°C, regulated via a PID controller (Eurotherm 3216) in a feedback loop manner, where the sample surface temperature

inside the chamber was continuously used as input. As readout, the LSPR peak descriptors (λ_{peak}) were obtained following the method we established earlier. [125] In detail, a Lorentzian fit was applied to the wavelength range at ± 60 nm around the LSPR peak in the measured optical extinction spectra. Despite the asymmetry of the global LSPR peak, a good fit ($R^2 > 0.97$) was obtained, and thus the fit is appropriate to determine the λ_{peak}. Results are displayed in Fig. 3.9 and Fig. 3.10 for the optimized array sensor and quasi-random array control sample as comparison, respectively.

EVOLUTIONARY OPTIMIZATION OF LIGHT-MATTER COUPLING IN OPEN PLASMONIC CAVITIES

Using a Particle Swarm Optimization (PSO) algorithm and Finite-Difference in Time-Domain (FDTD) simulations, we optimize the coupling strength between excitons in poly(3-hexylthiophene-2,5-diyl) (P3HT) and surface lattice resonances (SLRs) in open cavities defined by arrays of aluminum nanoparticles. Strong light-matter coupling and the formation of exciton-polaritons are demonstrated. Nanoparticle arrays with optimal dimensions have been fabricated and measured, validating the predictions by the numerical method. P3HT is a regioregular semiconducting polymer used as a donor material in acceptor-donor blends for organic photovoltaic applications. Our results demonstrate the efficacy of the proposed method for the optimization of light-matter coupling and its potential application for the enhanced performance of optoelectronic devices.

4.1   Introduction

The recent advent of polaritonic devices (optoelectronic devices based on exciton-polaritons (EPs) arising from the strong coupling of excitons in semiconductors and photons in optical cavities) is attracting a significant interest due to the remarkable properties of EP states. The large binding energy, and the associated high transition dipole moments of Frenkel excitons in organic semiconductors, lead to many intriguing phenomena emerging from strong light-matter coupling at room temperature. The hybrid character of organic EPs makes them exhibit photon and exciton properties that result in the modification of intrinsic semiconductor properties, [181–183] such as the enhancement of the exciton diffusion length [184–189], increase of the long-range energy transfer [190–192] or reduction of photobleaching [193, 194]. Enhanced non-linearities in EPs are also responsible for polariton lasing, [195–198] and quantum condensation due to the bosonic character of EPs, [199–203] which can lead to low threshold coherent emission.

Organic photovoltaic (OPV) devices can profit from strong light-matter coupling and EPs. OPV cells are easy to fabricate, lightweight, mechanically flexible and can be partially transparent, which make them very appealing for large-area energy conversion. However, the power conversion efficiency of OPV cells is low and limited by the thickness of the active layer, which is determined by exciton diffusion lengths and carrier recombination losses. [204, 205] Other limiting factors are the charge transfer across the interface separating the donor-acceptor materials and the photo-degradation due to intersystem crossing. [206] The modified energies of EPs, compared to excitons, could be used to reduce the triplet density or enhance reversed intersystem crossing [191, 207–209], modify the excited-state life time [193, 210–212], or enhance exciton and charge transport [184–189, 213–215]. These phenomena could be exploited to solve the problems limiting a more extended utilisation of OPV and the first steps in this direction have been made. [216–218] However, most of the works on strong light-matter coupling are based on closed Fabry-Perot microcavities with the active semiconductor enclosed between two mirrors. [219] Such a closed geometry limits the application of strong light-matter coupling in OPV, where incident light needs to be absorbed as efficiently as possible in the active material.

In this chapter, we investigate the coupling of excitons in regioregular poly(3-hexylthiophene-2,5-diyl) (P3HT) semiconducting polymer with optical modes in resonant cavities formed by square arrays of plasmonic nanodisks made of aluminum (Al). P3HT is an electron donor polymer, widely employed in OPV. Nanoparticle arrays define open optical cavities with optical modes that result from the radiative coupling of localized surface plasmon resonances to diffraction orders in the plane of the array. These optical modes are know as Surface Lattice Resonances (SRLs). [220] SLRs can have remarkably narrow linewidths (high Q-factors) due to low radiation losses and high field enhancements over large volumes [135, 221–223]. When the nanoparticle array is covered by a P3HT layer, SLRs can couple to excitons in the organic semiconductor as evidenced by the formation a lower and upper EP states in the absorption spectrum with an associated Rabi Splitting. [224] We have used a Particle Swarm Optimization (PSO) algorithm to find

the global best sample dimensions for light-matter coupling. [225–228] We run the PSO algorithm together with Finite-Difference in Time-Domain (FDTD) simulations using 30 stochastic populations with randomly chosen sample parameters that evolve during 100 generations. [229] Samples have been fabricated with the optimized dimensions and and the optical extinction dispersion has been measured, confirming the results obtained by the PSO algorithm.

4.2 Excitons in P3HT

The optical properties of P3HT, defined by the refractive index and extinction coefficient, have been retrieved from the ellipsometry measurement, as shown in Fig. 4.1 with dashed curves. To use these values in the FDTD simulations, we have fitted the refractive index n and extinction coefficient κ to a Lorentz oscillator model:

$$n + i\kappa = n_{back} + \frac{A(\omega_0^2 - \omega^2)}{B[(\omega_0^2 - \omega^2)^2 + \omega^2\gamma^2]} + i\frac{A\gamma\omega}{B[(\omega_0^2 - \omega^2)^2 + \omega^2\gamma^2]} \tag{4.1}$$

where $n_{back} = 1.72$, $A = 2.51 \times 10^{-11}$, $B = 1.61 \times 10^{-41}$, $E_0 = \hbar\omega_0 = 2.38\ eV$, $\gamma = 4.48 \times^{14}\ s^{-1}$. The Lorentz fit is given by the solid curves in Fig. 4.1 (a). From this fit we retrieve the main exciton energy of 2.38 eV, corresponding to a wavelength of 521 nm, and the P3HT background refractive index (refractive index far from the exciton energy) of 1.72. Actually there is another weak exciton energy of P3HT is about 2 eV. In order to eliminate some interference, in our study, we ignore it and only focus on the most important resonance.
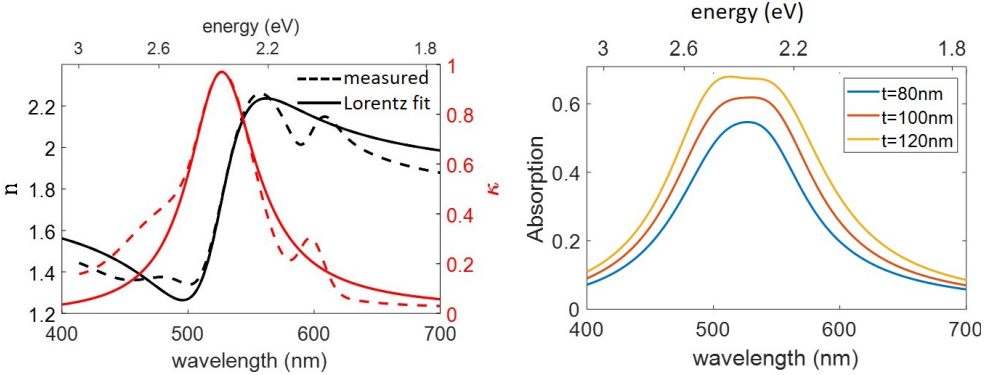
Figure 4.1: (a) Refractive index (n) and extinction coefficient (κ) obtained from ellipsometry measurements (dashed curves) and fitted to a Lorentz oscillator model (solid curves). (b) Absorption spectra of P3HT with a thickness 80 nm, 100 nm and 120 nm, respectively.

The thickness of active layer in OPV device should be large enough for effective photon absorption. The P3HT absorption for a thickness of 80 nm, 100 nm and 120 nm are

displayed in Fig. 4.1 (b). The power conversion efficiency of organic solar cells is usually low because of the short exciton diffusion lengths (<100 nm) and carrier recombination losses. For this reason, we fix the thickness of P3HT to 100 nm for applications in organic solar cells.

4.3 Bare States and Fitness Value

A schematic representation of the investigated system is depicted in the left of Fig. 4.2 (a). This system consists of a square array of aluminum (Al) nanoparticles with a layer of P3HT on top of an eagle glass substrate (refractive index $n = 1.51$). The choice of Al is motivated by the plasmonic response of this metal at short wavelengths in the visible spectrum and its stability. The thickness of the P3HT layer is fixed as 100 nm, comparable to the typical thickness of the active layer in organic solar cells. The Al nanoparticles, with diameter d and height h, are arranged in an infinite periodic square array with a lattice constant a. The nanoparticle array is designed to support SLRs at the P3HT exciton energy for normal incidence, i.e., light with a wavelength close to 500 nm and incident along the normal direction to the surface of the arrays is diffracted in the plane of the array.

Two questions are addressed in this chapter: (i) What is the maximum Rabi splitting that can be achieved by coupling of P3HT excitons and SLRs supported by a square array of Al nanoparticles? and, (ii) which parameters of the array lead to this maximum Rabi splitting? We seek the answers to these questions by using a PSO algorithm and FDTD. PSO algorithms are designed for numerical optimization problems that look for the solution by defining a random population of candidate solutions ("particles") than can move (or evolve) over the search space by changing position and velocity. Each "particle" movement is influenced by its own local best position and the best known positions of the other "particles". Subsequent generations converge to a global best solution. A more detailed description of the PSO method can be found in section 1.7 of chapter 1.

The interaction between excitons in P3HT and SLR cavity can be expressed by a two coupled harmonic oscillator model:

$$\begin{bmatrix} \omega_c - \frac{i\gamma_c}{2} & g \\ g & \omega_p - \frac{i\gamma_p}{2} \end{bmatrix} \begin{pmatrix} \alpha \\ \beta \end{pmatrix} = \omega \begin{pmatrix} \alpha \\ \beta \end{pmatrix} \tag{4.2}$$

where ω_c and ω_p are the energies of the bare SLR and excitons in P3HT, respectively, γ_c and γ_p are the decay rates of these bare states, and g is the coherent coupling strength, which depends on the magnitudes of the transition dipole moment of the excitons $\boldsymbol{\mu}$, the cavity fields $|\boldsymbol{E_0}|$, and their relative orientation, $g = \boldsymbol{\mu} \cdot |\boldsymbol{E_0}| = \boldsymbol{\mu} \cdot \boldsymbol{u_c} \sqrt{\frac{N\hbar\omega_p}{\epsilon_0 V}}$, where $\boldsymbol{u_c}$ is the unit vector indicating the direction of the electric field of the cavity mode, N is the number of excitons, ϵ_0 is the vacuum permittivity, and V is the cavity mode volume. Thus, the energies of the lower polariton band (LPB) and the upper polariton band (UPB) for zero detuning of the bare states ($\omega_c = \omega_p = \omega_0$) are

$$\omega_{\pm} = \omega_0 - \frac{i(\gamma_c + \gamma_p)}{4} \pm \frac{1}{2}\sqrt{(2g)^2 - \frac{(\gamma_c - \gamma_p)^2}{4}}. \tag{4.3}$$
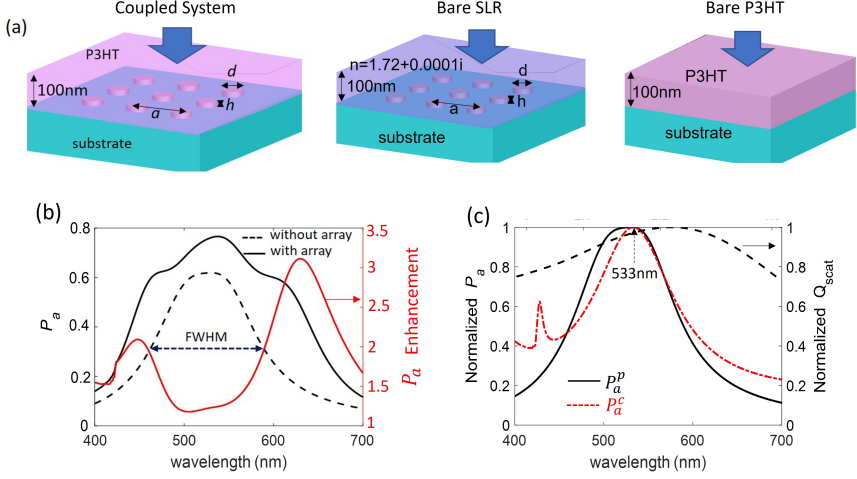
Figure 4.2: (a) Schematic representation of the investigated samples. left: a square array with lattice constant, a, formed by Al nanoparticles with height h and diameter d on top of a glass substrate and embedded in a P3HT layer with a thickness $t = 100$ nm. Systems supporting the bare states. middle: Al nanoparticle array on glass with a layer of 100 nm of a material with a refractive index $n = 1.72 + 0.0001i$, and right: P3HT layer with a thickness of 100 nm on top of glass. (b) Normalized power absorption of P3HT for coupled system (black curve) and absorption enhancement (red curve) compared to the bare state of P3HT (black-dashed curve). (c) Normalized P_a^p of the 100 nm thick P3HT layer on a glass substrate (black curve); normalized P_a^c of a 100 nm thick layer with refractive index $n = 1.72 + 0.0001i$ on top of an Al nanoparticle array with a=280 nm, d=130 nm, and h=49 nm (red curve); and normalized scattering efficiency Q_{scat} for an Al nanodisk with h=49 nm and d=130 nm (red-dashed curve).

The value of Rabi splitting is given as $\omega_+ - \omega_-$ by

$$\Omega_R = \sqrt{(2g)^2 - \frac{(\gamma_c - \gamma_p)^2}{4}}, \tag{4.4}$$

with a maximum value when $\gamma_c = \gamma_p$. Strong coupling and the formation of exciton polaritons happens when

$$4g^2 > \frac{(\gamma_c - \gamma_p)^2}{4}. \tag{4.5}$$

However, the coupling strength needs to be larger than the mean of the losses of the bare states for making visible the splitting between the LPB and UPB. Therefore, a better criterium for strong coupling is usually defined as

$$4g^2 > \frac{\gamma_c^2 + \gamma_p^2}{2}. \tag{4.6}$$

The properties of SLRs in the Al nanoparticle arrays are controlled by the size of the nanoparticles and the lattice constant. We tune the geometrical parameters, including the

height h, diameter d of nanodisk, and the lattice constant of the square array a, independently, to find the lattice with a SLR absorption that matches spectrally and spatially the absorption spectrum and the location of P3HT layer. The fitness value that we maximize with the PSO algorithm is defined by

$$F = \frac{2P_{abs}}{|\gamma_c - \gamma_p|}, \tag{4.7}$$

where P_{abs} is given below and corresponds to the overlap integral of the absorption spectra of the bare (uncoupled cavity and exciton) states leading to the coupled system, and γ_c and γ_p are the decay rates of these bare states. The fitness value is inversely proportional to the modulus of the difference between the loss rates of the bare states, which is justified by the fact that in the above coupled oscillator model, the Rabi splitting is maximum when $\gamma_c = \gamma_p$.

The coupled system results from the hybridization of the bare states, schematically represented in right side of Fig. 4.2 (a), and corresponding to (i) SLRs in an empty cavity, i.e, a nanoparticle array on glass with a 100 nm thick layer of a material with a background refractive index of $n = 1.72 + 0.0001i$ on top, similar to the refractive index of P3HT at energies far from the exciton energy, and (ii) excitons in a P3HT layer with a thickness of 100 nm on top of glass. These bare states have been simulated using FDTD by determining the absorbed power spectrum in the volume occupied by the layers and given by $P_a^c(\omega)$ and $P_a^p(\omega)$ for the bare cavity and bare P3HT layer, respectively. The normalized absorbed power spectra are displayed in Fig. 4.2 (c), where we use $h = 49$ nm, $d = 130$ nm and $a = 280$ nm. As shown in the next section, these values correspond to the array with the largest coupling strength. The absorbed powers are defined by integrating over the volume occupied by the layers in a unit cell of the array: $P_a^{c,p}(x,y,z,\omega) = (1/2)\epsilon_0\omega|E_{c,p}(x,y,z,\omega)|^2\epsilon''_{c,p}(\omega)$, where $E_{c,p}(x,y,z,\omega)$ is the electric field at frequency ω and position (x,y,z) in the layer on top of the array and in P3HT, and $\epsilon''_{c,p}(\omega)$ is the imaginary component of the dielectric function of the layers. Note that we allow for a sufficiently small imaginary component of the refractive index in the layer on top of the Al nanoparticle array to calculate an absorbed optical power in this layer without introducing a significant change to the SLR mode profile. The absorbed power peak at 533 nm corresponds to the SLR emerging from the (1,0) and (-1,0) diffraction orders, while the narrower peak around 428 nm is due to the (0,±1) diffraction orders. P_{abs} in Eq. (4.7) is given by

$$P_{abs} = \frac{\int P_a^c(\omega) P_a^p(\omega) d\omega}{V}, \tag{4.8}$$

where V is the volume of the polymer layer in a unit cell of the array. The fitness value given by Eq. (4.7) is thus proportional to the overlap integral of the absorbed power of the bare systems calculated in the volume occupied by the polymer. Correspondingly, we consider the regions in the sample where the SLR mode overlaps with the excitons in P3HT. The choice of this fitness value ensures that both the absorption of the bare states and their overlap is maximum, which should also lead to a maximum coupling strength and Rabi splitting. As it is apparent in Fig. 4.2 (b), the power absorption of P3HT in coupled

system shows two additional absorption peaks at lower and high energies than the exciton peak. Furthermore, the absorption of P3HT is greatly enhanced by strong coupling, which further contributes to the formation of LP and UP peaks. The maximum Rabi splitting can be expressed as the energy difference between UP and LP.

We also show with the dashed curve in Fig. 4.2 (c) the normalized scattering efficiency of a single Al nanoparticle with the same dimensions as the nanoparticles in the array to illustrate the significant narrowing of the SLR as a results of the collective response of the array. The tuneability of the line-width of the SLR, which is controlled by the localized plasmonic resonances in the individual nanoparticles and the diffraction orders in the plane of the array, turns out to be critical to achieve the largest possible coupling strength and Rabi splitting. [40, 41, 230]
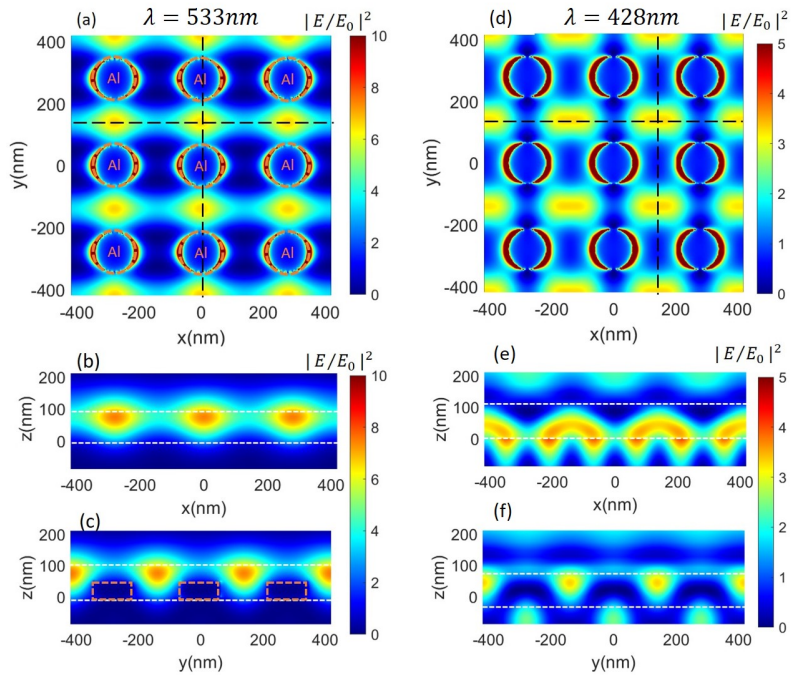
Figure 4.3: Electric field intensity at $\lambda = 533$ nm (a) in the $x - y$ plane on top of the nanoparticles, (b) in the $z - x$ plane indicated in (a) with the horizontal black-dashed line, and (c) in the $z - y$ plane indicated in (a) with the vertical black-dashed line. The boundaries of the Al nanoparticles are indicated with the orange dashed circles and lines in (a) and (c), respectively. The layer of material with n=1.72+0.0001i and thickness of 100 nm is indicated by the white dashed lines in (b) and (c). Electric field intensity maps at $\lambda = 428$ nm for (d) $x - y$ plane on top of the particles, (e) $z - x$ plane indicated in (d) with the black horizontal dashed line, and (f) $z - y$ plane indicated in (d) with the black vertical dashed line. The thickness of the layer with refractive index $n = 1.72 + 0.0001i$ is 100 nm. This layer is indicated with the white dashed lines in (e) and (f).

Figure 4.3 shows simulations of the electric field intensity enhancement (local field intensity normalized by the incident field intensity) in the bare cavity at 533 nm, i.e., the SLR peak wavelength and at 428 nm corresponding to the another peak in the absorption spectrum. These simulations are performed by considering a plane wave illumination at normal incidence and polarization along the x-direction. Figures 4.3 (a) and (d) corresponds to the $x - y$ plane at the top of the nanoparticles, while (b) (e) and (c) (f) are the cross sections in the $z - x$ and $z - y$ planes indicated by the dashed lines in (a). At 533 nm, we can observe in these figures a high field intensity enhancement close to the nanoparticles at due to the localized surface plasmon resonance (note that to highlight the SLRs, the color scale is saturated at an intensity enhancement of 10), and a field intensity enhancement extending over the array and in the thin layer on top as a result of the (1,0) and (-1,0) in-plane diffraction orders. While at 428 nm, the field intensity is high at positions between four adjacent particles, indicating that at this wavelength the field intensity enhancement is due to SLRs excited along both the x and y directions arising from both the (0,±1) and the (1,0), (-1,0) RAs (see Sec.1.5 in chapter 1).

It is worth mentioning that it is not possible to define the fitness value as the energy difference between the lower polariton (LP) and upper polariton (UP) in the coupled system. The Rabi splitting is defined by this energy difference only at the position in the dispersion diagram at which the bare states cross each other. A PSO algorithm based on a fitness value defined for the coupled system would not know a priory the energy and dispersion of the bare states, converging to a wrong set of parameters. This point is discussed in more detail in the next section and it is the reason why we chose a fitness value that is defined for the bare states.

Some constraints are imposed to the geometrical values and the fitness value calculation by the PSO algorithm: (a) $a > d + 50$ nm. This condition is imposed to ensure that the nanoparticles do not overlap and are sufficiently separated to be possible to fabricate them using electron beam lithography; (b) $F = 0$ when the wavelength difference between the SLR and the P3HT center exciton energy is $\Delta\lambda > 50, 40, 30$ and 20 nm in the 2-10, 11-20, 21-30, and 31-100 generations, respectively. This condition is imposed to ensure that the populations evolve to a solution in with the fitness value is maximum for overlapping resonances; (c) $F = \frac{2Pabs}{0.001}$ if $|\gamma_c - \gamma_p| < 0.001$. This condition is imposed to avoid the divergence of F when $\gamma_c = \gamma_p$.

4.4 PSO of the Coupling Strength

The PSO algorithm was run using 30 initial random populations of Al nanodisk arrays. The values of h, d and a were bounded to the ranges $10 - 100$ nm, $50 - 200$ nm, and $200 - 400$ nm, respectively. These range of values could be eventually realized experimentally.

The largest fitness value in the 1st generation was 3.73×10^2, and after 100 iterations the fitness value increased about 45 times to obtain a global best $F = 1.69 \times 10^4$, as can be seen in Fig. 4.4 (a) with a black line. In less than 50 generations, the PSO algorithm was able to find a geometry with dimensions that increase F to values close to convergence, showing the effectiveness of this method. The mean value of F of all populations are
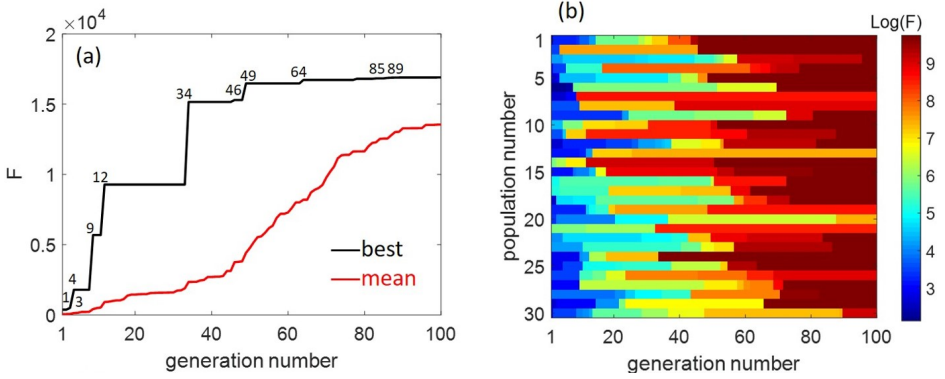
Figure 4.4: (a) Best (black line) and mean (red line) fitness value as a function of the generation number. The numbers indicate the generations at which the best fitness value of the populations evolves to a higher value. (b) Fitness value (log-color scale) for all the populations and generations.

shown in Fig. 4.4 (a) with a red line. This mean value approaches the global best value as the number of generations increases, as it could be expected when this global best attracts the other populations. [225, 229] Figure 4.4 (b) displays the fitness values (in a log-color scale) of each population and for all the generations, showing the increase of F for all the populations as they converge towards the best geometry.

Figure 4.5 (a) shows the normalized spectra of $P_a^c(\omega)$ and $P_a^p(\omega)$ for the 11 best populations during the full range of generations (the number gives the generation at which F increases, as it is also indicated in Fig. 4.4 (a), while Fig. 4.5 (b) displays the simulations of the optical power absorption enhancement calculated for the coupled systems with the same structural parameters as these best populations. The power absorption enhancement is defined as the power absorption in the P3HT layer of the coupled system, normalized by the power absorption of the bare P3HT layer to suppress the contribution of dark and uncoupled excitons. The best populations for the first 9 generations correspond to detuned SLR-exciton systems, as can be appreciated by the large wavelength difference between the P3HT absorption maximum (black-dotted curves in Fig. 4.5 (a)) and the maxima in absorption spectra of the bare particle array corresponding to SLRs (red-solid curves in Fig. 4.5 (a)). As a result of this detuning, indicated by δ in Fig. 4.5 (a), the difference between the LP and UP shown in Fig. 4.5 (b) does not correspond to the Rabi splitting. Only when the detuning between the bare states becomes sufficiently small, we can identify the maxima in the absorption spectra of the coupled system with the LP and UP states for zero detuning, defining the Rabi splitting. The Rabi splitting reaches a maximum of 0.7996 eV after 85 generations. This value is larger than the decay rates of the bare states obtained from the FWHM of the power absorption spectra, $\gamma_c = 0.5874$ eV, and $\gamma_p = 0.5881$ eV, and satisfies the criteria for strong coupling of coupled oscillators given in Eq. (4.6). The Rabi splitting corresponds to 34% of the exciton energy, which places the system at the onset of the ultra-strong coupling regime.[231]
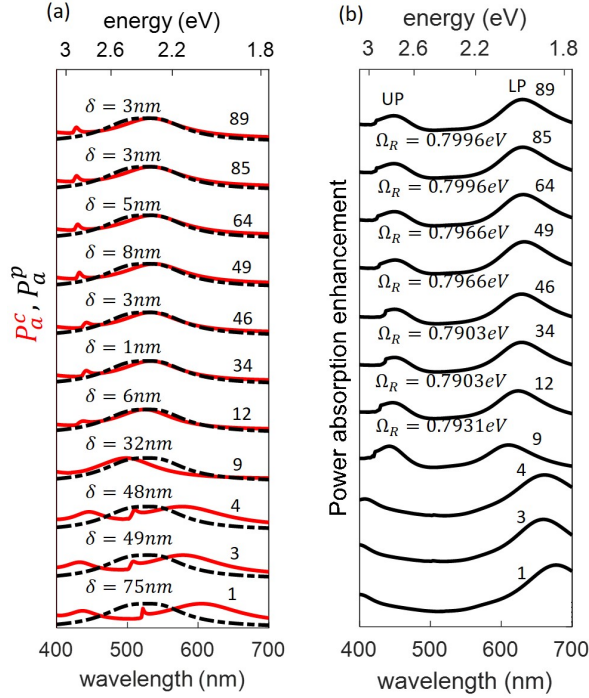
Figure 4.5: (a) Simulations of the power absorption spectra of a layer with refractive index n=1.72+0.0001i on Al nanoparticle arrays (red curves), and power absorption spectra of P3HT without nanoparticles (black-dashed curves). The simulations for the different arrays correspond to the 11 best populations during different generations indicated in Fig. 4.4 (a), which are labeled with a number that gives the generation at which F increases. (b) Absorption power enhancement of P3HT for the same samples as in (a), but considering the coupled system (P3HT layer on top a nanoparticle array). Lower and upper polariton peaks are labeled in the figure. The values of the Rabi splitting Ω_R are given for the generations 12 to 89, where the detuning between the bare states is small. The energy difference between the LP and UP for the generations 1-9 do not correspond to Ω_R due to the large detuning between bare states visible in (a) and characterized by δ. The spectra for the different populations are displaced vertically for clarity.

In PSO algorithms, the value of F depends on several parameters that gradually converge towards those defining the global best solution as F increases. To illustrate the convergence of the parameters in the optimization process, we show in Figs. 4.6 (a), (b) and (c) the mean (black curve) and standard deviation (SD) (red curve) of h (particle height), d (particle diameter), and a (lattice constant) for each generation, respectively. After 100 generations, we obtain the maximum value of F corresponding to an Al nanoparticle array with $h = 49 \pm 8$ nm, $d = 130 \pm 16$ nm, and $a = 279 \pm 10$ nm. From these values, we can see that the SD of the lattice constant is less than 4% of the mean, being the relative values of the SD of the diameter and height of the nanoparticles to their respective means. This
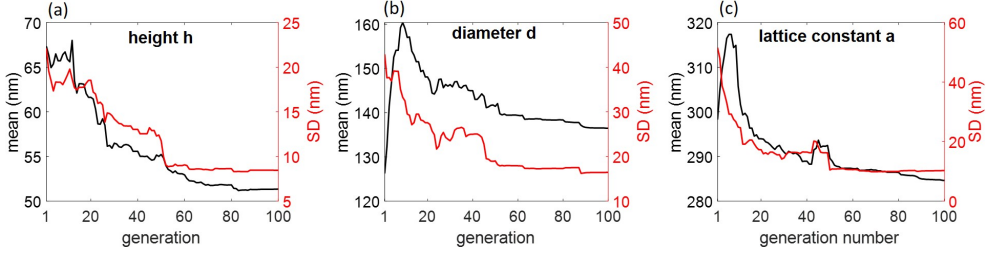
Figure 4.6: Mean of all the populations (black curve) and standard deviation (SD) (red curve) of (a) height h, (b) diameter d and (c) lattice constant a as a function of the generation number.
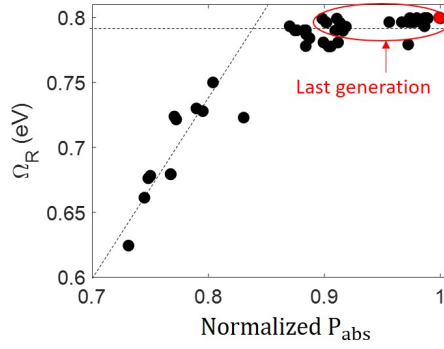
Figure 4.7: Rabi splitting as a function of P_{abs} normalized to its maximum value. The red ellipse indicates the arrays in the last generation. The red circle corresponds to the global best population of this last generation.

low relative SD suggests that the lattice constant is the most sensitive parameter for the optimization of the coupling strength and the one converging the fastest, which can be understood by the strong dependence of the linewidth of SLRs with the lattice constant in nanoparticle arrays. [79]

The relation between the Rabi energy and the power absorption integral defined in Eq. (4.8) is illustrated in Fig. 4.7 (a) for several populations in different generations, where we can see that Ω_R increases first linearly with P_{abs}, converging for large values of P_{abs} to approximately 0.8 eV. As expected, the last generation corresponds to the largest Rabi splittings as marked by the red ellipse in Fig. 4.7 (a). The global best population is indicated with the red data point.

4.5   Dispersion Measurements

Based on the results of the PSO algorithm, we have fabricated a sample with structural dimensions as close as possible to the optimal dimensions for coupling with excitons in P3HT. The sample was fabricated using electron-beam lithography (EBL) and reactive-ion etching (RIE). A 50 nm-thick polycrystalline Al layer was deposited on an eagle glass substrate by an electron-beam deposition at room temperature. A resist (nega-type, NEB22A2, Sumitomo, Japan) was spin-coated on the Al film and the array patterns were written by EBL (F7000S-KYT01, Advantest, Japan). After development of the patterns by a developer solution (SD-1), the Al film with a patterned resist was etched using RIE. After that, the remaining resist on top of the array was removed by an ashing process where oxygen plasma selectively etches the resist away. There is a 3 nm thick natural oxide layer (Al_2O_3) formed on top of the nanoparticles that gives the long-term stability needed for applications. An optical microscope image of the 200 μm × 200 μm array is shown in Fig. 4.8 (a), while a scanning electron microscope image of the nanoparticles with $a = 280 \pm 10$ nm, $d = 130 \pm 10$ nm is displayed in Fig. 4.8 (b).

The sample has been characterized by measuring the dispersion of the optical extinction using Fourier plane imaging spectroscopy.[232] For these measurements, a white light beam is focused onto the sample with a 40x objective (NA=0.6). The transmitted light through the sample is collected by another objective 60x objective (NA=0.7) and the back focal plane of this objective is imaged at the entrance slit of a spectrometer. The imaging spectrometer retrieves the transmission spectra as a function of angle. These measurements can be plotted in a dispersion diagram, representing the optical extinction as a function of the photon energy and the wave vector parallel to the surface, i.e., $k_{||} = (2\pi/\lambda)\sin\theta$. The related extinction is defined as $1 - T/T_0$, where T is the transmission through the sample and T_0 is a reference transmission measured through bare P3HT without sample.

The extinction measurements are shown in Fig. 4.8 (c) and compared with the simulations obtained with FDTD in Fig. 4.8 (d). These measurements and simulations correspond to the bare optical cavity, which has been fabricated by spin-coating a film of P3HT with a thickness of 100 nm on top of the Al nanoparticle array that has been photobleached using the expanded beam from a continuous wave laser of $\lambda = 445$ nm. By photobleaching, we remove the excitonic resonance in the P3HT layer while maintaining a thin dielectric layer on top of the Al nanoparticle array to reproduce experimentally the bare cavity shown in Fig. 4.3 (a). We note, however, that the refractive index of the bleached P3HT layer is ~1.5 (measured with ellipsometry), thus lower than the background refractive index of P3HT. The SLRs of the array in Figs. 4.8 (c) and (d) correspond to the bands of high extinction. We have also marked in these figures the in-plane non-degenerate (1,0), (-1,0) and the degenerate (0,±1) diffracted orders satisfying the grating equation. [233] The in-plane diffraction of the (1,0) and (-1,0) orders is responsible of the low-energy SLR that can couple to the P3HT excitons at 2.35 eV. This SLR is indicated in the figures and calculated using a damped coupled oscillator model with one oscillator representing the localized surface plasmon polaritons of the individual nanoparticles and other two representing the (1,0) and (-1,0) orders, [234] neglecting the mutual coupling between the diffraction
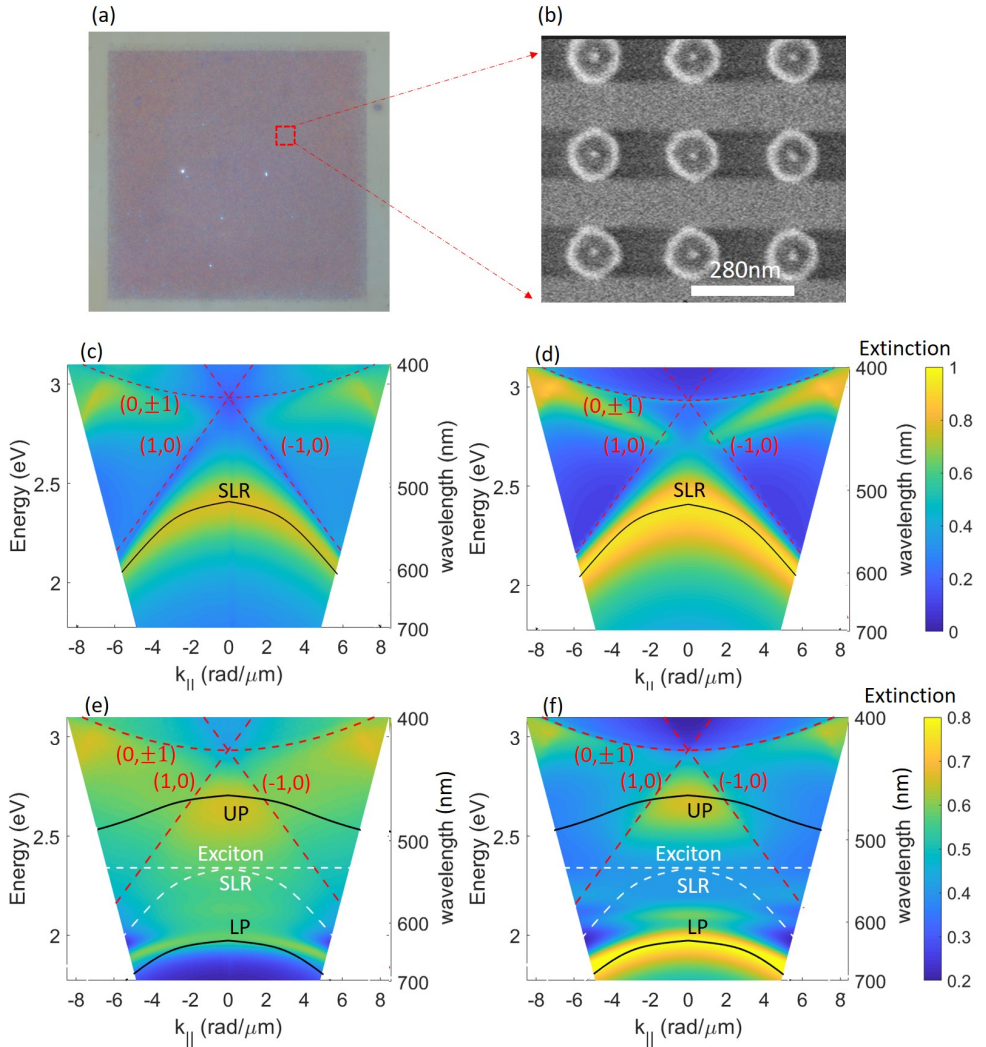
Figure 4.8: (a) Scanning electron microscopy image of the square array of Al nanoparticles. The scale bar corresponds to 280 nm. (b,d) Measurements and (c,e) simulations of the optical extinction of Al nanoparticle arrays covered with a 100 nm-thick layer of (b,c) bleached P3HT and (d,e) P3HT. The in-plane diffraction orders are indicated with dashed lines and curves for the (1,0), (-1,0) and (0, ±1) orders, respectively. The solid curves in (b) and (c) and white dashed curves in (d) and (e) represent the SLR. The fits to the LP and UP bands in (d) and (e), obtained with a coupled oscillator model that describes the interaction between the SLR and the excitons of P3HT (white-dashed lines), are given as black solid curves.

orders.

The coupling of the SLR to excitons in P3HT is demonstrated by the measurements and simulations shown in Figs. 4.8 (e) and (f). In these measurements and simulations, which correspond to the nanoparticle array with the P3HT layer on top before photobleaching, we can see the formation of the LP band at lower energies than the energy of the SLR of the bare particle array. Note that for the simulations, we have used the complex refractive index of P3HT retrieved from ellipsometry and shown in Fig. 4.1 (a) with the dashed curves. The SLR here is slightly red-shifted with respect to the SLR in the photobleached sample due to the higher refractive index of P3HT. The LP band has been fitted to the coupled oscillator model, described in previous section, to retrieve a Rabi energy of $\Omega_R = 0.74$ eV. This value of the Rabi splitting is smaller than the maximum value of 0.8 eV obtained from the PSO algorithm and the simulations, which can be explained by the fact that extinction measurements give the contribution of absorption and scattering to the spectrum, while the PSO algorithm was applied to only to absorption. As discussed in the literature, absorption measurements provide a more reliable value of the Rabi splitting than reflection, transmission or extinction measurements. [235–237] However, accurate absorption measurements need to be done using an integrating sphere to collected all the reflected and transmitted light intensities by the sample, which typically require a sample's size larger than the one used in our experiments. We also note in Figs. 4.8 (e) and (f) that the UP band calculated with the coupled oscillator model does not coincide with the band of large extinction over the whole range of wave vectors. This discrepancy can be attributed to the coupling to the $(0,\pm1)$ SLRs that can not be neglected at high energies. For completeness, we have also indicated with white-dashed curves and lines in Figs. 4.8 (e) and (f) the dispersion of the SLR in the bare cavity and the P3HT central exciton energy. The nearly flat band at 2.1 eV in Fig. 4.8 (f) corresponds to 0–1 intrachain excitons in P3HT, as can be also appreciated in the experimentally determined values of the optical constants of Fig. 4.1 (a). These excitons are not considered in the PSO calculations.

4.6   Conclusion

Using a Particle Swarm Optimization algorithm and finite differences in time domain simulations, we have determined the optimal size and lattice constant of square arrays of Al nanoparticles for strong coupling of surface lattice resonances with excitons in P3HT films. Through 100 generations of 30 populations, we retrieve a maximum Rabi splitting of 0.8 eV in these open optical cavities. We have also fabricated the Al nanoparticle array with optimized geometrical parameters and measured the optical extinction using back focal plane imaging spectroscopy. The experimental results show the formation of exciton polaritons in the strong coupling limit, in agreement with the simulated extinction. This work illustrates an efficient approach to optimize resonant structures for light-matter interaction in open systems that can be used in polaritonic devices.

EVOLUTIONARY OPTIMIZATION OF THE SHORT-CIRCUIT CURRENT ENHANCEMENT IN ORGANIC SOLAR CELLS BY NANOSTRUCTURED ELECTRODES

Using a Particle Swarm Optimization algorithm (a population-based stochastic optimization technique) combined with Finite Differences in Time Domain simulations, we inverse design periodic arrays of metallic nanoparticles on indium-tin-oxide electrodes and nanoholes in metallic thin films working as electrodes in P3HT-PCBM organic solar cells to achieve the maximum short circuit currents (J_{sc}). Nanohole-array electrodes have large optical losses, leading to a net reduction of J_{sc} compared to a reference solar cell. On the other hand, nanoparticle arrays can lead to a significant enhancement of J_{sc} of up to 20%. Detailed simulations show that this enhancement is caused by the grating coupling of the incident light to surface plasmon polaritons at the interface of the metal electrode and hole transport layer, leading to the enhancement of the electromagnetic field in the organic blend.

5.1 Introduction

Organic solar cells (OSCs) based on bulk heterojunctions are promising candidates for renewable energy sources thanks to their advantages compared to inorganic solar cells, such as low-cost, lightweight, and mechanical flexibility. [238] Significant progress has been made on OSCs processing, device configuration, and film morphology to achieve high power-conversion efficiencies (PCEs). [239–241]. However, organic materials have several drawbacks that impact the overall performance of solar cells. For example, the relatively low carrier mobilities and short exciton-diffusion lengths, [204] lead to typically very thin photo-active layers, of around 100 nm, which limits the light-absorption and the energy conversion efficiencies. [242]. Many efforts have been made to improve the PCE in OSCs by increasing the short-circuit current (J_{sc}), [243, 244] open-circuit voltage (V_{OC}), [245–247] or extending the absorption spectrum. [248] Resonant light trapping in organic solar cells has attracted a lot of attention in recent years, as it enables physically thin devices with high optical absorption. [249–251] Light absorption could be improved by implementing metallic nanoparticles or nanoholes arrays into solar cell devices. These structures can introduce plasmonic effects such as localized surface plasmon resonances (LSPRs), [252–254] surface plasmon polaritons (SPPs), [255] and quasi-guided modes [256] into OSCs. To introduce resonant structures in OSCs, a comprehensive analysis of their structure is required to optimize the size, [257] shape, [258] composition [259] and lattice constant [260]. Besides resonant metallic structures for light absorption, metallic nanomeshes and nanowire networks have also been considered as potential alternatives to indium-tin-oxide (ITO) electrodes. [255, 261]

In this chapter, we explore numerically using evolutionary optimization the potential of using plasmonic nanoparticle and nanohole arrays defining the cathode of P3HT:PC$_{61}$BM OSCs to enhance the generated short circuit current (J_{sc}) compared to standard devices with the same thickness of the organic blend. Two different OSC architectures are considered: Solar cells with periodic aluminum nanoparticles on top of the ITO electrode (nanoparticle array solar cell); and solar cells with nanohole arrays in an aluminum thin film acting as a conducting semitransparent electrode that replaces the ITO electrode (nanohole array solar cell). A Particle Swarm Optimization (PSO) algorithm, [81, 262] combined with Finite Difference in Time-Domain (FDTD) simulations, is used to determine the nanoparticle or nanohole dimensions and the square lattice constant for the maximum J_{sc} under 1 sun illumination. Our numerical simulations conclude that nanohole array electrodes always reduce the J_{sc} compared to standard devices due to their relative low transmission, despite being this transmission enhanced at defined wavelengths due to the excitation of SPPs. On the other hand, the plasmonic resonances of nanoparticle arrays on top of the ITO electrode enhances the J_{sc} by 20% in the optimized particle array by confining the electromagnetic field into the organic blend and extending the absorption spectrum of the solar cell.

Plasmonic nanoparticles can be made of a variety of materials, such as gold [263, 264] and silver [265–267]. However, the high cost or stability of these materials prevents their use in real applications. Therefore, we will limit our study to alumunium (Al) as inexpensive and stable material with a good plasmonic response in the visible. [268] Al nanopar-

ticles exhibit not only a resonant enhancement of light scattering and absorption due to plasmonic resonances, but they can act as quenchers of triplet excitons, improving the stability of the device. [269]

The chapter is organized as follows. Section 5.2 describes the geometries of the nanoparticle and nanohole array solar cells and illustrate with two examples the effect of nanostructuring the electrode on the absorption of the blend and the J_{sc}. In Section 5.3, we apply the PSO to retrieve the parameters of the arrays and the blend thickness giving the maximum enhancement of J_{sc}. Section 5.4 describes the mechanisms leading to this maximum enhancement in the nanoparticle solar cell. Finally, in section 5.5 we investigate the oblique angle illumination of the solar cell to retrieve the dispersion in the absorption.

5.2   Design of Nanoparticle and Nanohole Array Devices

A schematic representation of the investigated standard solar cell device is depicted in Fig. 5.1 (a). This device consists of a 120 nm thick layer of ITO as cathode on top of a glass substrate, a ZnO layer for electron transport with a thickness of 40 nm, a blend of P3HT:PC$_{61}$BM defining the bulk-heterojunction, a 10 nm MoO$_3$ layer for hole transport, and an Ag layer with a thickness of 100 nm acting as anode. The complex values of the refractive index of the blend that are used in the simulations are taken from the literature [255], and given in Fig. 5.1 (b) with the dashed curves. The solid curves in this figure are fits to the empirical results satisfying the Kramers-Kroning relations.

For the nanoparticle array solar cell, we design a square array of aluminum (Al) nanoparticles on top of the ITO cathode as depicted in Fig. 5.1 (c) to explore the optical absorption and the J_{sc} enhancement of the solar cell due to the electromagnetic field confinement in the blend. The Al nanoparticles, with diameter d and height h, are arranged in a periodic square array with a lattice constant a, and subsequent layers are conformally deposited on top.

For the nanohole array solar cell, a square nanohole array in an Al thin film simultaneously functions as a semi-transparent electrode to replace the ITO and to enhance the field in the blend, as shown schematically in Fig. 5.1 (e) with nanohole diameter d, height h, and lattice constant a. The holes are filled with ZnO obtaining a planar structure. We aim to explore the effect of the nanohole array in the device directly from the J_{sc} enhancement that represent the total contribution of the transmission through the structured electrode and the absorption in the active layer.

The absorbed power per unit volume can be calculated from the simulated electric field distribution

$$P_{abs}(x, y, z, \omega) = \frac{1}{2}\epsilon_0 \omega |E(x, y, z, \omega)|^2 \epsilon''(\omega), \tag{5.1}$$

where $E(x, y, z, \omega)$ is the electric field at coordinates x, y, z and at the angular frequency ω, ϵ'' is the imaginary component of the permittivity of the material at the same coordinates, and ϵ_0 is the vacuum permittivity. The absorbed power of the organic blend in the solar

cell can be calculated as

$$A(\omega) = \frac{1}{P_{source}} \iiint_V P_{abs}(x, y, z, \omega) \, dx \, dy \, dz, \tag{5.2}$$

where P_{source} is the power of the incident wave and V is the volume occupied by the blend. By assuming an internal conversion efficiency of the organic blend of 100%, i.e., the number of generated electron-hole pairs is equal to the number of absorbed photons, the short circuit current density of the solar cell can be determined as

$$J_{sc} = \frac{e}{\hbar S} \int_{\omega_1}^{\omega_2} \frac{A(\omega) S_{AM1.5}}{\omega} \, d\omega, \tag{5.3}$$

where e is the electron charge, $\hbar$ is Planck's constant, S is the surface area of the device and the $S_{AM1.5}$ is the AM 1.5 solar spectrum. The integral limits are defined by the absorption spectrum of the organic blend, i.e., ω_1 = 430 THz and ω_2 = 1000 THz, corresponding to wavelengths in the range 300 to 700 nm. The simulations are done for an incident wave with an amplitude of $1 V/m$ and a spectral range covering the absorption of the blend.
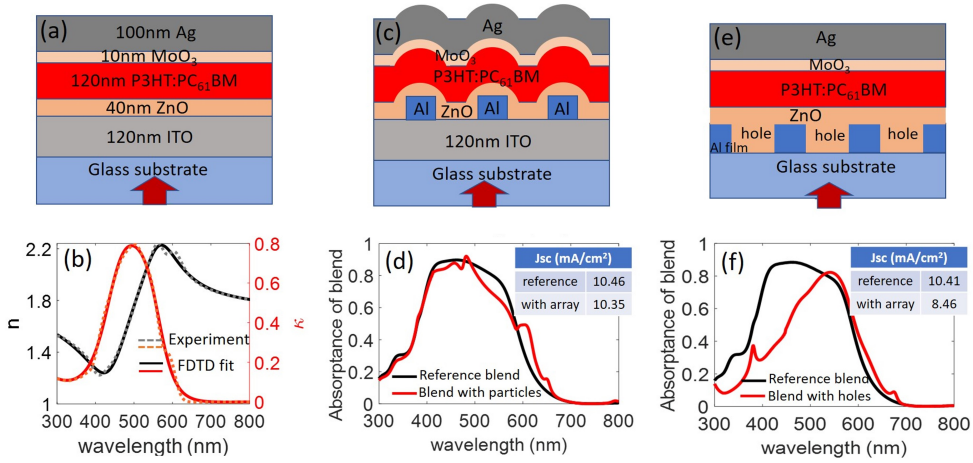

Figure 5.1: Schematic cross sections of the layer stack of (a) the reference solar cell, (c) the nanoparticle array solar cell, and (e) the nanohole array solar cell (e). (b) Experimental refractive index (n) and extinction coefficient (κ) of P3HT:PC$_{61}$BM from Ref. [255] (dashed curves). The fits to the experimental values used for the FDTD simulations are displayed with solid curves. (d) Absorptance of P3HT:PC$_{61}$BM in the reference solar cell (black curve) and in the Al nanoparticle array solar cell (red curve, period a = 400 nm, diameter d = 120 nm, height h = 30 nm and thickness of blend t = 120 nm). The J_{sc} values for both solar cells are given in the inset. (f) Absorptance of P3HT:PC$_{61}$BM in the reference solar cell (black curve) and in a nanohole array solar cell (red curve, a = 307 nm, d = 257 nm, h = 52 nm and t = 123 nm). The J_{sc} values for both solar cells are given in the inset.

To illustrate these calculations, we display the absorptance spectrum of the blend in Fig. 5.1 (d) with the red curve for a nanoparticle array solar cell with d = 120 nm, h = 30 nm,

a = 400 nm, and a 120 nm thick layer of blend under normal illumination. For comparison, the absorptance spectrum of a standard solar cell with the same thickness of blend is plotted with a black curve. We observe that the absorptance for the nanoparticle array solar cell increases around 600 nm. The absorptance is reduced at shorter wavelenghts, with the exception of 480 nm, leading to a net reduction of J_{sc} compared to the reference device as indicated in the inset table of Fig. 5.1 (d).

Similarly, we also calculate the absorptance spectrum of the blend in a nanohole array solar cell with d = 257 nm, h = 52 nm, a = 307 nm, and 123 nm thickness of blend. The result is displayed in Fig. 5.1 (f) with a red curve, where also the absorptance of the reference solar cell is plotted for comparison with a black curve. As shown in the inset table of Fig. 5.1 (f), and despite a slight absorptance enhancement that can be observed around the long-wavelength absorption edge of the blend, J_{sc} is greatly reduced compared to the reference due to the lower reduced optical transmittance through the nanohole array.

Although J_{sc} is not improved by introducing the nanoparticle and nanohole arrays into solar cell devices for the above examples, the absorptance spectrum is greatly affected by resonances in these arrays. Next, we optimize the size of nanoparticles and nanoholes, the period of the arrays and the thickness of the blend to achieve the maximum J_{sc}, which eventually improves the J_{sc} of the equivalent devices without structured electrodes and we analyze the main resonances in the arrays contributing to the J_{sc}.

5.3 Particle Swarm Optimization of the Short-Circuit Current Enhancement

We incorporate the concept of evolutionary optimization in the form of a PSO algorithm to find best structural parameters of the nanoparticle and nanohole arrays. This optimization is done by performing FDTD simulations that yield the highest possible J_{sc} enhancement in OSCs. [81, 270] The J_{sc} enhancement is defined as $(J_{sc}/J_{sc}^{ref} - 1) \cdot 100\%$, where J_{sc}^{ref} is the short circuit current of the reference solar cell with the same thickness of the blend but with a flat ITO electrode instead of the nanohole array or the ITO with a nanoparticle array on top.

The PSO algorithm is used to optimize the J_{sc} enhancement by iteratively improving the parameters. It calculates a J_{sc} enhancement by having a population of solar cell devices that evolve towards the optimum by changing parameters in the search space. Each population change is influenced by its local best-known parameters, but is also guided toward the best-known parameters in the search space, which are updated as better parameters are found by other populations. This procedure is expected to move the populations toward the global best set of parameters that correspond to the maximum J_{sc} enhancement.

The diameter d and height h of the cylindrical nanoparticles and nanoholes, the period of the square array a, and the thickness of the blend t for light-harvesting are the parameters that are optimized. For the nanoparticle array solar cells, these parameters are varied in the ranges d = 20 - 200 nm, h = 20 - 80 nm, a = 200 - 500 nm and t = 80 - 140 nm; while for the nanohole array solar cells are varied in the ranges d = 20 - 500 nm, h = 20 - 150 nm, a = 200 - 600 nm and t = 80 - 140 nm. These ranges are limited by values that can

be fabricated using standard lithographic and spin-coating techniques, such as electron beam or nanoimprint lithography.
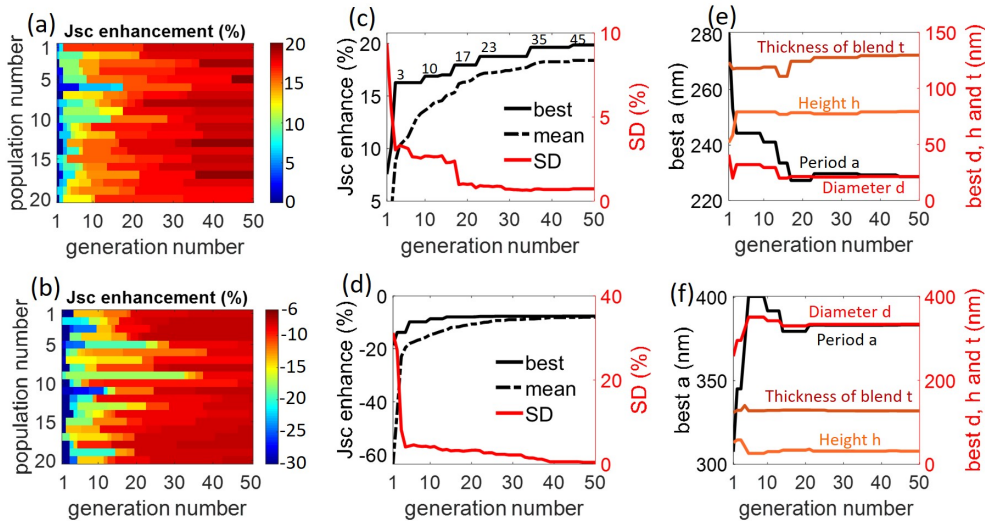

Figure 5.2: J_{sc} enhancement of (a) nanoparticle array solar cells, and (b) nanohole array solar cells for all the populations and generations of PSO evolutions. (c) and (d) display the best (black lines), mean (black-dash lines) and standard deviation (red lines) values of J_{sc} enhancement as function of the generations of the PSO for particle array solar cells and hole array solar cells, respectively. The numbers indicate the generations at which the best J_{sc} enhancement value of the populations evolves to a higher value. (e) and (f) show the period a (black lines), diameter d (red lines), height h (pink lines), and thickness of the blend t (dark-red lines) of the best population as a function of the generation number for nanoparticle and nanohole array solar cells, respectively.

Twenty populations are allowed to evolve during fifty generations, as illustrated in Fig. 5.2 (a). This evolution for nanoparticle array solar cells shows an increase in J_{sc} for all the populations as they converge toward the optimum device geometry. This geometry corresponds to a J_{sc} enhancement of $\approx 20\%$ and parameters $d = 21.4$ nm, $h = 79.7$ nm, $a = 228.6$nm, and $t = 129.4$nm. For the nanohole array solar cells, we always retrieve a reduction of the J_{sc} with a minimum value of 6%, which corresponds to the parameters of $d = 333.5$ nm, $h = 31.2$ nm, $a = 383.5$ nm, and $t = 127.2$ nm. The evolution of the J_{sc} in the twenty populations of nanohole array solar cells is illustrated in Fig. 5.2 (b). Even thought the transmission through a hole array can be enhanced at selected wavelengths by the excitation of surface plasmon polaritons, [271] this enhanced resonant transmission can not compensate for the high reflection at other wavelengths and the absorption in the metal layer, which give rise to a net reduction of J_{sc}.

The best J_{sc}, mean value of J_{sc}, and standard deviation (SD) for each iteration or generation number are displayed in Figs. 5.2 (c) and (d) for the particle and nanohole array devices, respectively. These figures illustrate the convergence of the maximum J_{sc} and the mean towards the highest J_{sc}, and the reduction of the SD during the evolution. To

illustrate the changes of the parameters of the population with the highest J_{sc} as a function of the generation number, we show in Fig. 5.2 (e) for the nanoparticle array solar cells, and in Fig. 5.2 (f) for the nanohole solar cells, the period a (black curve), diameter d (red curve), height h (pink curve), and thickness of organic blend t (dark-red curve) for this best population. It is worth noting that all the parameters remain nearly constant after 23 generations, which illustrates the relative fast convergence of this method.

5.4 Investigation of the Optimum Nanoparticle Array Device

Based on the results of the PSO algorithm, J_{sc} can be significantly enhanced by a nanoparticle array on top of ITO. In this section, we describe the mechanisms responsible for this enhancement. The refractive index n and extinction coefficient k of the different materials forming the solar cell are shown in Fig. 5.3. Besides the organic blend and the Ag anode, the other materials exhibit almost no absorption in the visible, with the absorption increasing in the UV. Therefore, mainly the organic blend (donor) absorbs photons under sun light illumination, forming the excitons that have to be dissociated at the interface between the donor and acceptor. Electrons are collected at the transparent ITO cathode through the electron transport layer (ZnO), while holes are collected at the Ag anode through the hole transport layer (MoO$_3$).

Figure 5.4 (a) shows the absorptance spectrum calculated in the volume occupied by the organic blend in the device with the optimum nanoparticle array for a maximum J_{sc} (black curve). This spectrum is compared to the absorptance of the blend in a standard (reference) device (dashed curve in Fig. 5.4 (a)). The absorptance is enhanced by the nanoparticle array over the full visible spectrum, being reduced at short wavelengths (<360 nm). The red curve in Fig. 5.4 (a) represents the absorption enhancement in the organic blend by the nanoparticle array, calculated as the ratio between the absorptance in the blend of the nanoparticle device and the absorptance in the blend of the reference device. There are two clear peaks in the spectrum of the absorption enhancement, located on the absorption edges of the organic blend.

We have calculated the absorptance spectrum in the volume occupied by the Al nanoparticles to characterize the loss introduced by the plasmonic nanostructures. This absorptance, shown in Fig. 5.4 (a) with the blue curve, is negligible compared to the absorption in the blend. Furthermore, the absorptance spectra of the electrodes and transport materials are given in Fig. 5.5. The total reflectance and absorptance spectra of the solar cells are displayed in Fig. 5.4 (b) with black and red curves, respectively; and for the nanoparticle array solar cell and the reference solar cell (solid and dashed curves, respectively).

To sort out the mechanism leading to the enhanced absorption of the nanoparticle array in the solar cell, we investigate the electric field intensity integrated in the xy-plane as a function of position in the z-direction and wavelength, as shown in Fig. 5.4 (c) for the reference solar cell, and in Fig. 5.4 (d) for the nanoparticle solar cell. The field in the blend for the reference solar cell is mainly enhanced at $\simeq 340$ nm and $\simeq 700$ nm due to Fabry-
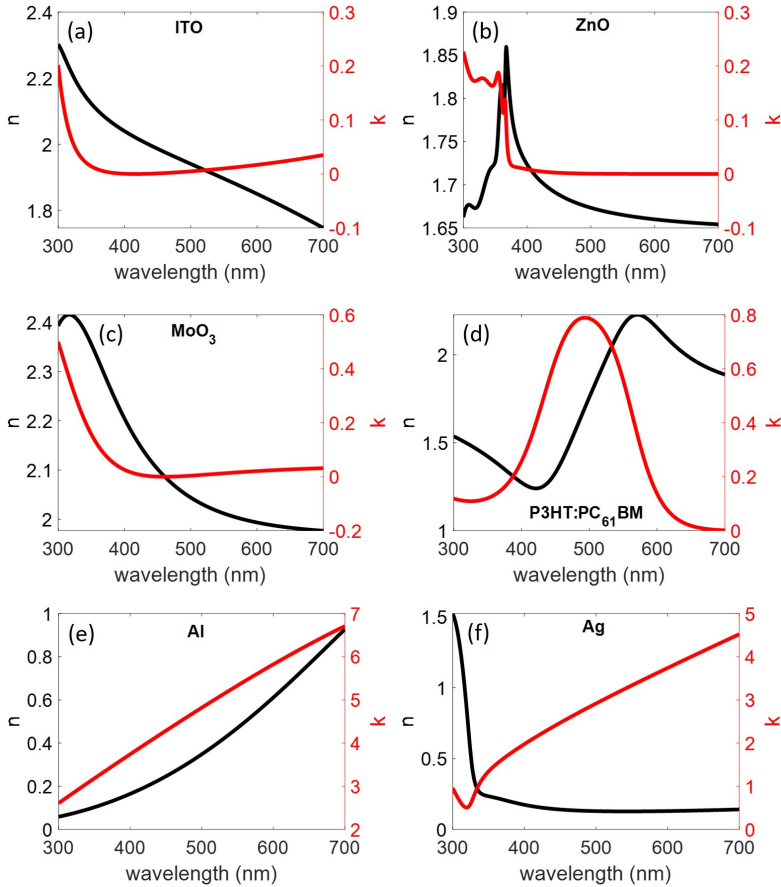
Figure 5.3: Complex refractive index of the (a) ITO, (b) ZnO, (c) MoO$_3$, (d) P3HT:PC$_{61}$BM, (e) Al and (f) Ag.

Perot resonances in the planar cell structure. The resonant field enhancement at 700 nm does not contribute to the net solar cell absorption due to the low extinction coefficient of the blend at these wavelengths.

The resonant field enhancement due to the Fabry-Perot resonances in the nanoparticle solar cell is reduced compared to the reference solar cell (see Fig. 5.4 (d)). However, a pronounced enhancement of the field close to the Ag anode-MoO$_3$ layer is apparent at 635 nm. We attribute this enhancement to the diffractive coupling of the incident light to surface plasmon polaritons (SPPs) at the Ag interface. This excitation of SPPs contributes to a 2.5-fold absorption enhancement in the blend. In addition, it results in absorption peaks in Ag and MoO$_3$, but a reduction of the absorption in ITO, as shown in Fig. 5.5. The SPP corresponds to a minimum of the reflectance and a peak of the total absorptance of the full device, as can be seen in Fig. 5.4 (b).
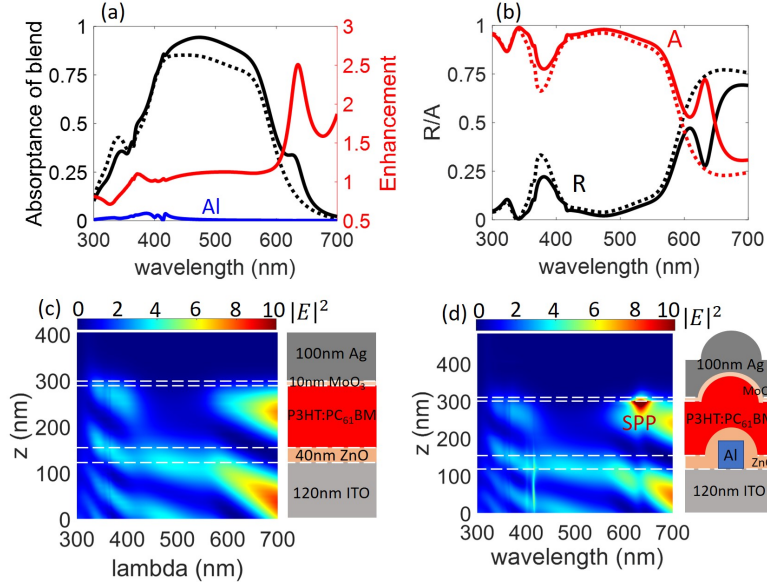
Figure 5.4: (a) Absorptance spectra of the blend in the optimal nanoparticle array solar cell (black curve), in the reference solar cell with the same thickness of blend (dashed-black curve) and the absorption enhancement (red curve). The absorptance in the Al nanoparticles is plotted as a blue curve. (b) Total reflection (black curves) and absorptance (red curves) of the optimal nanoparticle array solar cell (solid curves) and reference solar cell (dashed curves). (c) and (d) are the electric field intensity $|E|^2$ integrated in the xy-plane and in the wavelength range 300-700 nm as function of height for the reference solar cell and the optimal nanoparticle array solar cell, respectively. The dashed lines indicate the height of the different interfaces. The cross sections of the solar cells are schematically represented on the right panels of (c) and (d).

To investigate the effect of the corrugation introduced by the nanoparticle array that is responsible for the diffractive coupling to SPPs and to exclude a possible effect of the nanoparticles, we have simulated a similar corrugated solar cell but without nanoparticles. These results are given in Fig. 5.6, showing a similar enhancement of the absorptance in the organic cell and of J_{sc}, albeit having slightly lower values. This result supports the interpretation that the main mechanism leading to the increased absorption are SPPs at that Ag electrode. Nanoparticles are needed to form the periodic structure and corrugation that enables the diffractive coupling to SPPs. However, the material forming these nanoparticles is not as critical as could be initially expected. Further improvement in the absorption could be attained by considering periodic lattices with a higher rotational symmetry, such as hexagonal arrays.
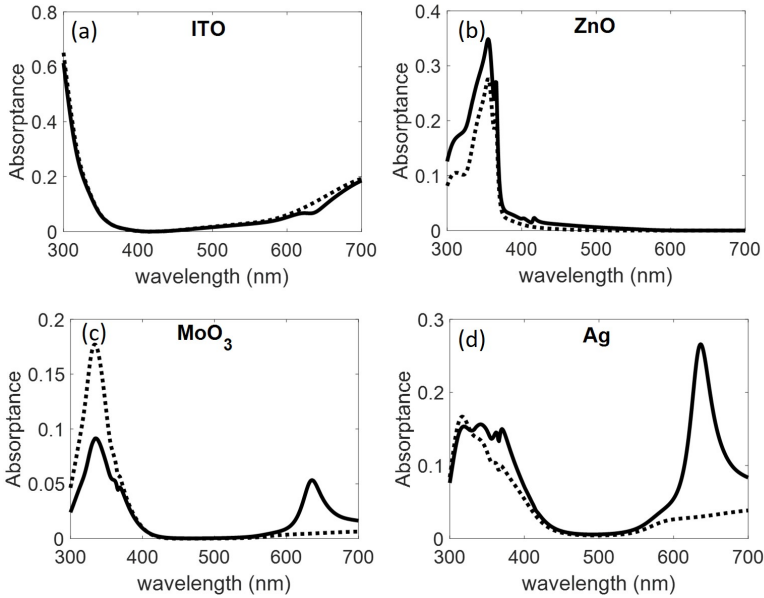
Figure 5.5: Absorptance spectra of (a) ITO, (b) ZnO, (c) MoO$_3$, and (d) Ag in the reference
solar cell (dashed curves) and optimal nanoparticle solar cell (solid curves).
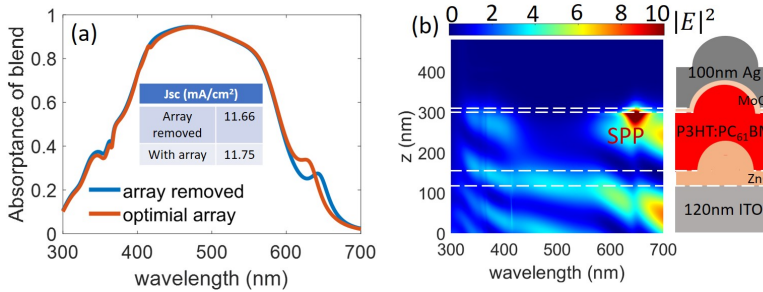
Figure 5.6: (a) Absorptance spectra of the organic blend for the optimal nanoparticle array
solar cell (orange curve) and a similar solar cell but without nanoparticles (blue curve).
Inset: J_{sc} of both solar cells. (b) Electric field intensity $|E|^2$ integrated in the xy-plane of the
solar cell without nanoparticles plotted as a function of wavelength and height. Dashed
lines indicate the interfaces between layers of the device with a schematic representation
on the right.

5.5   Oblique Angle Illumination

To investigate the dispersive response of the nanoparticle array solar cell, we have sim-
ulated the absorptance under oblique angle illumination. The absorptance dispersion
diagrams for TM polarization are plotted in Fig. 5.7 (a) for the reference solar cell (left

panel) and the nanoparticle array solar cell (right panel). These dispersion diagrams represent the absorptance of the blend as a function of the photon energy/wavelength and the wave vector component of the incident wave parallel to the surface, i.e., $k_\parallel = (2\pi/\lambda)sin(\theta)$, where θ is the angle of incidence. The dispersions are symmetric with respect to normal incidence ($k_\parallel = 0$); therefore, we only plot them for negative and positive angles, respectively, to facilitate their comparison. As can be appreciated, the absorptance of the blend is enhanced in almost the entire angular dispersion, apart from the UV region where the Fabry-Perot resonance in the planar structure is reduced by the nanoparticles.
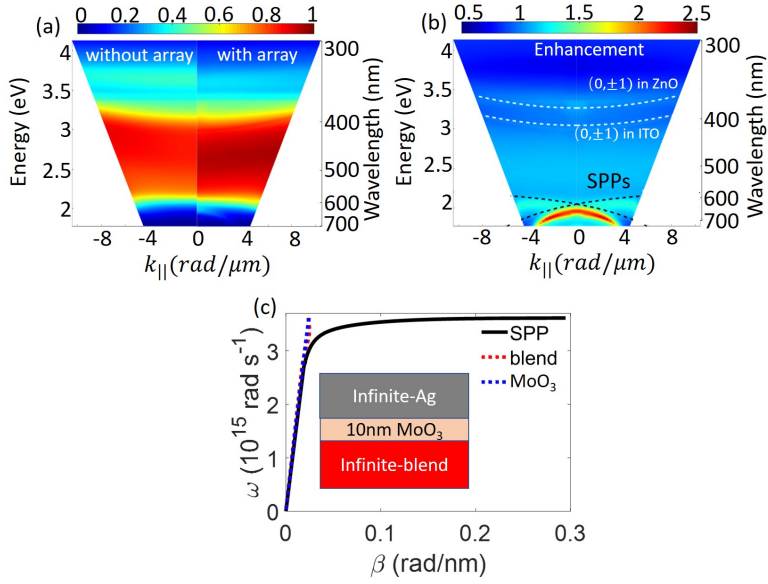

Figure 5.7: (a) Absorptance dispersion of the organic blend in a reference solar cell (left) and in the optimal nanoparticle array solar cell (right). (b) Absorption enhancement of the organic blend for the nanoparticle solar cell. The dispersion of grating coupled SPPs and in-plane diffraction orders (Rayleigh anomalies) are indicated with black-dotted and white-dotted curves, respectively. (c) Dispersion relation of SPPs in an Ag/MoO$_3$/blend three-layer system with a MoO$_3$ thickness of 10 nm (black curve). The light cone of the organic blend (dashed-red line) and MoO$_3$ (dashed-blue line) are also plotted.

The dispersion absorption enhancement is plotted in Fig. 5.7 (b). The main features in this figure are the enhancement peaks that, as we show next, follow the dispersion of SPPs. To determine the SPPs dispersion, we firstly calculate the SPP wave number for a three-layer system, consisting of semi-infinite Ag and blend, separated by a layer of 10 nm of MoO$_3$. The dispersion relation can be obtained by calculating the eigenstates of this three-layer system, given by

$$e^{-2k_1 l} = \frac{k_1/\epsilon_1 + k_2/\epsilon_2}{k_1/\epsilon_1 - k_2/\epsilon_2} \frac{k_1/\epsilon_1 + k_3/\epsilon_3}{k_1/\epsilon_1 - k_3/\epsilon_3}, \tag{5.4}$$

and

$$k_i^2 = \beta^2 - k_0^2 \epsilon_i, \tag{5.5}$$

with i=1,2 and 3 corresponding to MoO$_3$, Ag and the blend, respectively, and $l = 10$ nm is
the thickness of MoO$_3$. The dispersion of the SPP at the interface Ag-MoO$_3$/blend is dis-
played in Fig. 5.7 (c). At low frequencies, the SPP dispersion (black curve) approaches the
light cones of the blend (dashed-red line) and of MoO$_3$ (dashed-blue line). However, the
incident plane wave onto the nanoparticle solar cell acquires an additional momentum by
scattering with the periodic lattice, leading to the diffraction coupling condition to SPPs:

$$\beta = k_\parallel + \frac{2\pi}{a}(i\,\hat{u}_x, j\,\hat{u}_y), \tag{5.6}$$

where (i, j) is the order of diffraction in the x- and y-directions, and a is the period of
square array. Here, we focus on the in-plane (1,0) and (-1,0) diffraction orders from the
array, defined by the polarization of the incident wave. The calculated SPPs dispersion is
plotted with the dotted-black curve in Fig. 5.7 (b). This dispersion follows the simulated
dispersion bands of enhanced absorption, confirming that these bands result from the
grating coupling of the incident wave to SPPs at the Ag interface.

We also see in Fig. 5.7 (b) bands with a weaker absorption enhancement. These bands
follow the dispersion of Rayleigh anomalies (RAs), i.e., in-plane diffracted orders, which
can be calculated with the grating equation considering that the diffracted wave is on the
plane of the array. [45] The white-dotted curves in Fig. 5.7 (b) represent the calculation of
these RAs for the degenerate (0,±1) diffraction orders. Considering that the nanoparticle
array is placed on top of ITO and covered by the layer of ZnO and the organic blend, two
RAs are apparent, corresponding to the upper and lower media. Both RAs slightly increase
the absorption due to the diffraction of the incident wave in the plane of the array.

5.6   Conclusions

To summarize, we have investigated the J_{sc} enhancement of organic solar cells with
nanostructured electrodes formed by Al nanoparticle or nanohole squared arrays. By
combining a particle swarm optimization algorithm with finite difference in time-domain
simulations, the structural parameters of the arrays and the thickness of the organic
blend layer have been optimized to maximize the J_{sc} enhancement of the solar cell. The
optimal nanoparticle array solar cell reaches a remarkable 20% enhancement of the J_{sc}
compared to a standard planar solar cell, which is mediated by the grating coupling of the
incident light into surface plasmon polaritons at the Ag electrode interface and in-plane
diffraction orders. However, the J_{sc} is reduced even for the optimum nanohole array
due to the reduction of coupling of the incident light into the active blend of the organic
solar cell. These findings reduce the applicability of nanohole arrays as semitransparent
electrodes replacing ITO, but highlight the potential improvement of organic solar cells
with nanoparticle arrays on top of ITO.

COUPLED SURFACE PLASMON POLARITONS AND DARK GAP PLASMONS IN PERIODIC ARRAYS OF NANOPATCH ANTENNAS

Systems formed by metallic nanoparticles separated by a thin dielectric layer from a metal film, the so-called nanopatch antennas, have attracted significant interest due to their capacity for confining electromagnetic radiation in tiny volumes. We perform a systematic study on randomized versus periodic silver nanopatch antennas (Ag nanodisks separated from an Ag layer by a HfO_2 thin film). Combining experiments and simulations, the origin of different plasmonic resonances in these systems are identified. The differences between the randomized and periodic cases are presented, showing that the electromagnetic field can be noticeably enhanced when the randomized nanodisks are organized into periodic arrays. A hybrid plasmonic mode was observed in the periodic case, which originates from the coupling of a lattice surface plasmon polariton (SPP) in the metal film and a dark gap mode in the nanodisks with a mode splitting of 0.5 eV. Furthermore, a bound state in the continuum (BIC)-like mode is formed by the suppression of the radiation losses in the direction normal to the surface, leading to quality factors (Q-factors) larger than 50. These results of large mode splitting, substantial Q-factor in a metallic system and large-area distribution of enhanced electric fields illustrate the richness of the plasmonic modes in these hybrid systems.

6.1 Introduction

A surface plasmon is the collective oscillation of free charges on metal particles or films that can be excited by electromagnetic waves [272]. Generally, metal films support surface plasmon polaritons (SPPs), while metallic nanoparticles support localized surface plasmon resonances (LSPRs). Both of these resonances can confine electromagnetic waves in sub-wavelength volumes and their response can be tuned by the geometry, materials and the medium surrounding the metal film or nanoparticles. [36, 273, 274] This flexibility makes them well suited for a range of applications such as biosensors [275], solar cells [276], photo-catalysis [277], and linear/nonlinear optics [40, 278, 279]. Merging nanoparticles and metal films into coupled systems can further enrich their optical response. The interplay between SPPs and LSPRs at different metal/dielectric interfaces in these hybrid systems lead to phenomena such as Fano resonances [280], broadband super absorption [281], and the reduction of the extinction through metal films.[282–284]

There have been several studies on the hybridization of LSPRs and SPPs [273, 285, 286], which either focus on the interaction between a single nanoparticle-dielectric-metal film (nanopatch antenna) or between a nanoparticle array-dielectric-metal film (nanopatch antenna array). A detailed study and comparison between plasmonic modes of randomized nanodisk arrays and periodic nanodisk arrays on metal films is not yet reported. To elucidate the interplay between SPPs and LSPRs, and the evolution of plasmonic modes in the process of transforming the structure from a randomized to a periodic array is particularly interesting since gratings play an important role in the excitation of SPPs at the interface of metal films and in the enhancement of the optical response. [40, 41, 51, 287]

Two different types of plasmonic modes have been identified in nanopatch antennas: localized longitudinal nanoparticle modes L_{mn} and transverse gap SPP modes S_{mn} produced at the thin dielectric gap that is surrounded by metal [288–292]. The m and n subindexes refer to the azimuthal number and the mode order. The localized longitudinal modes depend strongly on the height of the nanoparticles, whereas the gap SPP modes depend on the thickness of dielectric layer. These two type of modes and their interaction can be thus independently tuned in hybrid systems [288]. Furthermore, transverse gap SPP modes have an extremely large Purcell factor because of the strong field confinement in the dielectric layer. Longitudinal nanoparticle modes have a weaker Purcell enhancement factor but a larger emission efficiency [291]. To simultaneously obtain high Purcell enhancement factors, high emission quantum efficiency, and directional emission, dielectric nanoparticles are promising substitutes for the metallic nanoparticles on metallic films [293].

In this chapter, we investigate randomized and periodic nanoantenna patch arrays formed by Ag nanodisks on a thin layer of HfO_2 on top of an Ag film. The experimental spectra and dispersion of randomized and periodic nanopatch antenna arrays are systematically studied, finding that the electromagnetic fields of both longitudinal nanoparticle modes and transverse gap modes are enhanced noticeably by ordering the nanodisks into periodic arrays. More interestingly, a BIC-like hybrid plasmonic mode is present in the periodic case. With the help of the numerical (FDTD) simulations, the plasmonic resonances in these systems have been investigated and the mechanism

leading to the BIC-like plasmonic mode has been identified.

6.2 Sample Description and Morphological Characterization

The schematics of the investigated samples are displayed in Fig. 6.1 (a). The top panel shows the side view of the structure, and the other two panels below illustrate the periodic and randomized arrays. The Ag film is thicker than 150 nm; hence, its optical response can be considered as that of bulk silver. Therefore, only the silver film-HfO_2 interface needs to be considered as essential for the optical response of the samples. The thicknesses of the
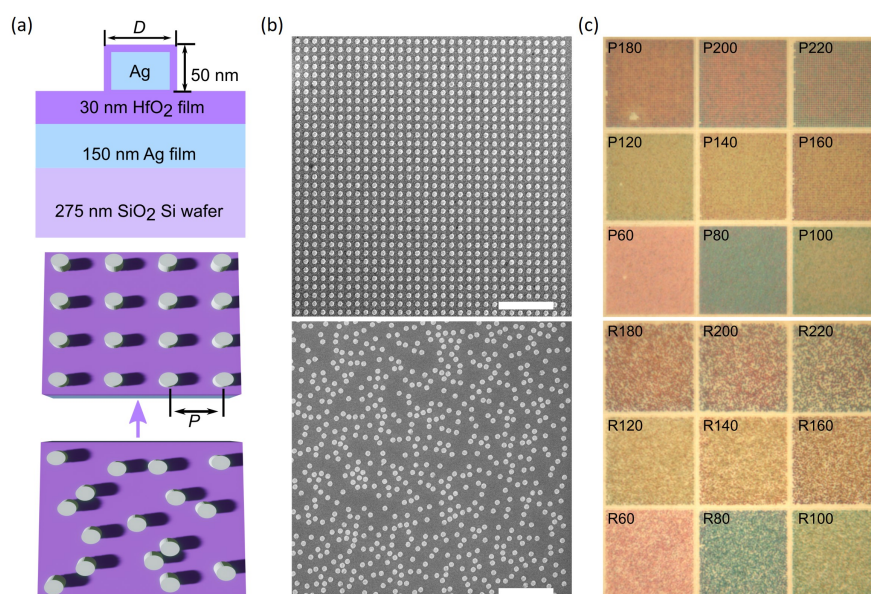

Figure 6.1: (a) Sample configurations. D is the diameter of nanodisk and P is the pitch size of the square array. (b) Scanning electron microscope images of periodic nanodisks (top) and randomized nanodisks (bottom), respectively. The scale bars are 2 μm. (c) Optical images of periodic/randomized nanodisks with diameters from 60 nm to 220 nm. The size of each square area is 20×20 μm^2. The nanodisk coverage ratios are the same for the randomized and periodic arrays with same nanodisk diameter. The label "Px" means that it is a periodic nanodisk array with the diameter of the nanodisk of x nm, while "Rx" means that it is randomized nanodisk array.

HfO_2 spacer layer and the height of the Ag nanoparticles are fixed to 30 and 50 nm, respectively. The high quality of the samples is confirmed by the scanning electron microscopy (SEM) images displayed in Fig. 6.1 (b). The upper and lower panels in this figure show the periodic and randomized nanodisks with the same diameter, D = 160 nm, respectively. The variation in the diameter of the nanodisks between samples is controlled below 5 nm,

which ensures the reliability of the detailed comparison in the follow up analysis. Besides
the uniform diameter, the neighboring nanodisks are well separated in the random case.
To avoid overlap, the randomized positions of the nanodisks are computed by keeping a
distance of neighboring nanodisks of no less than 40 nm. Figure 6.1 (c) shows the bright-
field optical microscope images of randomized (bottom) and periodic nanodisks (top)
arrays with diameters ranging from 60 to 220 nm. The color of the nanodisks changes
systematically along with the increase of disk diameter. This color change is especially
visible in the diameter range from 60 to 100 nm. From the optical images, it is already
conclusive that the apparent color is determined by the size of the nanodisks and not by
the ordering. This observation suggests that the localized plasmonic resonances of the
single silver nanodisks play a key role in determining the optical response of the samples.
When the arrangement of the nanodisks is disordered, the color is not very uniform as a
result of the interactions between neighboring nanodisks at different distances, which is
in clear contrast to the uniform colors found for the periodic arrays.

6.3 Optical Characterization and Discussion

To characterize the plasmonic resonances in the randomized and periodic arrays of
nanopatch antennas in more detail, we have measured the reflectance dispersion using a
Fourier miscroscope. A collimated white-light beam from an halogen lamp is focused on
the sample through a 0.9 NA objective (Nikon Plan Fluor 100x). The back focal plane of
the objective lens is imaged on a spectrometer slit with a 4f system. These measurements
can be plotted in a dispersion diagram, resolving the reflectance as a function of the angle
of incidence θ.

6.3.1 Plasmonic Modes in Randomized Nanodisk Arrays

We first describe the plasmonic resonances identified in the reflectance spectra of ran-
domized nanodisks with a diameter of 120 nm. The corresponding angular reflectance dis-
persion is shown in Figs. 6.2 (a) (c) and it is compared to the simulation of the absorption
efficiency of a single nanodisk in Figs. 6.2 (b) (d) for TM-polarized light. Both simulated
and measured resonances at 447 and 778 nm do not depend on the angle of incidence,
which is consistent with their localized character to individual nanopatch antennas. These
resonances, shown in more detail in Fig. 6.3 with the dips in the reflectance and peaks in
the absorption efficiency spectra for normal incidence, correspond to the transverse gap
SPP S_{11} mode and the longitudinal nanoparticle L_{11} mode. The S_{11} and L_{11} modes can
be better recognized by simulating the spatial distribution of the electric field in the xz-
plane and xy-plane at the two resonant wavelengths. These fields are shown in Fig. 6.3 (b).
The color scales represent the amplitudes of real part of the $z-$component of the electric
field and the black-dashed lines show the boundaries of the Ag disk and the HfO$_2$ film.
For the resonance at 778 nm, the electric field is mainly confined at the bottom of the
disk and extends into the HfO$_2$ layer. This distribution indicates that this resonance can
be associated to the transverse gap SPP mode in the metal-insulator-metal structure. The

gap SPP reflects at the edges of the nanoparticle forming an standing wave that leads to the resonance. The electric-field distribution in the horizontal plane at the bottom of disk allows to identify this resonance with the S_{11} mode, which has a single node and opposite phase at the edges of the nanodisk. The bottom panels of Fig. 6.3 (b) correspond to the electric field calculated at 447 nm. This field is mainly concentrated at the top of the nanodisk, indicating that this is a localized longuitudinal mode. According to the in-plane electric-field distribution on top of the disk, as shown in the bottom right panel of the Fig. 6.3 (b), this resonance can be associated to the localized longitudinal L_{11} nanopatch entenna mode.
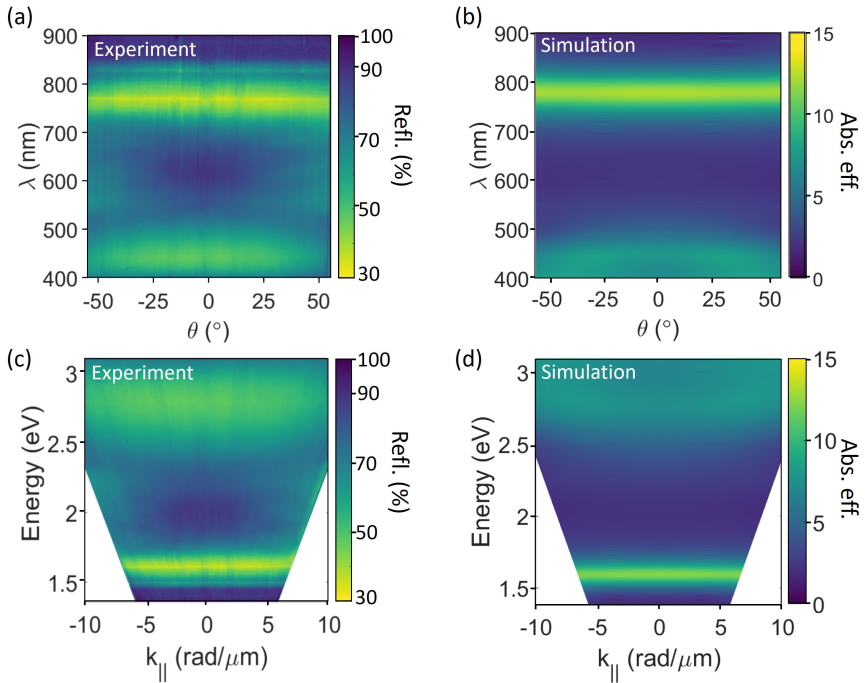

Figure 6.2: (a) and (c) Experimental reflectance dispersions of the randomized array of Ag nanopatch antennas on a HfO_2-Ag substrate (diameter D = 120 nm, height H = 50 nm) for TM-polarized incident light. (a) displays the reflectance as a function of the incident wavelength and angle, while (c) displays this reflectance as a function of the photon energy and $k_{||} = (2\pi/\lambda)\sin(\theta)$. (b) and (d) FDTD simulations of the absorption efficiency of a single Ag nanopatch antenna.

To further confirm the origin of these two modes, we have simulated the absorption efficiencies at normal incidence for nanopatch antennas with different heights on top of a 33 nm thick layer of HfO_2 layer. The results are shown in Fig. 6.4 (a) for H = 50, 70 and 100 nm, where we can see that the S_{11} resonance is nearly independent of the height of the nanodisks. On the other hand, the L_{11} red-shifts as the nanodisk height increases. In addition to these two modes, we also see a resonance at 380 nm which does

not change when the height of the nanodisks is varied. This resonance corresponds to the S_{12} transverse gap mode as confirmed by the simulations of the electric field distributions shown in Figs. Fig. 6.4 (c) and (d) and representing the xz-plane and in the xy-plane at the bottom of the nanodisk, respectively. We observe in Fig. 6.4 (c) a large field amplitude enhancement on the top of the nanodisk, which is associated to the proximity of the L_{11} resonance. Also, a strong field can be noticed in Fig. 6.4 (d) at the bottom of the disk with 3 nodes, which unambiguously assigns this mode to the S_{12} gap SPP.
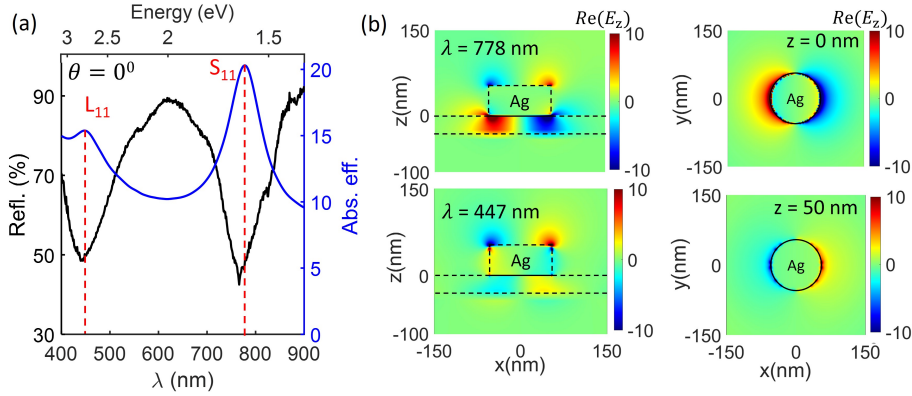

Figure 6.3: (a) Measured reflectance (black) and simulated absorption efficiency spectra (blue) of randomized nanopatch antenna arrays (diameter $D = 120$ nm, height $H = 50$ nm) and single nanopatch antennas, respectively, for $\theta = 0°$. The S_{11} and L_{11} modes are indicated with the vertical-dashed lines. (b) Electric-field distributions $Re(E_z)$ in the xz-plane (left) and xy-plane (right) at 778 nm for the S_{11} mode (top) and at 447 nm for the L_{11} mode (bottom) of a single Ag nanopatch antenna. The boundaries of the Ag nanodisks and the layer of HfO_2 are indicated with the dashed-black lines in the left panels of (b). The black circles on the right panels of (b) represent the boundary of the Ag nanodisk.

Similarly, the absorption efficiencies are calculated for single nanopatch antennas ($H = 50$ nm) with different thickness of HfO_2 layer, as shown in Fig. 6.4 (b). A blue shift of S_{11} mode can be observed when the dielectric layer thickness is increased from 20 nm to 33 nm. The resonance wavelength of the L_{11} mode is hardly affected by this change in the thickness of dielectric layer. All of these features reveal again the nature of gap SPP mode and localized longitudinal resonance in randomized nanodisk-HfO_2-Ag systems [291].

Besides the aforementioned two dips in the randomized arrays, we also notice in Fig. 6.2 (a) a weak feature at around 550 nm for large angles, which is not visible at normal incidence. This feature can be better seen in the spectra shown in Fig. 6.5 (a), measured at $\theta = 50°$ and compared to the simulated absorption efficiency spectra. This feature corresponds to the dark S_{02} gap resonance, which can not be excited at normal incidence due to its symmetric electric field distribution in the disk. At oblique incidence, the field distribution breaks the symmetry and results in a weakly visible S_{02} gap mode in the spectra, as shown in Fig. 6.5 (b). This dark gap SPP mode is better visible in the measurements of the randomized array compared to the simulations done for individual nanodisks, which can be attributed to the interaction of neighboring nanodisks.
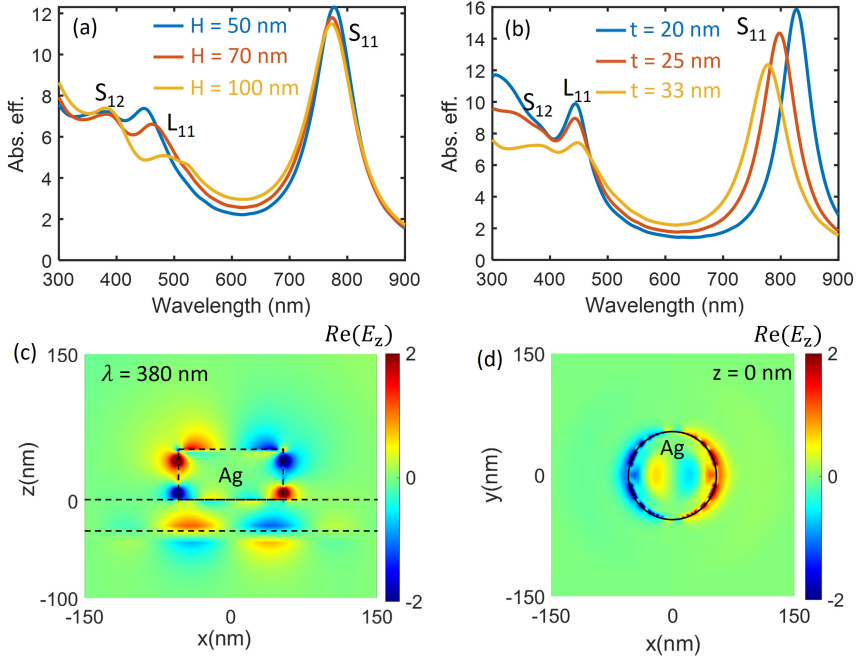
Figure 6.4: (a) Simulated absorption efficiency spectra at normal incidence for single Ag nanopatch antennas with different heights, H = 50, 70 and 100nm, on a 33 nm thick layer of HfO_2 on Ag. (b) Simulated absorption efficiency spectra for nanopatch antennas with different thickness of the HfO_2 layer, t = 20, 25 and 33 nm. The height of the disks is 50 nm. Electric-field distributions $Re(E_z)$ for λ = 380 nm in the (c) xz-plane and (d) xy-plane at the bottom of a disk with H = 50 nm and t = 33 nm. The resonance at this wavelength corresponds to the S_{12} gap mode as can be appreciated by the 3 nodes in field at the bottom of the disk.

The dark S_{02} gap mode in the randomized nanopatch antenna arrays has been further confirmed by simulating single Ag nanopatch antennas with varying height of the nanodisk and varying thickness of the dielectric layer. The simulated absorption efficiency spectra are displayed in Figs. 6.6 (a) and (b), where we observe that this mode is independent of the nanodisk height, but blue shifts as the dielectric layer thickness increases.

6.3.2 Coupled SPP and Dark Gap Mode in Periodic Arrays

After clarifying the origin of the different plasmonic modes in single nanopatch antennas, we further measured the dispersion of a periodic array of nanopatch antennas with diameter D = 120 nm and pitch 330 nm to investigate the effect of the ordering. Figures 6.7 (a) (c) and 6.7 (b) (d) display the reflectance measurements and simulations in the wavelength range 400–900 nm for TM-polarized light illumination. As expected, the gap SPP S_{11} and longitudinal L_{11} resonances are nearly dispersion less, consistent with their localized
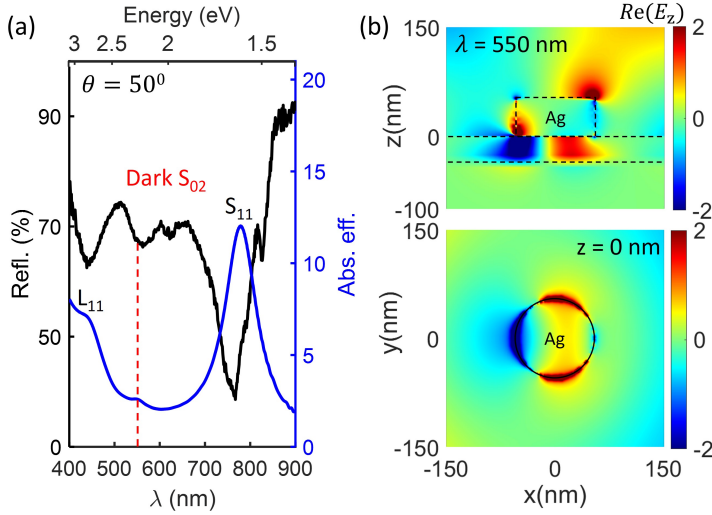
Figure 6.5: (a) Measured reflectance (black) and simulated absorption efficiency spectra (blue) of randomized nanopatch arrays (diameter $D = 120$ nm, height $H = 50$ nm) and single nanopatch antennas, respectively, for $\theta = 50°$. The dark S_{02} gap mode is indicated with the vertical-dashed line. (b) Electric-field distributions $Re(E_z)$ in the xz-plane (top) and xy-plane (bottom) at 550 nm for the S_{02} mode of a single Ag nanopatch antenna. The boundaries of the Ag nanodisk and the layer of HfO$_2$ are indicated with the dashed-black lines in the top panel. The black circle on the bottom panel represent the boundary of the Ag nanodisk.
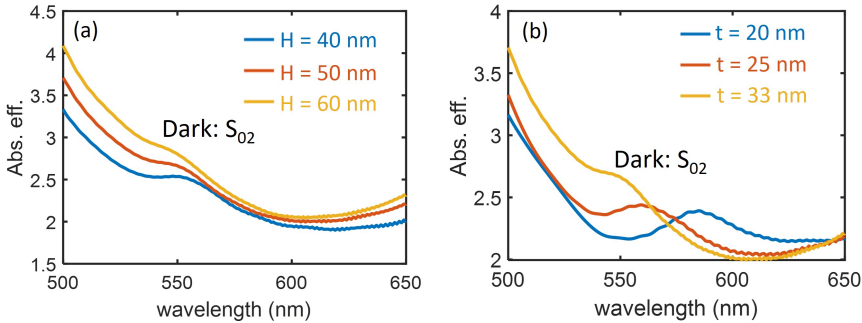
Figure 6.6: (a) Simulated absorption efficiency spectra for single Ag nanopatch antennas with different heights, H = 50, 70 and 100nm, on top of 33 nm thick layer of HfO$_2$ layer on Ag and angle of incidence $\theta = 50°$. (b) Simulated absorption efficiency spectra for single Ag nanopatch antennas with different thickness of the HfO$_2$ layer, t = 20, 25 and 33 nm, and angle of incidence $\theta = 50°$. The height of the Ag disks is 50 nm.

behavior in individual nanopatch antennas as measured in the randomized system.

As shown in the spectra of Fig. 6.8 (a) measured and simulated for normal incidence, besides the gap SPP resonance S_{11} at 778 nm and the longitudinal nanodisk L_{11} mode at

Figure 6.7: (a) (c) Experimental and (b) (d) simulated reflectance dispersion of a periodic array of Ag nanopatch antennas (diameter $D = 120$ nm, height $H = 50$ nm, pitch size $P = 330$ nm) for TM-polarized light illumination. The (1,0) and (-1,0) SPP modes are indicated with the solid-white curves. The dispersion of the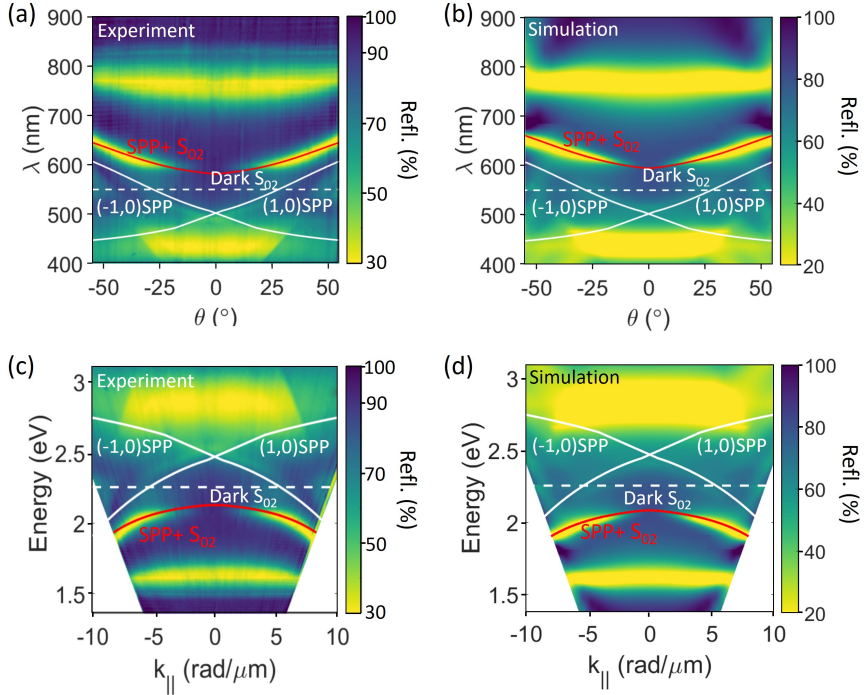 hybrid SPP-S_{02} mode, calculated with a coupled oscillator model is given by the solid-red curve. The wavelength/energy of the dark S_{02} gap mode is given by the dashed-white line.

447 nm, an additional dip in reflection appears at $\lambda \sim 500$ nm. This dip is indicated in the simulations with a dashed-red line. A more detailed description of this SPP mode dispersion will be discussed later in this section. In Fig. 6.8 (b), the spatial distributions of the electric field amplitude ($Re(E_z)$) at 510 nm for normal incidence are displayed in the xz-plane across the middle of the particle and the xy-plane at the bottom of the disk. Besides the field confinement on top of disk due to the L_{11} mode, a large field enhancement can be observed at the interface of the Ag film and HfO$_2$. Therefore, this dip in reflection is associated to the diffractive coupling of the incident light to SPPs in the three layer system (Ag-HfO$_2$-air), which we call lattice SPPs. The dark gap SPP S_{02} resonance at 550 nm is independent of the angle of incidence, indicated in Figs. 6.7 (a)-(d) by the white dashed lines. This resonance can be significantly enhanced by coupling to the lattice SPP, along with the formation of hybrid SPP-gap modes in the periodic arrays.

To characterize the coupling of lattice SPPs and dark gap SPP modes, we fit the dip in the reflectance dispersion to a coupled harmonic oscillator model.[62, 294, 295] The

Hamiltonian that describes this coupling is given by

$$\begin{bmatrix} E_{SPP} - i\gamma_{SPP} & g \\ g & E_{gap} - i\gamma_{gap} \end{bmatrix} \begin{pmatrix} \alpha \\ \beta \end{pmatrix} = E \begin{pmatrix} \alpha \\ \beta \end{pmatrix} \tag{6.1}$$

where E_{SPP} and E_{gap} are the lattice SPP and dark gap resonance energies, respectively, γ_{SPP} and γ_{gap} are the corresponding decoherence rates, and g is the coupling coefficient.

Figure 6.8: (a) Measured (black) and simulated (blue) reflectance spectra for $\theta = 0°$ of a periodic array of Ag nanopatch antennas (diameter $D = 120$ nm, height $H = 50$ nm, pitch size $P = 330$ nm). The $(\pm 1, 0)$ SPP mode in the simulations is indicated by the dashed-red line. (b) Electric-field distributions $Re(E_z)$ in the xz-plane and xy-plane at bottom of disk for 510 nm, corresponding to the $(\pm 1, 0)$ SPP mode.

Since the lattice SPP mode is excited at the air-HfO$_2$-Ag interface, the dispersion relation can be obtained by calculating the eigenstates of a three-layer system, which are given by

$$\exp(-2k_{HfO_2}t) = \frac{k_{HfO_2}/\epsilon_{HfO_2} + k_{air}/\epsilon_{air}}{k_{HfO_2}/\epsilon_{HfO_2} - k_{air}/\epsilon_{air}} \frac{k_{HfO_2}/\epsilon_{HfO_2} + k_{Ag}/\epsilon_{Ag}}{k_{HfO_2}/\epsilon_{HfO_2} - k_{Ag}/\epsilon_{Ag}}, \tag{6.2}$$

and

$$k_i^2 = k_{SPP}^2 - k_0^2\epsilon_i, \tag{6.3}$$

where t is the thickness of HfO$_2$, i corresponds to HfO$_2$, air or Ag, and k_{SPP} is the wave vector of the SPP. The incident plane wave couples to the SPP by diffraction with the periodic array:

$$\mathbf{k_{SPP}} = \mathbf{k}_\parallel + \frac{2\pi}{a}p\mathbf{u_x} + \frac{2\pi}{a}q\mathbf{u_y}, \tag{6.4}$$

where (p, q) define the order of diffraction in the x- and y-directions with unit vectors $\mathbf{u_{x,y}}$, a is the lattice constant of the square array, and $\mathbf{k}_\parallel$ is the wave vector component of the incident wave parallel to the surface, *i.e.*, $k_\parallel = (2\pi/\lambda)\sin(\theta)$. The calculated lattice SPP dispersion relations are plotted with the solid white curves on top of the measured and simulated dispersions in Figs. 6.7 (a)-(d), respectively, for (1,0) and (-1,0) diffraction orders. These dispersions follow the measured and simulated bands of reduced reflection.

The calculated lattice SPP dispersion crosses the dark gap S_{02} resonance indicated with the horizontal dashed white line at 550 nm. This results in the coupling and formation of hybrid SPP-gap modes, which can be appreciated by the redshift of the band of reduced
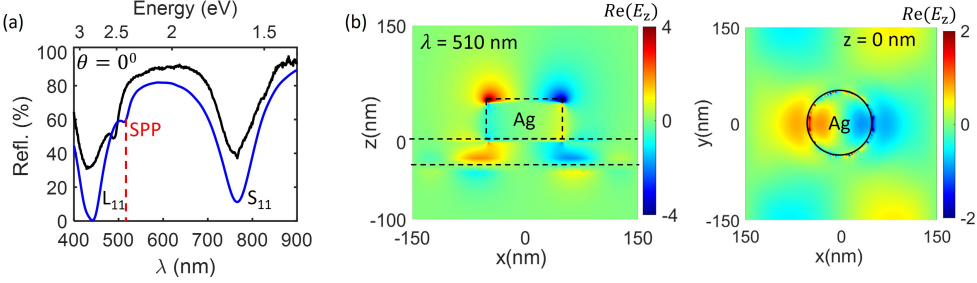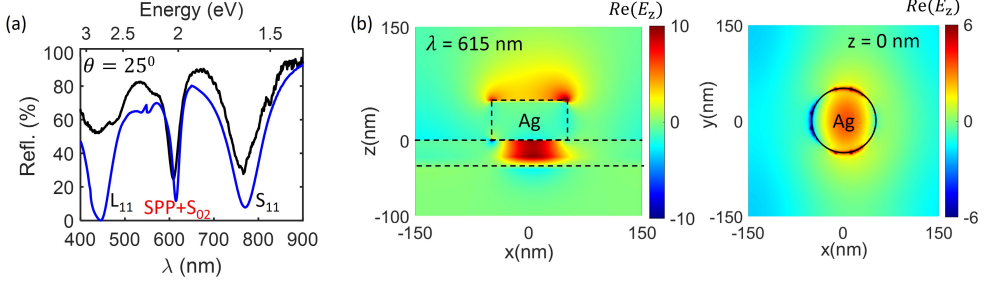
Figure 6.9: (a) (a) Measured (black) and simulated (blue) reflectance spectra for $\theta = 25°$ of a periodic array of Ag nanopatch antennas (diameter $D = 120$ nm, height $H = 50$ nm, pitch size $P = 330$ nm). The hybrid (1,0) lattice SPP and dark S_{02} gap mode is indicated in the figure together with the L_{11} and S_{11}. (b) Electric-field distributions $Re(E_z)$ in the xz-plane and xy-plane at bottom of disk for $\lambda = 615$ nm, corresponding to the hybrid SPP-S_{02} mode.

reflection relative of the SPP dispersion. The dispersion of the hybrid SPP-gap has been fitted in Figs. 6.7 (a)-(d) to the eigenvalues obtained by the diagonalization of the Hamiltonian given in Eq. (6.1). For this fit, we have used the loss rates for the SPP and gap modes $\gamma_{SPP} = 0.1$ eV and $\gamma_{gap} = 0.2$ eV that are estimated from the FWHM of the simulated reflectance spectra. A coupling coefficient $g = 0.2$ eV is used as fitting parameter to the measured band in the range 600-700 nm. A larger coupling coefficient of $g = 0.25$ eV is obtained from the fit to the simulations, which corresponds to a mode splitting of 0.5 eV. Furthermore, the expansion coefficients of the eigenstates on the lattice SPP and S_{02} basis are calculated using the Hamiltonian matrix given by Eq. (6.1). The results, shown in Fig. 6.10, indicate that the SPP fraction of the hybrid mode increases from 40% to 60% when θ is increased to 60°, whereas the S_{02} fraction decreases. The fractions are 50% at $\theta = 28°$ where the anticrossing between the two modes is apparent.

To further analyze the hybrid mode, we have simulated the electric field ($Re(E_z)$) distributions and displayed them in Fig. 6.9 (b) for $\theta = 25°$ and $\lambda = 615$ nm, which corresponds to the narrow dip in the measured and simulated reflectance spectra of Fig. 6.9 (a). The electric field in the xz-plane shows a strong confinement in the dielectric layer as a result of the S_{02} gap mode with a fraction larger than 50 % at $\theta = 25°$. The electric field in the plane of the nanodisk (right panel of Fig. 6.9 (b)) also shows a negative amplitude at other positions than beneath the nanodisk, which illustrates the contribution of the lattice SPP to the hybrid mode.

The strong angular dependence of the hybrid mode can be further analyzed by plotting its reflectance spectra for various angles of incidence, as shown in Figs. 6.11 (a) and (b) for the measurements and FDTD simulations, respectively. At normal incidence, the reflectance dip vanishes. The hybrid lattice SPP-gap mode gradually appears by increasing the angle, showing the redshift as a function of θ. We have calculated the total electric field intensities and reflectance for the hybrid mode in the xz-plane crossing the nanoparticles, as shown in Fig. 6.11 (c). The field intensity increases and the reflectance decreases with increasing angle of incidence. At larger angles that $> 18°$, the total electric field intensity
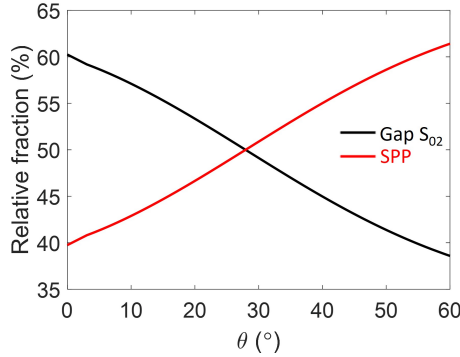
Figure 6.10: Calculated lattice SPP and S_{02} fractions of the hybrid SPP-$S_{0}2$ mode.

decreases, increasing again for angles larger than 28°, where the dark gap S_{02} resonance and the lattice SPP are resonant.

Another distinct feature of the hybrid mode is the Q-factor. We plot this Q-factor, which is extracted from a Lorentzian fit to reflectance measurements, as a function of the angle of incidence in Fig. 6.11 (d). This figure neatly reveals the divergence of the Q-factor with Q > 50 for $\theta < 3°$. The Q-factor strongly depends on the expansion coefficients that are shown in Fig. 6.10. For $\theta < 28°$, the Q-factor decrease is more pronounced because the hybrid mode is dominated by the S_{02} mode with larger intrinsic loss in the Ag nanodisks. While for $\theta > 30°$, the hybrid mode is dominated by the SPP mode. It is worth noting that the behaviour of hybrid mode resembles that of a symmetry protected bound state in the continuum (BIC) due to its dark character at normal incidence (see Figs. 6.7 (a)-(d)) [296–299]. However, Ohmic losses in Ag limits the Q-factor to finite values in contrast to true BICs that have infinite Q-factor by the suppression of the radiation leakage in a lossless medium.

6.3.3 Field Enhancement in Random and Periodic Nanodisk Arrays

While coupling of the dark S_{02} gap mode to the lattice SPP on the Ag-HfO$_2$-air layers leads to a BIC-like dark mode at $\theta = 0°$, the S_{11} gap resonance is expected to lead to a large field enhancement, as shown in Fig. 6.12. For the random array in Figs. 6.2 (a)-(d), and the periodic array in Figs. 6.7 (a)-(d), we plot and compare the spectra for normal incidence in the wavelength range 650-900 nm in Fig. 6.12 (a). The experimental results for both the random (black-dashed curve) and periodic (blue-dashed curve) arrays show very similar spectra. This is consistent with the gap SPP nature of the S_{11} mode, which is barely affected by diffraction. For the measured spectra, the Q-factor is slightly larger in the periodic array (Q = 6.97) compared to that in randomized nanodisks (Q = 6.28). The Q-factors of simulated spectra are also slightly larger compared with experimental results.

To demonstrate the potential of S_{11} resonance in the Ag nanodisk periodic array-insulator-Ag film system to interact with a medium such as a 2D semiconductor, [300–
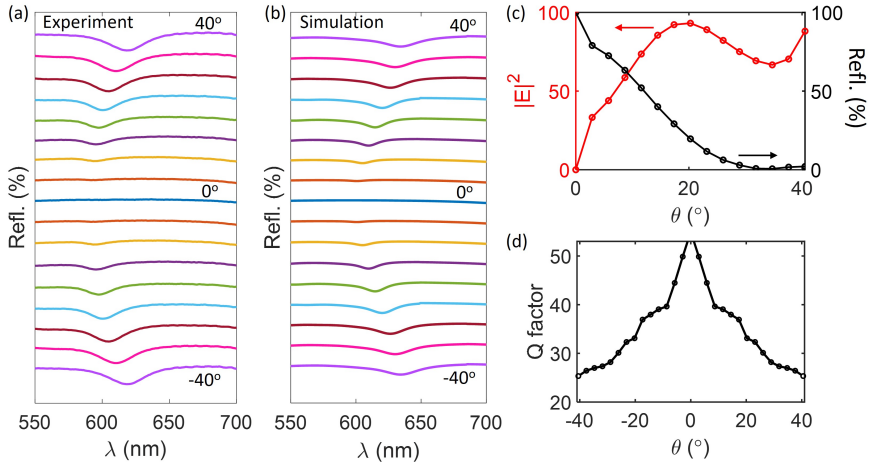
Figure 6.11: Hybrid SPP-S_{02} mode in a periodic Ag nanopatch antenna array. (a) Experimental and (b) FDTD simulations of the reflectance spectra for various angles of incidence in the vicinity of the hybrid band. (c) Total electric field intensity and reflectance of the hybrid band as a function of the angle of incidence θ. (d) Q-factors of the hybrid mode as a function of the angle of incidence.
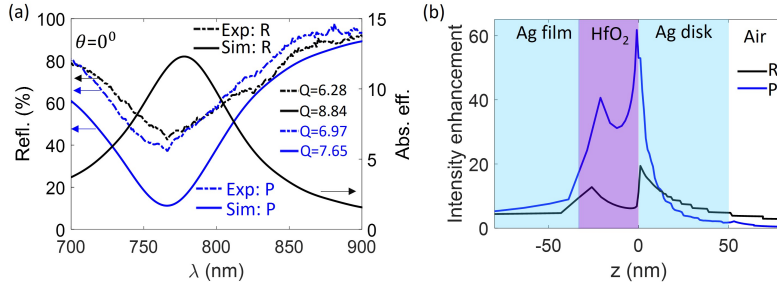
Figure 6.12: The intensity enhancement of localized S_{11} resonance in the cases of the randomized and periodic array. (a) Experimental reflectance spectra for S_{11} mode at a normal incidence that is supported in the randomized (dashed-black) and periodic (dashed-blue) nanopatch antennas. Simulated absorption efficiency spectrum for S_{11} mode in the single nanopatch antenna (solid-black) and simulated reflectance spectrum for S_{11} mode in the periodic nanopatch antennas array (solid-blue) for normal incidence. Inset shows the Q-factors. The Q-factor is calculated by a Lorentzian function that is used to fit the resonance dip and linewidth. (b) Total electric field intensity enhancements of S_{11} mode in randomized (black) and periodic (blue) nanodisks arrays as a function of z position where including the part of Ag film, HfO$_2$ layer and Ag nanodisks.

304] we have calculated the total intensity enhancement (IE) of electrical field for this resonance. The IE is defined as the integral of the field intensity over the volume occupied by the material, normalized to a reference without the nanodisks array. For

a 2D semiconductor at a height z from the Ag film, the IE can be evaluated as a surface integral in the xy-plane as a function of this height and wavelength:

$$\text{IE}(z,\lambda) = \frac{\int_A |E(x,y,z,\lambda)|^2 dxdy}{\int_A |E_{ref}(x,y,z,\lambda)|^2 dxdy}, \quad (6.5)$$

where $E(x,y,z,\lambda)$ is the electric field at wavelength λ and position z and $E_{ref}(x,y,z,\lambda)$ is the electric field of the reference. From the simulations of the IE shown in Fig. 6.12 (b), we observe that the field enhancement is mostly located at the interface of the Ag disk and HfO$_2$ layer. Compared to the IE of S_{11} resonance in random arrays, the IE at the interface of Ag in the periodic array is enhanced by more than 3 times as a result of the field confinement in the plane of the array due to diffraction. Consequently, this gap SPP S_{11} resonance in the periodic metal nanodisks-insulator-metal film system exhibits promising characteristics for applications in which enhanced light-matter interaction is required, such as optical sensors, detectors, and non-linear optics.

6.4 Conclusion

In summary, we have investigated experimentally and theoretically the resonances in random and periodic arrays of metal (Ag) nanopatch antennas, i.e., Ag nanodisks separated by a thin dielectric (HfO$_2$) layer from a metal (Ag) film. While random arrays only show localized longitudinal resonances and transverse gap SPP modes associated to the individual nanodisks, the periodic arrays present hybrid SPP-gap modes that originate from the coupling of lattice SPP resonances in the Ag-HfO$_2$-air film and dark gap S_{02} resonances in the HfO$_2$ layer beneath the nanodisks. The hybrid mode has been investigated by visualization of the electric fields distributions and Q-factor. The Q-factor increases for low angles of incidence, similar to the increase observed in symmetry protected quasi-BICs. Finally, we found that the intensity enhancement of the fundamental S_{11} resonances in the periodic arrays is up to three times larger compared to the random array. This detailed description of field enhancements is important for the design and optimization in applications relying on high local-fields confinements and large Q-factors.

ACRONYMS

FDTD	Finite-differences time domain
SLRs	Surface lattice resonances
PSO	Particle swarm optimization
EM	Electromagnetic
LEDs	Light-emitting diodes
MCM	Multi-coefficient model
LSPRs	Localized surface plasmon resonances
TFSF	Total-field scattered-field
PML	Perfectly matched layer
LSPR	Localized Surface Lattice Resonance
RAs	Rayleigh anomalies
FWHM	Full width at half maximum
SLR	Surface lattice resonance
BIC	Bound states in the continuum
CDA	Coupled dipole approximation
CDM	Coupled dipole method
TE	Transverse Electric
TM	Transverse magnetic
FoM	Figure of merit
P3HT	Poly(3-hexylthiophene-2,5-diyl)
SPP	Surface plasmon polaritons
ED	Electric dipole
MD	Magnetic dipole
IE	Intensity enhancement
FLDOS	Fractional radiative local density of states
QGMs	Quasi-guided modes
ppm	Parts-per-million
ppb	Parts-per-billion
LoD	Limits of detection
PMMA	Poly(methylmethacrylate)
EPs	Exciton-polaritons

Acronyms

OPV	Organic photovoltaic
LPB	Lower polariton band
UPB	Upper polariton band
LP	Lower polariton
UP	Upper polariton
SD	Standard deviation
EBL	Electron-beam lithography
RIE	Reactive-ion etching
NA	Numerical aperture

REFERENCES

[1] *The Fabry Perot Resonator*, pages 189–215, Springer New York, New York, NY, 2005.

[2] A. McGurn, *Nonlinear Optics*, pages 461–490, Springer International Publishing, Cham, 2018.

[3] A. McGurn, *Lasers*, pages 423–444, Springer International Publishing, Cham, 2018.

[4] S. Molesky, Z. Lin, A. Y. Piggott, W. Jin, J. Vucković, and A. W. Rodriguez, *Inverse design in nanophotonics*, Nature Photonics **12**, 659 (2018).

[5] E. J. F. Dickinson, H. Ekström, and E. Fontes, *COMSOL Multiphysics®: Finite element software for electrochemical analysis. A mini-review*, Electrochemistry Communications **40**, 71 (2014).

[6] L. Su, D. Vercruysse, J. Skarda, N. V. Sapra, J. A. Petykiewicz, and J. Vučković, *Nanophotonic inverse design with SPINS: Software architecture and practical considerations*, Applied Physics Reviews **7**, 011407 (2020).

[7] L. I. Ansys.com, *FDTD: 3D Electromagnetic Simulator*, 2020.

[8] *VIII. A dynamical theory of the electromagnetic field*, Philosophical Transactions of the Royal Society of London (1865).

[9] K. Yee, *Numerical solution of initial boundary value problems involving maxwell's equations in isotropic media*, IEEE Transactions on Antennas and Propagation **14**, 302 (1966).

[10] J. B. Cole, R. A. Krutar, S. K. Numrich, and D. B. Creamer, *Finite-difference time-domain simulations of wave propagation and scattering as a research and educational tool*, Computers in Physics **9**, 235 (1995).

[11] W. Sun, N. G. Loeb, and Q. Fu, *Finite-difference time-domain solution of light scattering and absorption by particles in an absorbing medium*, Applied optics **41**, 5728 (2002).

[12] A. Nagra and R. York, *FDTD analysis of wave propagation in nonlinear absorbing and gain media*, IEEE Transactions on Antennas and Propagation **46**, 334 (1998).

[13] J. Young and R. Nelson, *A summary and systematic analysis of FDTD algorithms for linearly dispersive media*, IEEE Antennas and Propagation Magazine **43**, 61 (2001).

[14] F. Zepparelli, F. Alimenti, P. Bassi, P. Mezzanotte, L. Roselli, and R. Sorrentino, *FDTD-analysis of 3D-optical and optoelectronic waveguide-based devices*, in *1999 IEEE MTT-S International Microwave Symposium Digest (Cat. No. 99CH36282)*, volume 3, pages 1257–1260, IEEE, 1999.

[15] J.-W. Kim, J.-H. Jang, M.-C. Oh, J.-W. Shin, D.-H. Cho, J.-H. Moon, and J.-I. Lee, *FDTD analysis of the light extraction efficiency of OLEDs with a random scattering layer*, Opt. Express **22**, 498 (2014).

[16] S. Hagness, A. Taflove, and J. Bridges, *Two-dimensional FDTD analysis of a pulsed microwave confocal system for breast cancer detection: fixed-focus and antenna-array sensors*, IEEE Transactions on Biomedical Engineering **45**, 1470 (1998).

[17] K. G. Ong, O. K. Varghese, G. K. Mor, K. Shankar, and C. A. Grimes, *Application of finite-difference time domain to dye-sensitized solar cells: The effect of nanotube-array negative electrode dimensions on light absorption*, Solar Energy Materials and Solar Cells **91**, 250 (2007).

[18] R. d. L. Kronig, *On the theory of dispersion of x-rays*, Josa **12**, 547 (1926).

[19] B. Y.-K. Hu, *Kramers–Kronig in two lines*, Am. J. Phys **57**, 821 (1989).

[20] K. Waters, M. Hughes, J. Mobley, and J. Miller, *Differential forms of the Kramers-Kronig dispersion relations*, IEEE Transactions on Ultrasonics, Ferroelectrics, and Frequency Control **50**, 68 (2003).

[21] T. J. Kippenberg, R. Holzwarth, and S. A. Diddams, *Microresonator-based optical frequency combs*, science **332**, 555 (2011).

[22] A. Imamoğlu, H. Schmidt, G. Woods, and M. Deutsch, *Strongly interacting photons in a nonlinear cavity*, Physical Review Letters **79**, 1467 (1997).

[23] K. Koshelev, S. Kruk, E. Melik-Gaykazyan, J.-H. Choi, A. Bogdanov, H.-G. Park, and Y. Kivshar, *Subwavelength dielectric resonators for nonlinear nanophotonics*, Science **367**, 288 (2020).

[24] G. Li, S. Zhang, and T. Zentgraf, *Nonlinear photonic metasurfaces*, Nature Reviews Materials **2**, 1 (2017).

[25] F. Vollmer and L. Yang, *Review Label-free detection with high-Q microcavities: a review of biosensing mechanisms for integrated devices*, Nanophotonics **1**, 267 (2012).

[26] B. Sepúlveda, A. Calle, L. M. Lechuga, and G. Armelles, *Highly sensitive detection of biomolecules with the magneto-optic surface-plasmon-resonance sensor*, Optics letters **31**, 1085 (2006).

[27] A. F. Cihan, A. G. Curto, S. Raza, P. G. Kik, and M. L. Brongersma, *Silicon Mie resonators for highly directional light emission from monolayer MoS2*, Nature Photonics **12**, 284 (2018).

[28] J. Wiersig and M. Hentschel, *Unidirectional light emission from high-Q modes in optical microcavities*, Physical Review A **73**, 031802 (2006).

[29] G. Vecchi, V. Giannini, and J. G. Rivas, *Shaping the fluorescent emission by lattice resonances in plasmonic crystals of nanoantennas*, Physical review letters **102**, 146807 (2009).

[30] A. G. Curto, T. H. Taminiau, G. Volpe, M. P. Kreuzer, R. Quidant, and N. F. Van Hulst, *Multipolar radiation of quantum emitters with nanowire optical antennas*, Nature communications **4**, 1 (2013).

[31] A. Manjavacas, F. J. Garcia de Abajo, and P. Nordlander, *Quantum plexcitonics: strongly interacting plasmons and excitons*, Nano letters **11**, 2318 (2011).

[32] J. Foresi, P. R. Villeneuve, J. Ferrera, E. Thoen, G. Steinmeyer, S. Fan, J. Joannopoulos, L. Kimerling, H. I. Smith, and E. Ippen, *Photonic-bandgap microcavities in optical waveguides*, nature **390**, 143 (1997).

[33] D. Rosenblatt, A. Sharon, and A. A. Friesem, *Resonant grating waveguide structures*, IEEE Journal of Quantum electronics **33**, 2038 (1997).

[34] J. Pitarke, V. Silkin, E. Chulkov, and P. Echenique, *Theory of surface plasmons and surface-plasmon polaritons*, Reports on progress in physics **70**, 1 (2006).

[35] S. A. Maier et al., *Plasmonics: fundamentals and applications*, volume 1, Springer, 2007.

[36] K. L. Kelly, E. Coronado, L. L. Zhao, and G. C. Schatz, *The optical properties of metal nanoparticles: The influence of size, shape, and dielectric environment*, Journal of Physical Chemistry B **107**, 668 (2003).

[37] C. Gong and M. S. Leite, *Noble metal alloys for plasmonics*, Acs Photonics **3**, 507 (2016).

[38] M. W. Knight, N. S. King, L. Liu, H. O. Everitt, P. Nordlander, and N. J. Halas, *Aluminum for plasmonics*, ACS nano **8**, 834 (2014).

[39] Q. Zhao, J. Zhou, F. Zhang, and D. Lippens, *Mie resonance-based dielectric metamaterials*, Materials Today **12**, 60 (2009).

[40] W. Wang, M. Ramezani, A. I. Väkeväinen, P. Törmä, J. G. Rivas, and T. W. Odom, *The rich photonic world of plasmonic nanoparticle arrays,* Materials today **21**, 303 (2018).

[41] V. G. Kravets, A. V. Kabashin, W. L. Barnes, and A. N. Grigorenko, *Plasmonic surface lattice resonances: a review of properties and applications,* Chemical reviews **118**, 5912 (2018).

[42] Z. Pan and J. Guo, *Enhanced optical absorption and electric field resonance in diabolo metal bar optical antennas,* Optics Express **21**, 32491 (2013).

[43] E. D. Palik, *Handbook of Optical Constants, Vol.2,* 1991.

[44] G. Lozano, D. J. Louwers, S. R. Rodríguez, S. Murai, O. T. Jansen, M. A. Verschuuren, and J. Gómez Rivas, *Plasmonics for solid-state lighting: enhanced excitation and directional emission of highly efficient light sources,* Light: Science & Applications **2**, e66 (2013).

[45] R. W. Wood, *XLII. On a remarkable case of uneven distribution of light in a diffraction grating spectrum,* The London, Edinburgh, and Dublin Philosophical Magazine and Journal of Science **4**, 396 (1902).

[46] L. Rayleigh, *III. Note on the remarkable case of diffraction spectra described by Prof. Wood,* The London, Edinburgh, and Dublin Philosophical Magazine and Journal of Science **14**, 60 (1907).

[47] H. Raether, *Surface plasmons on smooth surfaces,* in *Surface plasmons on smooth and rough surfaces and on gratings,* pages 4–39, Springer, 1988.

[48] G. Lozano, D. J. Louwers, S. R. Rodríguez, S. Murai, O. T. Jansen, M. A. Verschuuren, and J. Gómez Rivas, *Plasmonics for solid-state lighting: enhanced excitation and directional emission of highly efficient light sources,* Light: Science & Applications **2**, e66 (2013).

[49] F. Wang and Y. R. Shen, *General properties of local plasmons in metal nanostructures,* Physical review letters **97**, 206806 (2006).

[50] I. Zoric, M. Zach, B. Kasemo, and C. Langhammer, *Gold, platinum, and aluminum nanodisk plasmons: material independence, subradiance, and damping mechanisms,* ACS nano **5**, 2535 (2011).

[51] V. Giannini, G. Vecchi, and J. G. Rivas, *Lighting up multipolar surface plasmon polaritons by collective resonances in arrays of nanoantennas,* Physical review letters **105**, 266801 (2010).

[52] K. T. Carron, W. Fluhr, M. Meier, A. Wokaun, and H. Lehmann, *Resonances of two-dimensional particle gratings in surface-enhanced Raman scattering,* JOSA B **3**, 430 (1986).

[53] V. Markel, *Coupled-dipole approach to scattering of light from a one-dimensional periodic dipole structure*, Journal of Modern Optics **40**, 2281 (1993).

[54] S. Zou, N. Janel, and G. C. Schatz, *Silver nanoparticle array structures that produce remarkably narrow plasmon lineshapes*, The Journal of chemical physics **120**, 10871 (2004).

[55] F. G. De Abajo, R. Gómez-Medina, and J. Sáenz, *Full transmission through perfect-conductor subwavelength hole arrays*, Physical review E **72**, 016608 (2005).

[56] T. W. Ebbesen, H. J. Lezec, H. Ghaemi, T. Thio, and P. A. Wolff, *Extraordinary optical transmission through sub-wavelength hole arrays*, nature **391**, 667 (1998).

[57] V. Kravets, F. Schedin, and A. Grigorenko, *Extremely narrow plasmon resonances based on diffraction coupling of localized plasmons in arrays of metallic nanoparticles*, Physical review letters **101**, 087403 (2008).

[58] B. Auguié and W. L. Barnes, *Collective resonances in gold nanoparticle arrays*, Physical review letters **101**, 143902 (2008).

[59] Y. Chu, E. Schonbrun, T. Yang, and K. B. Crozier, *Experimental observation of narrow surface plasmon resonances in gold nanoparticle arrays*, Applied Physics Letters **93**, 181108 (2008).

[60] G. Vecchi, V. Giannini, and J. G. Rivas, *Shaping the fluorescent emission by lattice resonances in plasmonic crystals of nanoantennas*, Physical review letters **102**, 146807 (2009).

[61] G. Vecchi, V. Giannini, and J. G. Rivas, *Surface modes in plasmonic crystals induced by diffractive coupling of nanoantennas*, Physical Review B **80**, 201401 (2009).

[62] S. R. K. Rodriguez, A. Abass, B. Maes, O. T. Janssen, G. Vecchi, and J. G. Rivas, *Coupling bright and dark plasmonic lattice resonances*, Physical Review X **1**, 021019 (2011).

[63] A. García-Etxarri, R. Gómez-Medina, L. S. Froufe-Pérez, C. López, L. Chantada, F. Scheffold, J. Aizpurua, M. Nieto-Vesperinas, and J. J. Sáenz, *Strong magnetic response of submicron silicon particles in the infrared*, Optics express **19**, 4815 (2011).

[64] A. E. Miroshnichenko, W. Liu, D. Neshev, Y. S. Kivshar, A. I. Kuznetsov, Y. H. Fu, and B. Luk'yanchuk, *Magnetic light: optical magnetism of dielectric nanoparticles*, Optics and Photonics News **23**, 35 (2012).

[65] A. B. Evlyukhin, C. Reinhardt, A. Seidel, B. S. Luk'yanchuk, and B. N. Chichkov, *Optical response features of Si-nanoparticle arrays*, Physical Review B **82**, 045404 (2010).

[66] R. Sainidou, J. Renger, T. V. Teperik, M. U. González, R. Quidant, and F. J. Garcia de Abajo, *Extraordinary all-dielectric light enhancement over large volumes*, Nano letters **10**, 4450 (2010).

[67] V. Zakomirnyi, A. Ershov, V. Gerasimov, S. Karpov, H. Ågren, and I. Rasskazov, *Collective lattice resonances in arrays of dielectric nanoparticles: a matter of size*, Optics Letters **44**, 5743 (2019).

[68] A. B. Evlyukhin, C. Reinhardt, A. Seidel, B. S. Luk'yanchuk, and B. N. Chichkov, *Optical response features of Si-nanoparticle arrays*, Physical Review B **82**, 045404 (2010).

[69] P. Ding, M. Li, J. He, J. Wang, C. Fan, and F. Zeng, *Guided mode caused by silicon nanopillar array for light emission enhancement in color-converting LED*, Optics express **23**, 21477 (2015).

[70] A. Vaskin, J. Bohn, K. E. Chong, T. Bucher, M. Zilk, D.-Y. Choi, D. N. Neshev, Y. S. Kivshar, T. Pertsch, and I. Staude, *Directional and spectral shaping of light emission with Mie-resonant silicon nanoantenna arrays*, Acs Photonics **5**, 1359 (2018).

[71] J. Li, N. Verellen, and P. Van Dorpe, *Engineering electric and magnetic dipole coupling in arrays of dielectric nanoparticles*, Journal of Applied Physics **123**, 083101 (2018).

[72] L. Zhao, K. L. Kelly, and G. C. Schatz, *The extinction spectra of silver nanoparticle arrays: influence of array structure on plasmon resonance wavelength and width*, The Journal of Physical Chemistry B **107**, 7343 (2003).

[73] B. T. Draine and P. J. Flatau, *Discrete-dipole approximation for scattering calculations*, Josa a **11**, 1491 (1994).

[74] J. Li, N. Verellen, and P. Van Dorpe, *Engineering electric and magnetic dipole coupling in arrays of dielectric nanoparticles*, Journal of Applied Physics **123**, 083101 (2018).

[75] R. Guo, T. K. Hakala, and P. Törmä, *Geometry dependence of surface lattice resonances in plasmonic nanoparticle arrays*, Physical Review B **95**, 155423 (2017).

[76] P. W. Barber and S. C. Hill, *Light scattering by particles: computational methods*, volume 2, World scientific, 1990.

[77] S. Rodriguez, M. Schaafsma, A. Berrier, and J. G. Rivas, *Collective resonances in plasmonic crystals: Size matters*, Physica B: Condensed Matter **407**, 4081 (2012).

[78] A. Manjavacas, L. Zundel, and S. Sanders, *Analysis of the limits of the near-field produced by nanoparticle arrays*, ACS nano **13**, 10682 (2019).

[79] P. Offermans, M. C. Schaafsma, S. R. Rodriguez, Y. Zhang, M. Crego-Calama, S. H. Brongersma, and J. Gomez Rivas, *Universal scaling of the figure of merit of plasmonic sensors*, ACS nano **5**, 5151 (2011).

[80] J. Kennedy and R. Eberhart, *Particle swarm optimization*, in *Proceedings of ICNN'95-international conference on neural networks*, volume 4, pages 1942–1948, IEEE, 1995.

[81] J. Robinson and Y. Rahmat-Samii, *Particle swarm optimization in electromagnetics*, IEEE transactions on antennas and propagation **52**, 397 (2004).

[82] M. Donelli and A. Massa, *Computational approach based on a particle swarm optimizer for microwave imaging of two-dimensional dielectric scatterers*, IEEE Transactions on Microwave Theory and Techniques **53**, 1761 (2005).

[83] E. Briones, R. Ruiz-Cruz, J. Briones, N. Gonzalez, J. Simon, M. Arreola, and G. Alvarez-Alvarez, *Particle swarm optimization of nanoantenna-based infrared detectors*, Optics express **26**, 28484 (2018).

[84] Z. Cheng, J. Yang, and L. V. Wang, *Intelligently optimized digital optical phase conjugation with particle swarm optimization*, Optics Letters **45**, 431 (2020).

[85] S. He, Q. Liu, T. Sa, and Z. Wang, *Design of broadband reflector at the visible wavelengths using particle swarm optimization*, AIP Advances **9**, 075301 (2019).

[86] A. F. Koenderink, A. Alu, and A. Polman, *Nanophotonics: Shrinking light-based technology*, Science **348**, 516 (2015).

[87] L. Novotny and N. Van Hulst, *Antennas for light*, Nat. Photonics **5**, 83 (2011).

[88] A. Kinkhabwala, Z. Yu, S. Fan, Y. Avlasevich, K. Müllen, and W. Moerner, *Large single-molecule fluorescence enhancements produced by a bowtie nanoantenna*, Nat. Photonics **3**, 654 (2009).

[89] Q. Zhao, J. Zhou, F. Zhang, and D. Lippens, *Mie resonance-based dielectric metamaterials*, Mater. Today **12**, 60 (2009).

[90] A. E. Krasnok, A. E. Miroshnichenko, P. A. Belov, and Y. S. Kivshar, *All-dielectric optical nanoantennas*, Opt. Express **20**, 20599 (2012).

[91] J. Van de Groep and A. Polman, *Designing dielectric resonators on substrates: Combining magnetic and electric resonances*, Opt. Express **21**, 26285 (2013).

[92] R. M. Bakker, D. Permyakov, Y. F. Yu, D. Markovich, R. Paniagua-Domínguez, L. Gonzaga, A. Samusev, Y. Kivshar, B. Luk'yanchuk, and A. I. Kuznetsov, *Magnetic and electric hotspots with silicon nanodimers*, Nano Lett. **15**, 2137 (2015).

[93] A. García-Etxarri, R. Gómez-Medina, L. S. Froufe-Pérez, C. López, L. Chantada, F. Scheffold, J. Aizpurua, M. Nieto-Vesperinas, and J. J. Sáenz, *Strong magnetic response of submicron silicon particles in the infrared*, Opt. Express **19**, 4815 (2011).

[94] A. B. Evlyukhin, S. M. Novikov, U. Zywietz, R. L. Eriksen, C. Reinhardt, S. I. Bozhevolnyi, and B. N. Chichkov, *Demonstration of magnetic dipole resonances of dielectric nanospheres in the visible region*, Nano Lett. **12**, 3749 (2012).

[95] A. I. Kuznetsov, A. E. Miroshnichenko, Y. H. Fu, J. Zhang, and B. Luk'Yanchuk, *Magnetic light*, Scientific Reports **2**, 492 (2012).

[96] I. Staude et al., *Tailoring directional scattering through magnetic and electric resonances in subwavelength silicon nanodisks*, ACS Nano **7**, 7824 (2013).

[97] N. Meinzer, W. L. Barnes, and I. R. Hooper, *Plasmonic meta-atoms and metasurfaces*, Nat. Photonics **8**, 889 (2014).

[98] S. Zou and G. C. Schatz, *Narrow plasmonic/photonic extinction and scattering line shapes for one and two dimensional silver nanoparticle arrays*, The J. Chem. Phys. **121**, 12606 (2004).

[99] F. G. De Abajo, *Colloquium: Light scattering by particle and hole arrays*, Rev. Mod. Phys. **79**, 1267 (2007).

[100] G. Lozano, S. R. Rodriguez, M. A. Verschuuren, and J. G. Rivas, *Metallic nanostructures for efficient LED lighting*, Light: Science & Applications **5**, e16080 (2016).

[101] A. Christ, S. Tikhodeev, N. Gippius, J. Kuhl, and H. Giessen, *Waveguide-plasmon polaritons: strong coupling of photonic and electronic resonances in a metallic photonic crystal slab*, Phys. Rev. Lett. **91**, 183901 (2003).

[102] S. Rodriguez, S. Murai, M. Verschuuren, and J. G. Rivas, *Light-emitting waveguide-plasmon polaritons*, Phys. Rev. Lett. **109**, 166803 (2012).

[103] S. Murai, M. Verschuuren, G. Lozano, G. Pirruccio, S. Rodriguez, and J. G. Rivas, *Hybrid plasmonic-photonic modes in diffractive arrays of nanoparticles coupled to light-emitting optical waveguides*, Opt. Express **21**, 4250 (2013).

[104] V. Kravets, F. Schedin, A. Kabashin, and A. Grigorenko, *Sensitivity of collective plasmon modes of gold nanoresonators to local environment*, Opt. Lett. **35**, 956 (2010).

[105] P. Offermans, M. C. Schaafsma, S. R. Rodriguez, Y. Zhang, M. Crego-Calama, S. H. Brongersma, and J. G. Rivas, *Universal scaling of the figure of merit of plasmonic sensors*, ACS Nano **5**, 5151 (2011).

[106] A. Danilov, G. Tselikov, F. Wu, V. G. Kravets, I. Ozerov, F. Bedu, A. N. Grigorenko, and A. V. Kabashin, *Ultra-narrow surface lattice resonances in plasmonic metamaterial arrays for biosensing applications*, Biosensors and Bioelectronics **104**, 102 (2018).

[107] R. Adato, A. A. Yanik, J. J. Amsden, D. L. Kaplan, F. G. Omenetto, M. K. Hong, S. Erramilli, and H. Altug, *Ultra-sensitive vibrational spectroscopy of protein monolayers with plasmonic nanoantenna arrays*, Proc. Natl. Acad. Sci. U. S. A. **106**, 19227 (2009).

[108] S. Zou and G. C. Schatz, *Silver nanoparticle array structures that produce giant enhancements in electromagnetic fields*, Chem. Phys. Lett. **403**, 62 (2005).

[109] K. Guo, G. Lozano, M. A. Verschuuren, and J. G. Rivas, *Control of the external photoluminescent quantum yield of emitters coupled to nanoantenna phased arrays*, J. Appl. Phys. **118**, 073103 (2015).

[110] S. Wang, Q. Le-Van, T. Peyronel, M. Ramezani, N. Van Hoof, T. G. Tiecke, and J. Gomez Rivas, *Plasmonic nanoantenna arrays as efficient etendue reducers for optical detection*, ACS Photonics **5**, 2478 (2018).

[111] W. Zhou et al., *Lasing action in strongly coupled plasmonic nanocavity arrays*, Nat. Nanotechnol. **8**, 506 (2013).

[112] A. Yang, T. B. Hoang, M. Dridi, C. Deeb, M. H. Mikkelsen, G. C. Schatz, and T. W. Odom, *Real-time tunable lasing from plasmonic nanocavity arrays*, Nat. Commun. **6**, 6939 (2015).

[113] A. H. Schokker and A. F. Koenderink, *Lasing at the band edges of plasmonic lattices*, Phys. Rev. B **90**, 155452 (2014).

[114] M. H. J. W. J. F. C. Z. F. Ding, Pei Li, *Guided mode caused by silicon nanopillar array for light emission enhancement in color-converting LED*, Opt. Express **23**, 21477 (2015).

[115] E. D. Palik, *Handbook of Optical Constants of Solids*, Academic, New York, 1985.

[116] A. I. Kuznetsov, A. E. Miroshnichenko, M. L. Brongersma, Y. S. Kivshar, and B. Luk'yanchuk, *Optically resonant dielectric nanostructures*, Science **354**, aag2472 (2016).

[117] C. F. Bohren and D. R. Huffman, *Absorption and scattering of light by small particles*, John Wiley & Sons, 2008.

[118] Y. Francescato, V. Giannini, and S. A. Maier, *Plasmonic systems unveiled by Fano resonances*, ACS Nano **6**, 1830 (2012).

[119] V. E. Babicheva and J. V. Moloney, *Lattice effect influence on the electric and magnetic dipole resonance overlap in a disk array*, Nanophotonics **7**, 1663 (2018).

[120] G. Lozano, G. Grzela, M. A. Verschuuren, M. Ramezani, and J. G. Rivas, *Tailor-made directional emission in nanoimprinted plasmonic-based light-emitting devices*, Nanoscale **6**, 9223 (2014).

[121] M. Ramezani, G. Lozano, M. A. Verschuuren, and J. G. Rivas, *Modified emission of extended light emitting layers by selective coupling to collective lattice resonances*, Phys. Rev. B **94**, 125406 (2016).

[122] T. H. Taminiau, F. D. Stefani, and N. F. van Hulst, *Enhanced directional excitation and emission of single emitters by a nano-optical Yagi-Uda antenna*, Opt. Express **16**, 10858 (2008).

[123] P. Yeh, *Optical waves in layered media*, volume 61, Wiley-Interscience, 2005.

[124] P. Zijlstra, P. M. Paulo, and M. Orrit, *Optical detection of single non-absorbing molecules using the surface plasmon resonance of a gold nanorod*, Nature nanotechnology **7**, 379 (2012).

[125] F. A. Nugroho et al., *Metal–polymer hybrid nanomaterials for plasmonic ultrafast hydrogen detection*, Nature materials **18**, 489 (2019).

[126] A. Tittl, A. Leitis, M. Liu, F. Yesilkoy, D.-Y. Choi, D. N. Neshev, Y. S. Kivshar, and H. Altug, *Imaging-based molecular barcoding with pixelated dielectric metasurfaces*, Science **360**, 1105 (2018).

[127] T. Xue et al., *Ultrasensitive detection of miRNA with an antimonene-based surface plasmon resonance sensor*, Nature communications **10**, 1 (2019).

[128] B. Wang, P. Yu, W. Wang, X. Zhang, H.-C. Kuo, H. Xu, and Z. M. Wang, *High-Q Plasmonic Resonances: Fundamentals and Applications*, Advanced Optical Materials **9**, 2001520 (2021).

[129] M. S. Luchansky and R. C. Bailey, *High-Q optical sensors for chemical and biological analysis*, Analytical chemistry **84**, 793 (2012).

[130] J. Li et al., *Biosensing using diffractively coupled plasmonic crystals: the figure of merit revisited*, Advanced Optical Materials **3**, 176 (2015).

[131] Y. Yang, I. I. Kravchenko, D. P. Briggs, and J. Valentine, *All-dielectric metasurface analogue of electromagnetically induced transparency*, Nature communications **5**, 1 (2014).

[132] G. W. Castellanos, P. Bai, and J. Gómez Rivas, *Lattice resonances in dielectric metasurfaces*, Journal of Applied Physics **125**, 213105 (2019).

[133] R. Chikkaraddy, B. De Nijs, F. Benz, S. J. Barrow, O. A. Scherman, E. Rosta, A. Demetriadou, P. Fox, O. Hess, and J. J. Baumberg, *Single-molecule strong coupling at room temperature in plasmonic nanocavities*, Nature **535**, 127 (2016).

[134] K. D. Heylman, N. Thakkar, E. H. Horak, S. C. Quillin, C. Cherqui, K. A. Knapper, D. J. Masiello, and R. H. Goldsmith, *Optical microresonators as single-particle absorption spectrometers*, Nature Photonics **10**, 788 (2016).

[135] S. Zou and G. C. Schatz, *Narrow plasmonic/photonic extinction and scattering line shapes for one and two dimensional silver nanoparticle arrays*, The Journal of chemical physics **121**, 12606 (2004).

[136] Z. Li, S. Butun, and K. Aydin, *Ultranarrow band absorbers based on surface lattice resonances in nanostructured metal surfaces*, ACS nano **8**, 8242 (2014).

[137] R. Adato, A. A. Yanik, J. J. Amsden, D. L. Kaplan, F. G. Omenetto, M. K. Hong, S. Erramilli, and H. Altug, *Ultra-sensitive vibrational spectroscopy of protein monolayers with plasmonic nanoantenna arrays*, Proceedings of the National Academy of Sciences **106**, 19227 (2009).

[138] W. Wang, M. Ramezani, A. I. Väkeväinen, P. Törmä, J. G. Rivas, and T. W. Odom, *The rich photonic world of plasmonic nanoparticle arrays*, Materials today **21**, 303 (2018).

[139] B. Špačková and J. Homola, *Sensing properties of lattice resonances of 2D metal nanoparticle arrays: An analytical model*, Optics express **21**, 27490 (2013).

[140] C. Wadell, S. Syrenova, and C. Langhammer, *Plasmonic hydrogen sensing with nanostructured metal hydrides*, ACS nano **8**, 11925 (2014).

[141] F. A. A. Nugroho, I. Darmadi, V. P. Zhdanov, and C. Langhammer, *Universal scaling and design rules of hydrogen-induced optical properties in Pd and Pd-Alloy nanoparticles*, ACS nano **12**, 9903 (2018).

[142] I. Darmadi, F. A. A. Nugroho, and C. Langhammer, *High-performance nanostructured palladium-based hydrogen sensors—current limitations and strategies for their mitigation*, ACS sensors **5**, 3306 (2020).

[143] L. J. Bannenberg, C. Boelsma, K. Asano, H. Schreuders, and B. Dam, *Metal hydride based optical hydrogen sensors*, Journal of the Physical Society of Japan **89**, 051003 (2020).

[144] H. M. Luong, M. T. Pham, T. Guin, R. P. Madhogaria, M.-H. Phan, G. K. Larsen, and T. D. Nguyen, *Sub-second and ppm-level optical sensing of hydrogen using templated control of nano-hydride geometry and composition*, Nature communications **12**, 1 (2021).

[145] V. M. Silkin, R. D. Muiño, I. Chernov, E. V. Chulkov, and P. M. Echenique, *Tuning the plasmon energy of palladium–hydrogen systems by varying the hydrogen concentration*, Journal of Physics: Condensed Matter **24**, 104021 (2012).

[146] C. Langhammer, B. Kasemo, and I. Zorić, *Absorption and scattering of light by Pt, Pd, Ag, and Au nanodisks: absolute cross sections and branching ratios*, The Journal of chemical physics **126**, 194702 (2007).

[147] C. Langhammer, Z. Yuan, I. Zorić, and B. Kasemo, *Plasmonic properties of supported Pt and Pd nanostructures*, Nano letters **6**, 833 (2006).

[148] B. Liu et al., *A plasmonic sensor array with ultrahigh figures of merit and resonance linewidths down to 3 nm*, Advanced Materials **30**, 1706031 (2018).

[149] J. Tian, H. Jiang, X. Zhao, G. Shi, J. Zhang, X. Deng, and W. Zhang, *A Ppb-level hydrogen sensor based on activated Pd nanoparticles loaded on oxidized nickel foam*, Sensors and Actuators B: Chemical **329**, 129194 (2021).

[150] O. Lupan, V. Postica, F. Labat, I. Ciofini, T. Pauporte, and R. Adelung, *Ultra-sensitive and selective hydrogen nanosensor with fast response at room temperature based on a single Pd/ZnO nanowire*, Sensors and Actuators B: Chemical **254**, 1259 (2018).

[151] M. Darabpour and M. M. Doroodmand, *Fabrication of a glow discharge plasma-based ionization gas sensor using multiwalled carbon nanotubes for specific detection of hydrogen at parts per billion levels*, IEEE Sensors Journal **15**, 2391 (2014).

[152] S. Zhou, M. Xiao, F. Liu, J. He, Y. Lin, and Z. Zhang, *Sub-10 parts per billion detection of hydrogen with floating gate transistors built on semiconducting carbon nanotube film*, Carbon **180**, 41 (2021).

[153] J. S. Lee, S. G. Kim, S. Cho, and J. Jang, *Porous palladium coated conducting polymer nanoparticles for ultrasensitive hydrogen sensors*, Nanoscale **7**, 20665 (2015).

[154] X. Li, X. Ma, J. Zhang, E. Akiyama, Y. Wang, and X. Song, *Review of hydrogen embrittlement in metals: Hydrogen diffusion, hydrogen characterization, hydrogen embrittlement mechanism and prevention*, Acta Metallurgica Sinica (English Letters) **33**, 759 (2020).

[155] N. W. Smith, P. R. Shorten, E. H. Altermann, N. C. Roy, and W. C. McNabb, *Hydrogen cross-feeders of the human gastrointestinal tract*, Gut microbes **10**, 270 (2019).

[156] Y. Urita et al., *Extensive atrophic gastritis increases intraduodenal hydrogen gas*, Gastroenterology Research and Practice **2008** (2008).

[157] S. Zou, N. Janel, and G. C. Schatz, *Silver nanoparticle array structures that produce remarkably narrow plasmon lineshapes*, The Journal of chemical physics **120**, 10871 (2004).

[158] B. Auguié and W. L. Barnes, *Collective resonances in gold nanoparticle arrays*, Physical review letters **101**, 143902 (2008).

[159] M. S. Bin-Alam et al., *Ultra-high-Q resonances in plasmonic metasurfaces*, Nature communications **12**, 1 (2021).

[160] H. Gao, J. McMahon, M. Lee, J. Henzie, S. Gray, G. Schatz, and T. Odom, *Rayleigh anomaly-surface plasmon polariton resonances in palladium and gold subwavelength hole arrays*, Optics express **17**, 2334 (2009).

[161] B. D. Thackray, V. G. Kravets, F. Schedin, G. Auton, P. A. Thomas, and A. N. Grigorenko, *Narrow collective plasmon resonances in nanostructure arrays observed at normal light incidence for simplified sensing in asymmetric air and water environments*, Acs Photonics **1**, 1116 (2014).

[162] N. Strohfeldt, A. Tittl, M. Schaferling, F. Neubrech, U. Kreibig, R. Griessen, and H. Giessen, *Yttrium hydride nanoantennas for active plasmonics*, Nano letters **14**, 1140 (2014).

[163] F. Sterl, N. Strohfeldt, R. Walter, R. Griessen, A. Tittl, and H. Giessen, *Magnesium as novel material for active plasmonics in the visible wavelength range*, Nano letters **15**, 7949 (2015).

[164] J. Hong, S. Lee, J. Seo, S. Pyo, J. Kim, and T. Lee, *A highly sensitive hydrogen sensor with gas selectivity using a PMMA membrane-coated Pd nanoparticle/single-layer graphene hybrid*, ACS applied materials & interfaces **7**, 3554 (2015).

[165] C. F. Bohren and D. R. Huffman, *Absorption and scattering of light by small particles*, John Wiley & Sons, 2008.

[166] M. Chen et al., *Response characteristics of hydrogen sensors based on PMMA-membrane-coated palladium nanoparticle films*, ACS Applied Materials & Interfaces **9**, 27193 (2017).

[167] B. Chopard and M. Tomassini, *Particle swarm optimization*, in *Natural Computing Series*, 2018.

[168] K.-J. Jeon, H. R. Moon, A. M. Ruminski, B. Jiang, C. Kisielowski, R. Bardhan, and J. J. Urban, *Air-stable magnesium nanocomposites provide rapid and high-capacity hydrogen storage without using heavy-metal catalysts*, Nature materials **10**, 286 (2011).

[169] C. Wadell, F. A. A. Nugroho, E. Lidstrom, B. Iandolo, J. B. Wagner, and C. Langhammer, *Hysteresis-free nanoplasmonic Pd–Au alloy hydrogen sensors*, Nano letters **15**, 3563 (2015).

[170] L. J. Bannenberg, F. A. A. Nugroho, H. Schreuders, B. Norder, T. T. Trinh, N.-J. Steinke, A. A. Van Well, C. Langhammer, and B. Dam, *Direct comparison of PdAu alloy thin films and nanoparticles upon hydrogen exposure*, ACS applied materials & interfaces **11**, 15489 (2019).

[171] L. Bannenberg, H. Schreuders, and B. Dam, *Tantalum-Palladium: Hysteresis-Free Optical Hydrogen Sensor Over 7 Orders of Magnitude in Pressure with Sub-Second Response*, Advanced Functional Materials **31**, 2010483 (2021).

[172] K. Li, R. Gupta, A. Drayton, I. Barth, D. Conteduca, C. Reardon, K. Dholakia, and T. F. Krauss, *Extended Kalman Filtering Projection Method to Reduce the 3σ Noise Value of Optical Biosensors*, ACS sensors **5**, 3474 (2020).

[173] S. Celiksoy, W. Ye, K. Wandner, K. Kaefer, and C. Sonnichsen, *Intensity-Based Single Particle Plasmon Sensing*, Nano Letters **21**, 2053 (2021).

[174] P. Chen, N. T. Tran, X. Wen, Q. Xiong, and B. Liedberg, *Inflection point of the localized surface plasmon resonance peak: a general method to improve the sensitivity*, ACS sensors **2**, 235 (2017).

[175] B. Foerster, V. A. Spata, E. A. Carter, C. Sönnichsen, and S. Link, *Plasmon damping depends on the chemical nature of the nanoparticle interface*, Science advances **5**, eaav0704 (2019).

[176] S. Khomenko, M. Cirach, E. Pereira-Barboza, N. Mueller, J. Barrera-Gómez, D. Rojas-Rueda, K. de Hoogh, G. Hoek, and M. Nieuwenhuijsen, *Premature mortality due to air pollution in European cities: a health impact assessment*, The Lancet Planetary Health **5**, e121 (2021).

[177] F. A. Nugroho, B. Iandolo, J. B. Wagner, and C. Langhammer, *Bottom-up nanofabrication of supported noble metal alloy nanoparticle arrays for plasmonics*, ACS nano **10**, 2871 (2016).

[178] F. A. A. Nugroho, D. Albinsson, T. J. Antosiewicz, and C. Langhammer, *Plasmonic metasurface for spatially resolved optical sensing in three dimensions*, ACS nano **14**, 2345 (2020).

[179] A. Tittl, C. Kremers, J. Dorfmüller, D. N. Chigrin, and H. Giessen, *Spectral shifts in optical nanoantenna-enhanced hydrogen sensors*, Optical Materials Express **2**, 111 (2012).

[180] I. Darmadi, *Polymer-Nanoparticle Hybrid Materials for Plasmonic Hydrogen Detection*, Chalmers Tekniska Hogskola (Sweden), 2021.

[181] T. W. Ebbesen, *Hybrid Light-Matter States in a Molecular and Material Science Perspective*, Accounts of Chemical Research **49**, 2403 (2016).

[182] D. S. Dovzhenko, S. V. Ryabchuk, Y. P. Rakovich, and I. R. Nabiev, *Light-matter interaction in the strong coupling regime: Configurations, conditions, and applications*, Nanoscale **10**, 3589 (2018).

[183] M. Hertzog, M. Wang, J. Mony, and K. Börjesson, *Strong light-matter interactions: A new direction within chemistry*, Chemical Society Reviews **48**, 937 (2019).

[184] J. Feist and F. J. Garcia-Vidal, *Extraordinary exciton conductance induced by strong coupling*, Physical Review Letters **114**, 1 (2015).

[185] J. Schachenmayer, C. Genes, E. Tignone, and G. Pupillo, *Cavity-enhanced transport of excitons*, Physical Review Letters **114**, 1 (2015).

[186] Y. Zakharko, M. Rother, A. Graf, B. Hähnlein, M. Brohmann, J. Pezoldt, and J. Zaumseil, *Radiative Pumping and Propagation of Plexcitons in Diffractive Plasmonic Crystals*, Nano Letters **18**, 4927 (2018).

[187] G. G. Rozenman, K. Akulov, A. Golombek, and T. Schwartz, *Long-Range Transport of Organic Exciton-Polaritons Revealed by Ultrafast Microscopy*, ACS Photonics **5**, 105 (2018).

[188] R. K. Yadav, M. Otten, W. Wang, C. L. Cortes, D. J. Gosztola, G. P. Wiederrecht, S. K. Gray, T. W. Odom, and J. K. Basu, *Strongly Coupled Exciton-Surface Lattice Resonances Engineer Long-Range Energy Propagation*, Nano Letters **20**, 5043 (2020).

[189] S. Hou, M. Khatoniar, K. Ding, Y. Qu, A. Napolov, V. M. Menon, and S. R. Forrest, *Ultralong-Range Energy Transport in a Disordered Organic Semiconductor at Room Temperature Via Coherent Exciton-Polariton Propagation*, Advanced Materials **32** (2020).

[190] X. Zhong, T. Chervy, S. Wang, J. George, A. Thomas, J. A. Hutchison, E. Devaux, C. Genet, and T. W. Ebbesen, *Non-radiative energy transfer mediated by hybrid light-matter states*, Angewandte Chemie - International Edition **55**, 6202 (2016).

[191] K. Stranius, M. Hertzog, and K. Börjesson, *Selective manipulation of electronically excited states through strong light–matter interactions*, Nature Communications **9**, 1 (2018).

[192] T. V. Shahbazyan, *Exciton-Plasmon Energy Exchange Drives the Transition to a Strong Coupling Regime*, Nano Letters **19**, 3273 (2019).

[193] B. Munkhbat, M. Wersäll, D. G. Baranov, T. J. Antosiewicz, and T. Shegai, *Suppression of photo-oxidation of organic chromophores by strong coupling to plasmonic nanoantennas*, Science Advances **4** (2018).

[194] V. N. Peters, M. O. Faruk, J. Asane, R. Alexander, D. A. Peters, S. Prayakarao, S. Rout, and M. A. Noginov, *Effect of strong coupling on photodegradation of the semiconducting polymer P3HT*, Optica **6**, 318 (2019).

[195] S. Kéna-Cohen and S. R. Forrest, *Room-temperature polariton lasing in an organic single-crystal microcavity*, Nature Photonics **4**, 371 (2010).

[196] M. Ramezani, A. Halpin, A. I. Fernández-Domínguez, J. Feist, S. R.-K. Rodriguez, F. J. Garcia-Vidal, and J. G. Rivas, *Plasmon-exciton-polariton lasing*, Optica **4**, 31 (2017).

[197] D. Sannikov, T. Yagafarov, K. Georgiou, A. Zasedatelev, A. Baranikov, L. Gai, Z. Shen, D. Lidzey, and P. Lagoudakis, *Room Temperature Broadband Polariton Lasing from a Dye-Filled Microcavity*, Advanced Optical Materials **7**, 1900163 (2019).

[198] M. Wei, S. K. Rajendran, H. Ohadi, L. Tropf, M. C. Gather, G. A. Turnbull, and I. D. W. Samuel, *Low-threshold polariton lasing in a highly disordered conjugated polymer*, Optica **6**, 1124 (2019).

[199] J. D. Plumhof, T. Stöferle, L. Mai, U. Scherf, and R. F. Mahrt, *Room-temperature Bose–Einstein condensation of cavity exciton–polaritons in a polymer*, Nature Materials **13**, 247 (2014).

[200] K. S. Daskalakis, S. A. Maier, R. Murray, and S. Kéna-Cohen, *Nonlinear interactions in an organic polariton condensate*, Nature Materials **13**, 271 (2014).

[201] M. De Giorgi, M. Ramezani, F. Todisco, A. Halpin, D. Caputo, A. Fieramosca, J. Gomez-Rivas, and D. Sanvitto, *Interaction and Coherence of a Plasmon-Exciton Polariton Condensate*, ACS Photonics **5**, 3666 (2018).

[202] M. Ramezani, A. Halpin, S. Wang, M. Berghuis, and J. G. Rivas, *Ultrafast Dynamics of Nonequilibrium Organic Exciton-Polariton Condensates*, Nano Letters **19**, 8590 (2019).

[203] J. Keeling and S. Kéna-Cohen, *Bose-einstein condensation of exciton-polaritons in organic microcavities*, Annual Review of Physical Chemistry **71**, 435 (2020).

[204] P. E. Shaw, A. Ruseckas, and I. D. W. Samuel, *Exciton Diffusion Measurements in Poly(3-hexylthiophene)*, Advanced Materials **20**, 3516 (2008).

[205] O. V. Mikhnenko, P. W. M. Blom, and T.-Q. Nguyen, *Exciton diffusion in organic semiconductors*, Energy Environ. Sci. **8**, 1867 (2015).

[206] M. Manceau, S. Chambon, A. Rivaton, J. L. Gardette, S. Guillerez, and N. Lematre, *Effects of long-term UVvisible light irradiation in the absence of oxygen on P3HT and P3HT: PCBM blend*, Solar Energy Materials and Solar Cells **94**, 1572 (2010).

[207] E. Eizner, L. A. Martínez-Martínez, J. Yuen-Zhou, and S. Kéna-Cohen, *Inverting singlet and triplet excited states using strong light-matter coupling*, Science Advances **5** (2019).

[208] A. M. Berghuis, A. Halpin, Q. Le-Van, M. Ramezani, S. Wang, S. Murai, and J. Gómez Rivas, *Enhanced Delayed Fluorescence in Tetracene Crystals by Strong Light-Matter Coupling*, Advanced Functional Materials **29** (2019).

[209] D. Polak, R. Jayaprakash, T. P. Lyons, L. Martínez-Martínez, A. Leventis, K. J. Fallon, H. Coulthard, D. G. Bossanyi, K. Georgiou, A. J. Petty, J. Anthony, H. Bronstein, J. Yuen-Zhou, A. I. Tartakovskii, J. Clark, and A. J. Musser, *Manipulating molecules with strong coupling: Harvesting triplet excitons in organic exciton microcavities*, Chemical Science **11**, 343 (2020).

[210] A. Salomon, C. Genet, and T. W. Ebbesen, *Molecule-light complex: Dynamics of hybrid molecule-surface plasmon states*, Angewandte Chemie - International Edition **48**, 8748 (2009).

[211] T. Virgili, D. Coles, A. M. Adawi, C. Clark, P. Michetti, S. K. Rajendran, D. Brida, D. Polli, G. Cerullo, and D. G. Lidzey, *Ultrafast polariton relaxation dynamics in an organic semiconductor microcavity*, Physical Review B **83**, 245306 (2011).

[212] H. Wang, H. Y. Wang, A. Bozzola, A. Toma, S. Panaro, W. Raja, A. Alabastri, L. Wang, Q. D. Chen, H. L. Xu, F. De Angelis, H. B. Sun, and R. P. Zaccaria, *Dynamics of Strong Coupling between J-Aggregates and Surface Plasmon Polaritons in Subwavelength Hole Arrays*, Advanced Functional Materials **26**, 6198 (2016).

[213] E. Orgiu, J. George, J. A. Hutchison, E. Devaux, J. F. Dayen, B. Doudin, F. Stellacci, C. Genet, J. Schachenmayer, C. Genes, G. Pupillo, P. Samorì, and T. W. Ebbesen, *Conductivity in organic semiconductors hybridized with the vacuum field*, Nature Materials **14**, 1123 (2015).

[214] G. Lerario, D. Ballarini, A. Fieramosca, A. Cannavale, A. Genco, F. Mangione, S. Gambino, L. Dominici, M. De Giorgi, G. Gigli, and D. Sanvitto, *High-speed flow of interacting organic polaritons*, Light: Science and Applications **6**, 16212 (2017).

[215] D. Hagenmüller, J. Schachenmayer, S. Schütz, C. Genes, and G. Pupillo, *Cavity-Enhanced Transport of Charge*, Physical Review Letters **119**, 1 (2017).

[216] E. Eizner, J. Brodeur, F. Barachati, A. Sridharan, and S. Kéna-Cohen, *Organic Photo-diodes with an Extended Responsivity Using Ultrastrong Light-Matter Coupling*, ACS Photonics **5**, 2921 (2018).

[217] V. C. Nikolis, A. Mischok, B. Siegmund, J. Kublitski, X. Jia, J. Benduhn, U. Hörmann, D. Neher, M. C. Gather, D. Spoltore, and K. Vandewal, *Strong light-matter coupling for reduced photon energy losses in organic photovoltaics*, Nature Communications **10**, 1 (2019).

[218] M. Wang, M. Hertzog, and K. Börjesson, *Polariton-assisted excitation energy channeling in organic heterojunctions*, Nature communications **12**, 1 (2021).

[219] P. A. Hobson, W. L. Barnes, D. G. Lidzey, G. A. Gehring, D. M. Whittaker, M. S. Skolnick, and S. Walker, *Strong exciton-photon coupling in a low-Q all-metal mirror microcavity*, Applied Physics Letters **81**, 3519 (2002).

[220] C. Cherqui, M. R. Bourgeois, D. Wang, and G. C. Schatz, *Plasmonic Surface Lattice Resonances: Theory and Computation*, Accounts of Chemical Research **52**, 2548 (2019).

[221] S. Zou and G. C. Schatz, *Silver nanoparticle array structures that produce giant enhancements in electromagnetic fields*, Chemical Physics Letters **403**, 62 (2005).

[222] V. G. Kravets, F. Schedin, and A. N. Grigorenko, *Extremely narrow plasmon resonances based on diffraction coupling of localized plasmons in arrays of metallic nanoparticles*, Physical Review Letters **101**, 1 (2008).

[223] Q. Le-Van, E. Zoethout, E. J. Geluk, M. Ramezani, M. Berghuis, and J. Gómez Rivas, *Enhanced Quality Factors of Surface Lattice Resonances in Plasmonic Arrays of Nanoparticles*, Advanced Optical Materials **7** (2019).

[224] M. Ramezani, A. Halpin, J. Feist, N. Van Hoof, A. I. Fernández-Domínguez, F. J. Garcia-Vidal, and J. Gómez Rivas, *Dispersion Anisotropy of Plasmon-Exciton-Polaritons in Lattices of Metallic Nanoparticles*, ACS Photonics **5**, 233 (2018).

[225] J. Robinson and Y. Rahmat-Samii, *Particle swarm optimization in electromagnetics*, IEEE Transactions on Antennas and Propagation **52**, 397 (2004).

[226] Z. Cheng, J. Yang, and L. V. Wang, *Intelligently optimized digital optical phase conjugation with particle swarm optimization*, Optics Letters **45**, 431 (2020).

[227] E. Briones, R. Ruiz-Cruz, J. Briones, N. Gonzalez, J. Simon, M. Arreola, and G. Alvarez-Alvarez, *Particle swarm optimization of nanoantenna-based infrared detectors,* Optics Express **26**, 28484 (2018).

[228] S. He, Q. Liu, T. Sa, and Z. Wang, *Design of broadband reflector at the visible wavelengths using particle swarm optimization,* AIP Advances **9** (2019).

[229] A. P. Piotrowski, J. J. Napiorkowski, and A. E. Piotrowska, *Population size in Particle Swarm Optimization,* Swarm and Evolutionary Computation **58**, 100718 (2020).

[230] M. Ramezani, M. Berghuis, and J. Gómez Rivas, *Strong light–matter coupling and exciton-polariton condensation in lattices of plasmonic nanoparticles [Invited],* Journal of the Optical Society of America B **36**, E88 (2019).

[231] T. Schwartz, J. A. Hutchison, C. Genet, and T. W. Ebbesen, *Reversible switching of ultrastrong light-molecule coupling,* Physical Review Letters **106**, 1 (2011).

[232] R. Wagner, L. Heerklotz, N. Kortenbruck, and F. Cichos, *Back focal plane imaging spectroscopy of photonic crystals,* Applied Physics Letters **101**, 081904 (2012).

[233] A. M. Berghuis, V. Serpenti, M. Ramezani, S. Wang, and J. Gómez Rivas, *Light–Matter Coupling Strength Controlled by the Orientation of Organic Crystals in Plasmonic Cavities,* The Journal of Physical Chemistry C **124**, 12030 (2020).

[234] S. R. K. Rodriguez, A. Abass, B. Maes, O. T. A. Janssen, G. Vecchi, and J. Gómez Rivas, *Coupling Bright and Dark Plasmonic Lattice Resonances,* Phys. Rev. X **1**, 021019 (2011).

[235] V. Savona, L. C. Andreani, P. Schwendimann, and A. Quattropani, *Quantum well excitons in semiconductor microcavities: Unified treatment of weak and strong coupling regimes,* Solid State Communications **93**, 733 (1995).

[236] R. Houdré, *Early stages of continuous wave experiments on cavity-polaritons,* Physica Status Solidi (B) Basic Research **242**, 2167 (2005).

[237] T. J. Antosiewicz, S. P. Apell, and T. Shegai, *Plasmon-Exciton Interactions in a Core-Shell Geometry: From Enhanced Absorption to Strong Coupling,* ACS Photonics **1**, 454 (2014).

[238] M. C. Scharber and N. S. Sariciftci, *Efficiency of bulk-heterojunction organic solar cells,* Progress in polymer science **38**, 1929 (2013).

[239] H. Hoppe and N. S. Sariciftci, *Organic solar cells: An overview,* Journal of materials research **19**, 1924 (2004).

[240] A. Uddin, *Organic solar cells,* in *Comprehensive Guide on Organic and Inorganic Solar Cells,* pages 25–55, Elsevier, 2022.

[241] H. Lee, C. Park, D. H. Sin, J. H. Park, and K. Cho, *Recent advances in morphology optimization for organic photovoltaics*, Advanced Materials **30**, 1800453 (2018).

[242] A. J. Moulé, J. B. Bonekamp, and K. Meerholz, *The effect of active layer thickness and composition on the performance of bulk-heterojunction solar cells*, Journal of Applied Physics **100**, 94503 (2006).

[243] F. Cheng, G. Fang, X. Fan, N. Liu, N. Sun, P. Qin, Q. Zheng, J. Wan, and X. Zhao, *Enhancing the short-circuit current and efficiency of organic solar cells using MoO3 and CuPc as buffer layers*, Solar Energy Materials and Solar Cells **95**, 2914 (2011).

[244] F. Li, L. Kou, W. Chen, C. Wu, and T. Guo, *Enhancing the short-circuit current and power conversion efficiency of polymer solar cells with graphene quantum dots derived from double-walled carbon nanotubes*, NPG Asia Materials **5**, e60 (2013).

[245] H.-Y. Chen, J. Hou, S. Zhang, Y. Liang, G. Yang, Y. Yang, L. Yu, Y. Wu, and G. Li, *Polymer solar cells with enhanced open-circuit voltage and efficiency*, Nature photonics **3**, 649 (2009).

[246] D. Di Nuzzo, G.-J. A. Wetzelaer, R. K. Bouwer, V. S. Gevaerts, S. C. Meskers, J. C. Hummelen, P. W. Blom, and R. A. Janssen, *Simultaneous Open-Circuit Voltage Enhancement and Short-Circuit Current Loss in Polymer: Fullerene Solar Cells Correlated by Reduced Quantum Efficiency for Photoinduced Electron Transfer*, Advanced Energy Materials **3**, 85 (2013).

[247] N. K. Elumalai and A. Uddin, *Open circuit voltage of organic solar cells: an in-depth review*, Energy & Environmental Science **9**, 391 (2016).

[248] J. Yuan et al., *Single-junction organic solar cell with over 15% efficiency using fused-ring acceptor with electron-deficient core*, Joule **3**, 1140 (2019).

[249] A. Raman, Z. Yu, and S. Fan, *Dielectric nanostructures for broadband light trapping in organic solar cells*, Optics express **19**, 19015 (2011).

[250] H.-P. Wang, D.-H. Lien, M.-L. Tsai, C.-A. Lin, H.-C. Chang, K.-Y. Lai, and J.-H. He, *Photon management in nanostructured solar cells*, Journal of Materials Chemistry C **2**, 3144 (2014).

[251] B. Lipovšek, A. Čampa, F. Guo, C. J. Brabec, K. Forberich, J. Krč, and M. Topič, *Detailed optical modelling and light-management of thin-film organic solar cells with consideration of small-area effects*, Optics Express **25**, A176 (2017).

[252] J.-L. Wu, F.-C. Chen, Y.-S. Hsiao, F.-C. Chien, P. Chen, C.-H. Kuo, M. H. Huang, and C.-S. Hsu, *Surface plasmonic effects of metallic nanoparticles on the performance of polymer bulk heterojunction solar cells*, ACS nano **5**, 959 (2011).

[253] L. Qiao, D. Wang, L. Zuo, Y. Ye, J. Qian, H. Chen, and S. He, *Localized surface plasmon resonance enhanced organic solar cell with gold nanospheres*, Applied Energy **88**, 848 (2011).

[254] N. C. Lindquist, W. A. Luhman, S.-H. Oh, and R. J. Holmes, *Plasmonic nanocavity arrays for enhanced efficiency in organic photovoltaic cells*, Applied Physics Letters **93**, 350 (2008).

[255] C. Stelling, C. R. Singh, M. Karg, T. A. König, M. Thelakkat, and M. Retsch, *Plasmonic nanomeshes: their ambivalent role as transparent electrodes in organic solar cells*, Scientific reports **7**, 1 (2017).

[256] J. R. Tumbleston, D.-H. Ko, E. T. Samulski, and R. Lopez, *Absorption and quasiguided mode analysis of organic solar cells with photonic crystal photoactive layers*, Optics Express **17**, 7670 (2009).

[257] D. H. Wang, K. H. Park, J. H. Seo, J. Seifter, J. H. Jeon, J. K. Kim, J. H. Park, O. O. Park, and A. J. Heeger, *Enhanced power conversion efficiency in PCDTBT/PC70BM bulk heterojunction photovoltaic devices with embedded silver nanoparticle clusters*, Advanced Energy Materials **1**, 766 (2011).

[258] X. Li, W. C. H. Choy, H. Lu, W. E. Sha, and A. H. P. Ho, *Efficiency enhancement of organic solar cells by using shape-dependent broadband plasmonic absorption in metallic nanoparticles*, Advanced Functional Materials **23**, 2728 (2013).

[259] L. Lu, Z. Luo, T. Xu, and L. Yu, *Cooperative plasmonic effect of Ag and Au nanoparticles on enhancing performance of polymer solar cells*, Nano letters **13**, 59 (2013).

[260] J. Zhu, M. Xue, H. Shen, Z. Wu, S. Kim, J.-J. Ho, A. Hassani-Afshar, B. Zeng, and K. L. Wang, *Plasmonic effects for light concentration in organic photovoltaic thin films induced by hexagonal periodic metallic nanospheres*, Applied Physics Letters **98**, 151110 (2011).

[261] J. van de Groep, D. Gupta, M. A. Verschuuren, M. M Wienk, R. A. Janssen, and A. Polman, *Large-area soft-imprinted nanowire networks as light trapping transparent conductors*, Scientific Reports **5**, 1 (2015).

[262] C. Forestiere, M. Donelli, G. F. Walsh, E. Zeni, G. Miano, and L. Dal Negro, *Particle-swarm optimization of broadband nanoplasmonic arrays*, Optics letters **35**, 133 (2010).

[263] M. Notarianni, K. Vernon, A. Chou, M. Aljada, J. Liu, and N. Motta, *Plasmonic effect of gold nanoparticles in organic solar cells*, Solar Energy **106**, 23 (2014).

[264] C. C. Wang, W. C. Choy, C. Duan, D. D. Fung, E. Wei, F.-X. Xie, F. Huang, and Y. Cao, *Optical and electrical effects of gold nanoparticles in the active layer of polymer solar cells*, Journal of Materials Chemistry **22**, 1206 (2012).

[265] B. Wu, X. Wu, C. Guan, K. Fai Tai, E. K. L. Yeow, H. Jin Fan, N. Mathews, and T. C. Sum, *Uncovering loss mechanisms in silver nanoparticle-blended plasmonic organic solar cells*, Nature communications **4**, 1 (2013).

[266] N. Kalfagiannis, P. Karagiannidis, C. Pitsalidis, N. Panagiotopoulos, C. Gravalidis, S. Kassavetis, P. Patsalas, and S. Logothetidis, *Plasmonic silver nanoparticles for improved organic solar cells*, Solar Energy Materials and Solar Cells **104**, 165 (2012).

[267] M. Xue, L. Li, B. J. Tremolet de Villers, H. Shen, J. Zhu, Z. Yu, A. Z. Stieg, Q. Pei, B. J. Schwartz, and K. L. Wang, *Charge-carrier dynamics in hybrid plasmonic organic solar cells with Ag nanoparticles*, Applied Physics Letters **98**, 119 (2011).

[268] V. Kochergin, L. Neely, C.-Y. Jao, and H. D. Robinson, *Aluminum plasmonic nanostructures for improved absorption in organic photovoltaic devices*, Applied Physics Letters **98**, 73 (2011).

[269] M. Sygletou, G. Kakavelakis, B. Paci, A. Generosi, E. Kymakis, and E. Stratakis, *Enhanced stability of aluminum nanoparticle-doped organic solar cells*, ACS Applied Materials & Interfaces **7**, 17756 (2015).

[270] P. Bai, S. Ter Huurne, E. van Heijst, S. Murai, and J. Gómez Rivas, *Evolutionary optimization of light-matter coupling in open plasmonic cavities*, The Journal of Chemical Physics **154**, 134110 (2021).

[271] T. W. Ebbesen, H. J. Lezec, H. Ghaemi, T. Thio, and P. A. Wolff, *Extraordinary optical transmission through sub-wavelength hole arrays*, nature **391**, 667 (1998).

[272] J. Pitarke, V. Silkin, E. Chulkov, and P. Echenique, *Theory of surface plasmons and surface-plasmon polaritons*, Reports on progress in physics **70**, 1 (2006).

[273] Y. Chu and K. B. Crozier, *Experimental study of the interaction between localized and propagating surface plasmons*, Optics letters **34**, 244 (2009).

[274] Q. Li, J. Gao, H. Yang, H. Liu, X. Wang, Z. Li, and X. Guo, *Tunable plasmonic absorber based on propagating and localized surface plasmons using metal-dielectric-metal structure*, Plasmonics **12**, 1037 (2017).

[275] R. R. Gutha, S. M. Sadeghi, C. Sharp, and W. J. Wing, *Biological sensing using hybridization phase of plasmonic resonances with photonic lattice modes in arrays of gold nanoantennas*, Nanotechnology **28**, 355504 (2017).

[276] S. V. Zhukovsky, V. E. Babicheva, A. V. Uskov, I. E. Protsenko, and A. V. Lavrinenko, *Enhanced electron photoemission by collective lattice resonances in plasmonic nanoparticle-array photodetectors and solar cells*, Plasmonics **9**, 283 (2014).

[277] K. Ueno and H. Misawa, *Surface plasmon-enhanced photochemical reactions*, Journal of Photochemistry and Photobiology C: Photochemistry Reviews **15**, 31 (2013).

[278] S. Palomba, M. Danckwerts, and L. Novotny, *Nonlinear plasmonics with gold nanoparticle antennas*, Journal of Optics A: Pure and Applied Optics **11**, 114030 (2009).

[279] A. I. Fernández-Domínguez, F. J. García-Vidal, and L. Martín-Moreno, *Unrelenting plasmons*, Nature Photonics **11**, 8 (2017).

[280] A. Christ, Y. Ekinci, H. Solak, N. Gippius, S. Tikhodeev, and O. Martin, *Controlling the Fano interference in a plasmonic lattice*, Physical Review B **76**, 201405 (2007).

[281] K. Aydin, V. E. Ferry, R. M. Briggs, and H. A. Atwater, *Broadband polarization-independent resonant light absorption using ultrathin plasmonic super absorbers*, Nature communications **2**, 1 (2011).

[282] J. Cesario, M. U. Gonzalez, S. Cheylan, W. L. Barnes, S. Enoch, and R. Quidant, *Coupling localized and extended plasmons to improve the light extraction through metal films*, Optics express **15**, 10533 (2007).

[283] S. Linden, J. Kuhl, and H. Giessen, *Controlling the interaction between light and gold nanoparticles: selective suppression of extinction*, Physical review letters **86**, 4688 (2001).

[284] A. Christ, T. Zentgraf, S. Tikhodeev, N. Gippius, J. Kuhl, and H. Giessen, *Controlling the interaction between localized and delocalized surface plasmon modes: Experiment and numerical calculations*, Physical Review B **74**, 155435 (2006).

[285] J. Cesario, R. Quidant, G. Badenes, and S. Enoch, *Electromagnetic coupling between a metal nanoparticle grating and a metallic surface*, Optics letters **30**, 3404 (2005).

[286] B. Yildiz, M. Habib, A. Rashed, and H. Caglayan, *Hybridized plasmon modes in a system of metal thin film–nanodisk array*, Journal of Applied Physics **126**, 113104 (2019).

[287] Q. Le-Van, E. Zoethout, E.-J. Geluk, M. Ramezani, M. Berghuis, and J. Gómez Rivas, *Enhanced quality factors of surface lattice resonances in plasmonic arrays of nanoparticles*, Advanced Optical Materials **7**, 1801451 (2019).

[288] C. Tserkezis, R. Esteban, D. O. Sigle, J. Mertens, L. O. Herrmann, J. J. Baumberg, and J. Aizpurua, *Hybridization of plasmonic antenna and cavity modes: Extreme optics of nanoparticle-on-mirror nanogaps*, Physical Review A **92**, 053811 (2015).

[289] R. Chikkaraddy et al., *How ultranarrow gap symmetries control plasmonic nanocavity modes: from cubes to spheres in the nanoparticle-on-mirror*, Acs Photonics **4**, 469 (2017).

[290] J.-H. Huh, J. Lee, and S. Lee, *Comparative study of plasmonic resonances between the roundest and randomly faceted Au nanoparticles-on-mirror cavities*, ACS Photonics **5**, 413 (2018).

[291] C. Zhang, J.-P. Hugonin, J.-J. Greffet, and C. Sauvan, *Surface plasmon polaritons emission with nanopatch antennas: enhancement by means of mode hybridization*, ACS photonics **6**, 2788 (2019).

[292] R. Esteban, G. Aguirregabiria, A. G. Borisov, Y. M. Wang, P. Nordlander, G. W. Bryant, and J. Aizpurua, *The morphology of narrow gaps modifies the plasmonic response*, ACS photonics **2**, 295 (2015).

[293] Y. Yang, O. D. Miller, T. Christensen, J. D. Joannopoulos, and M. Soljacic, *Low-loss plasmonic dielectric nanoresonators*, Nano letters **17**, 3238 (2017).

[294] C. Garrido Alzar, M. Martinez, and P. Nussenzveig, *Classical analog of electromagnetically induced transparency*, American Journal of Physics **70**, 37 (2002).

[295] S. Mukherjee, H. Sobhani, J. B. Lassiter, R. Bardhan, P. Nordlander, and N. J. Halas, *Fanoshells: nanoparticles with built-in Fano resonances*, Nano letters **10**, 2694 (2010).

[296] Y. Liang, K. Koshelev, F. Zhang, H. Lin, S. Lin, J. Wu, B. Jia, and Y. Kivshar, *Bound states in the continuum in anisotropic plasmonic metasurfaces*, Nano Letters **20**, 6351 (2020).

[297] M. Gong, P. Hu, Q. Song, H. Xiang, and D. Han, *Bound states in the continuum from a symmetric mode with a dominant toroidal dipole resonance*, Physical Review A **105**, 033504 (2022).

[298] S. Sun et al., *Tunable plasmonic bound states in the continuum in the visible range*, Physical Review B **103**, 045416 (2021).

[299] Q. T. Trinh, S. K. Nguyen, D. H. Nguyen, G. K. Tran, V. H. Le, H.-S. Nguyen, and Q. Le-Van, *Coexistence of surface lattice resonances and bound states in the continuum in a plasmonic lattice*, Optics Letters **47**, 1510 (2022).

[300] W. Liu, Y. Wang, B. Zheng, M. Hwang, Z. Ji, G. Liu, Z. Li, V. J. Sorger, A. Pan, and R. Agarwal, *Observation and active control of a collective polariton mode and polaritonic band gap in few-layer WS2 strongly coupled with plasmonic lattices*, Nano Letters **20**, 790 (2019).

[301] G. M. Akselrod, C. Argyropoulos, T. B. Hoang, C. Ciracì, C. Fang, J. Huang, D. R. Smith, and M. H. Mikkelsen, *Probing the mechanisms of large Purcell enhancement in plasmonic nanoantennas*, Nature Photonics **8**, 835 (2014).

[302] Y. C. Jun, R. Pala, and M. L. Brongersma, *Strong modification of quantum dot spontaneous emission via gap plasmon coupling in metal nanoslits*, The Journal of Physical Chemistry C **114**, 7269 (2010).

[303] C. Yuan, Y. Wang, H. Cheng, H. Wang, M. Kuo, M. Shih, and J. Tang, *Modification of fluorescence properties in single colloidal quantum dots by coupling to plasmonic gap modes*, The Journal of Physical Chemistry C **117**, 12762 (2013).

[304] T. B. Hoang, G. M. Akselrod, C. Argyropoulos, J. Huang, D. R. Smith, and M. H. Mikkelsen, *Ultrafast spontaneous emission source using plasmonic nanoantennas*, Nature communications **6**, 1 (2015).

Summary and Future Perspective

Summary

Nanophotonics is the field of photonics that investigates the behavior of light at the nanometer scale and the interaction of light with nanostructures. Examples of these structures are metallic nanoparticles and nanoantennas with their plasmonics properties, photonic crystals with their special photonic dispersion given by the photonic bands, and semiconductor quantum dots with their quantum confinement effect. The advent of nanophotonics has created a new playground for exploring high-Q resonances and light–matter interactions for applications in optical and optoelectronic devices, such as sensors, solar cells, LEDs and semiconductor-based photonic devices. For functional applications, it is important to manipulate light at the nanoscale, i.e. beyond the diffraction limit, so that it is possible to tune the spectral range of resonant frequencies. An advantage of nanostructures is that their optical properties can be easily changed by tuning the geometrical parameters. Usually, this tuneability is achieved by synthesizing nanostructures with different shapes, sizes, materials, by controlling their arrangement in lattices and/or their near- and far-field coupling. Different types of nanostructures and nanostructure's arrangements should be designed for different applications. In this thesis, we have introduced an evolutionary optimization, i.e., Particle Swarm Optimization (PSO), to improve the nanophotonic design for optical and optoelectronic applications.

PSO combined with Finite Differences in Time Domain (FDTD) simulations enable the optimization of continuous functions describing the optical properties of nanophotonic structures. By doing so, the best design of these structures can be extracted from ranges of different parameters. In our research, we have designed several nanostructures consisting of nanoparticles and nanoparticle arrays. These arrays can support surface lattice resonances (SLRs) that present remarkably narrow line widths, low radiation losses, and high field enhancements over large volumes. These properties highlight the potential application of SLRs for the enhanced performance of optical and optoelectronical devices.

The thesis starts in chapter 1 with a brief introduction to localized resonances in single nano-disk structures, SLRs in periodic nanoparticle arrays, and the evolutionary optimization method. Following the introduction, chapter 2 describes two kinds of collective resonances in lattices of dielectric nanoparticles: Electric and magnetic SLRs in silicon nanoparticle arrays when they are homogeneously embedded in a dielectric material, and quasi-guided modes when silicon nanoparticle arrays are on top of an optical waveguide. Furthermore, we describe the remarkable differences in the intensity enhancement and field distributions for these two types of resonances. Both of them exhibit narrow line widths and high electromagnetic field enhancements, providing valuable information for the design and optimization in applications.

In the following three chapters, the PSO algorithm combined with FDTD simulations is used to optimize the geometrical parameters of nanostructures for different applications. Chapter 3 investigates the sensitivity of optical hydrogen sensors based on SLRs in palladium nanoparticle arrays. We tune the height and diameter of the nanoparticles, the period of the array, and the thickness of the PMMA layer on top. The optimized sensor displays a non-trivial balance between a large optical response upon hydrogenation and narrow spectral features. Furthermore, it is experimentally demonstrated that the measured *ppb* limit of detection is an order of magnitude lower than in any previous optical hydrogen sensor.

In chapter 4, we investigate and optimize the coupling strength between excitons in P3HT and SLRs in arrays of aluminum nanoparticles. The height and diameter of the nanoparticles and the lattice constant of square arrays are optimized. Strong light-matter coupling and the formation of exciton-polaritons are demonstrated. We have also fabricated the optimal nanostructures and retrieved a maximum Rabi splitting. This result illustrates an efficient approach to optimize resonant structures for light-matter coupling in polaritonic devices.

Chapter 5 focuses on the short-circuit current (J_{sc}) enhancement in organic solar cells with nanostructured electrodes: nanoparticle arrays and nanohole arrays. PSO is performed with FDTD simulations to optimize the height and diameter of the nanoparticles and nanoholes, the period of the array, and the thickness of acceptor-donor blend layers. Our results show that nanoparticle arrays are able to significantly enhance the J_{sc}, while this J_{sc} is always decreased with nanohole arrays. Our findings and optimization method will guide scientists in the design of organic solar cells with the best possible performance.

In chapter 6, we present a comparison between random and periodic arrays of Ag nanodisks on thin dielectric layer on top of Ag mirrors. Periodic arrays lead to the effective coupling of incident light to surface plasmon polaritons, with a dark character in the normal direction to the sample surface.

Future perspective

In the following, we discuss the possible future directions in which this research could develop. We focus on two directions: the functional nanophotonic inverse design and optimization methods, and the effects of strong light-matter coupling in polaritonic devices.

Inverse design and optimization of nanophotonics

The widely used evolutionary optimization algorithms belongs to the category of inverse design. Applications have been the driving force for the progress of these methods. More specifically and motivated by a given figure of merit (FoM) that defines the ultimate performance of an optical device, which are the feature size range and selection of materials for an optimum design? In principle, inverse-design methods can explore the full space of possible devices providing an answer to this question. This capability opens the possibility of reasonably asking what is the maximum theoretical performance of optical devices and it will help to guide future work in all fields of nanophotonics, including nonlinear, topological, near-field, and integrated photonics.

A challenge for inverse design and optimization of functional nanophotonic devices is constructing a model involving the FoM as simply and accurately as possible. Several key improvements would enable the widespread use of inverse-design methods in practical applications. Efforts should be focused on the development of new solvers for improvements in fast iterative methods for solving Maxwell equations. In the enduring quest for optimal photonic designs, the widespread integration of inverse-design and optimization tools seems not only sensible but unavoidable.

Strong light-matter coupling in optoelectric devices

Exciton-polaritons are hybrid quasi-particles made up of photons strongly coupled to excitons in semiconductors. Research on strong light-matter coupling has been mainly focused on the modification of the properties of the semiconductor, such as the exciton-polariton energy, the enhancement of charge transport and exciton-polariton diffusion, the suppression of photo-degradation and the improvement photoluminescence. In early experiments, strong light-matter coupling with organic materials was done with Fabry-Perot microcavities, which are cavities enclosed by two mirrors. These cavities greatly reduce the in- and out-coupling of light and limit the application in optoelectronic devices, where we need to maximize light harvesting. Alternatively, open cavities based on distributed feedback coupling have received great attention, like the periodic arrays of nanoparticles introduced in this thesis. These cavities can be implemented in optoelectronic devices without the degradation of the device's functionality.

As investigated in chapter 3 of this thesis, the optical absorption by a donor material has been significantly enhanced in the strong-coupling regime. Other meaningful effects in this regime that researchers are striving to explore include the red-shifting of the optical gap of organic solar cell due to the lower energy of polariton states, hereby reducing

the energy losses for strongly absorbed photons. To achieve this improvement in the performance of organic solar cell, it is key to enhance the coupling strength. Another potential development is the increased energy transfer rate due to the hybrid character of polaritons. The short diffusion length of excitons in organic materials limits the thickness of the active layers in organic solar cells to around 100 nm, which reduces the light absorption efficiency and the carrier collection probability by the electrodes. A promising method to solve this problem is to introduce polariton-assisted energy channeling in organic solar cells. Exciton-polaritons are quasiparticles that have demonstrate a rich variety of quantum phenomena, which may open a very valuable future direction for the improvement of opto-electronic devices.

LIST OF PUBLICATIONS

This thesis is based on the following publications:

1. *Lattice resonances in dielectric metasurfaces*, G. W. Castellanos, P. Bai and J. Gómez Rivas, **Journal of Applied Physics** 125(21), 213105 (2019). **(Chapter 2)**

   This publication was a starting project for P.B.'s PhD to become familiar with simulation tools and FDTD methods under G.W.C.'s guidance. P.B. developed and performed rudimentary simulations and associated data analysis. G.W.C. performed more accurate simulations and data analysis and wrote the manuscript. J.G.R. supervised P.B. and G.W.C.

2. *Inverse Designed Plasmonic Metasurface with ppb Optical Hydrogen Detection*, F. A. A. Nugroho*, P. Bai*, I. Darmadi*, G. W. Castellanos, J. Fritschze, C. Langhammer, J. Gómez Rivas and A. Baldi, **Submitted to Nature Communications** (2021). **(Chapter 3)**

   This publication was done in collaboration with F.A.A.N. and A.B. for the Vrij Universiteit Amsterdam. F.A.A.N., P.B. and I.D. contributed equally. F.A.A.N. and A.B. conceived the project. F.A.A.N. and P.B. executed the FDTD calculation. P.B. developed and performed the PSO algorithm. I.D. and J.F. fabricated the sensors. F.A.A.N. and I.D. designed the sensing measurements. I.D. performed the sensing measurements. F.A.A.N. and G.W.C. measured the transmission and angle dispersion of the arrays. C.L. supervised I.D. and J.F., J.G.R. supervised P.B. and G.W.C., A.B. supervised F.A.A.N. and the project as a whole. F.A.A.N. performed data analysis and wrote the first draft of the manuscript. All authors commented and edited the manuscript.

3. *Evolutionary optimization of light-matter coupling in open plasmonic cavities*, P. Bai, S. ter Huurne, E. van Heijst, S. Murai and J. Gómez Rivas, **The Journal of Chemical Physics** 154, 134110 (2021). **(Chapter 4)**

   P.B. is the main author of this publication under J.G.R. supervision. P.B. developed and performed the evolutionary optimization, data analysis and all simulations. S.M. from Kyoto University fabricated the sample. S.T.H. and E.V.H. measured the angle dispersion of the sample. P.B. wrote the manuscript with all authors' comments.

4. *Evolutionary Optimization of the Short-Circuit Current Enhancement in Organic Solar Cells by Nanostructured Electrodes*, P. Bai, M. S. Abdelkhalik, Diogo G.A. Castanheira and J. Gómez Rivas, **Submitted to Journal of Applied Physics** (2022). **(Chapter 5)**

   P.B. is the main author of this publication under J.G.R. supervision. P.B. developed and performed the evolutionary optimization, data analysis and all simulations. M.S.A. and D.G.A.C. joined the edit of introduction and references. P.B. wrote the manuscript with all authors' comments.

5. *Coupled Surface Plasmon Polaritons and Dark Gap Plasmons in Periodic Arrays of Nanopatch Antennas*, M. P. Liang*, P. Bai*, A. M. Berghuis, O. Zheliuk, P. Wan, X. Peng, J. Gómez Rivas and J. T. Ye, **In preparation** (2022). **(Chapter 6)**

   This project was done in collaboration with M.P.L. and J.T.Y. from the university of Groningen. M.P.L. fabricated the samples. A.M.B. measured the angle dispersion reflection of samples. P.B. performed all the simulations and mode analysis. M.P.L. and P.B. wrote the manuscript with all authors' comments.

* Equal contribution

Other publications by the author:

1. *Controlling Exciton Propagation in Organic Crystals through Strong Coupling to Plasmonic Nanoparticle Arrays*, A. M. Berghuis, R. Tichauer, L. de Jong, I. Sokolovskii, P. Bai, M. Ramezani, S. Murai, G. Groenhof and J. Gómez Rivas, **ACS Photonics** (2022).

2. *High-Q Collective Mie Resonances in Monocrystalline Silicon Nanoantenna Arrays for the Visible Light*, Z. Zhang, P. Liu, W. Lu, P. Bai, B. Zhang, Z. Chen, S. A. Maiere, J. Gómez Rivas, S. Wang and X. Li, **Fundamental Research** (2021).

3. *Manipulating the directional emission of monolayer semiconductors by dielectric nanoantenna arrays*, P. Liu, Z. Zhang, M. Lang, W. Lu, P. Bai, Z. Chen, S. Wang and X. Li, **Journal of Optics** 24, 024005 (2022).

4. *Non-Hermitian photonics for coherent perfect absorption, invisibility, and lasing with different orbital angular momenta*, P. Bai, J. Luo, H. Chu, W. Lu, L. Lai, **Opt. Lett.** 46, 4336-4336 (2021).

5. *Collective Mie Exciton-Polaritons in an Atomically Thin Semiconductor*, S. Wang, T.V. Raziman, S. Murai, G. W. Castellanos, P. Bai, A. M. Berghuis, R. H. Godiksen, A. G. Curto and J. Gómez Rivas, **J. Phys. Chem. C** 124, 1919619203 (2020).

6. *Simultaneous realization of a coherent perfect absorber and laser by zero-index media with both gain and loss*, P. Bai, K. Ding, G. Wang, J. Luo, Z. Q. Zhang, C. T. Chan, Y. Wu, Y. Lai, **Phys. Rev. A** 94, 063841 (2016).

7. *Sound-impenetrable holes in water based on acoustic complementary medium*, C. K. Liu*, P. Bai*, Y. Lai, **EPL** 115, 58002 (2016).

8. *Multi-channel coherent perfect absorbers*, P. Bai, Y. Wu, Y. Lai, **EPL** 114, 28003 (2016).

9. *Acoustic coherent perfect absorbers*, J. Z. Song, P. Bai, Z. H. Hang and Y. Lai, **New J. Phys.** 16, 033026 (2014).

* Equal contribution

CONFERENCE CONTRIBUTIONS

Talks:

1. *Evolutionary Optimization of Nanophotonic Design for Optical and Optoelectronic Applications*, **Oral Presentation**, The 12th International conference on Metamaterials, Photonic Crystals and Plasmonics, Torremolinos, Spain (July 2022).

2. *Evolutionary Optimization of Nanophotonic Design for Optical and Optoelectronic Applications*, **(Virtual) Oral Presentation**, NWO Physics@Veldhoven 2022, Veldhove, Netherland (Jounary 2022).

3. *Transition between propagation, perfect absorption and lasing states in energy-balanced materials with both gain and loss*, **Oral Presentation**, The 6th International conference on Metamaterials, Photonic Crystals and Plasmonics, New York, U.S.A (August 2015).

Posters:

1. *Evolutionary Optimization of Strong Light-Matter Coupling*, Strong Coupling with Organic Molecules (SCOM), (April 2021).

2. *Evolutionary Optimization of Strong Light-Matter Coupling*, NWO Physics@Veldhoven, Veldhove, (January 2021).

3. *Towards Polaritonic Optoelectronics: Strong Coupling of Excitons in Polymers with Photons*, NWO Physics@Veldhoven, Veldhove, (January 2020).

4. *Collective resonances and strong light-matter coupling for organic photovoltaics*, ICMS outreach symposium, (March 2019).

ACKNOWLEDGEMENTS

contributions in chapter 4. Mohammad, I admire how you deal with so many people at work. It has been a pleasure to work with you in the same office. Niels, although you left the group a while ago, I still remember you friendly showing me the THz setup when I first visit the laboratory. Francesco, you are always lively and made me feel relax when talking with you. Maira, you are so nice. I will always remember that you gave me a sweet chocolate when I was in a bad mood. I also want to extend my gratitude to the other members of this group: Aleks, Lian, Tomas, Simrjit, Minpeng, Pim and Thomas. Moreover, I would like to thank Alberto Curto and his group members Raziman, Rasmus, Sara, Ershad, Marzieh for their helpful inputs and comments in the group meetings, as well as the other PSN group members for your contributions on Monday's Lunch meetings.

During my PhD, I had the great opportunity of collaborating with the group of Dr. Andrea Baldi at DIFFER and the Vrij Universiteit Amsterdam and the group of prof. Jinanting Ye at the University of Groningen. I want to thank Ferry and Iwan for the nice fabrication and measurements. I am very grateful for your great contributions to the results in chapter 2. Also thanks to Minpeng for your samples and measurements in chapter 6. Moreover, I would like to thanks Tom from the Molecular Materials and Nanosystems (M2N) group for the advice on organic solar cell design during our meetings.

I really enjoyed being part of the PSN group thanks to the secretary Simone Manche-Krooswijk. Thank you for the kindly assistance in the daily administration and the organization of the nice group activities.

I would also like to thank for the financial support provided by the China Scholarship Council (CSC) from the Chinese government and NWO for partially financing this PhD thesis with the Vici grant SCOPE.

I also want to express my gratitude to my family for the unconditioned trust and support. Dad and Mom, thank you for your understanding and support for me over the years. Your tolerance and love are self-evident. I would like to thank my sisters and brother for taking care of our parents so well.

我还要感谢我的家人对我的无条件信任和支持。爸爸妈妈，谢谢你们多年来对我的理解和支持。你们的包容和爱是不言而喻的。我也要感谢我的姐姐和弟弟，是你们把我们的父母照顾得这么好，让我安心追求自己的学业。

The last spot on this list is dedicated to an extra special person. Zhijian, my boyfriend, your company is my greatest motivation in life. You always give me helpful advice when I was in doubt, and sticking with me in some troubling times. Thanks so much for your love and emotional support.

Thank you.
Ping

About the Author

Ping Bai was born on 28 February 1989 in Ganzhou, China.

She completed her bachelor's degree in information and computational sciences at the *Qi Lu University of Technology* (Jinan, China) in 2012. In 2012-2013, she worked as a junior high school physics teacher.

In 2013, she started her master's studies in optical physics, with a specific focus on coherent perfect absorbers, lasing based on metamaterials at *Soochow University*, China, supervised by Prof. Yun Lai. During her master's studies, she visited *King Abdullah University of Science and Technology (KAUST)* in Thuwal, Saudi Arabia twice and worked on the research projects of simultaneous realization of a coherent perfect absorber and laser by zero-index media with both gain and loss, and coherent perfect absorption in elasticity at Prof. Ying Wu's group. She completed her master's degree in physics in 2016 with the project "The Theory and Design of Novel Optical and Acoustical Absorption Systems".

In 2017, she started her PhD at *Eindhoven university of Technology* with a scholarship from the China Scholarship Council, a Chinese governmental organization. Since October 2018, she is part of the Photonics and Semiconductor Nanophysics (PSN) group as a PhD student under the supervision of Prof. Jaime Gomez Rivas working also for the NWO Vici project SCOPE. The main focus of the project is on the simulation and optimization of the strong light-matter coupling in nanoparticle arrays for optical and optoelectronic applications. The results of these studies, combined with other works in collaboration with Dr. Andrea Baldi's group of the Vrij Universiteit Amsterdam and Dr. Jianting Ye's group of the University of Groningen performed during the project, are presented in this thesis.

In her spare time, she likes cooking Chinese food, trekking in the mountain area and bike touring.